2003

Analysis and Structural Health Monitoring of Composite Plates with Piezoelectric Sensors and Actuators

Richard C. Mewer

Follow this and additional works at: http://digitalcommons.library.umaine.edu/etd

 Part of the Mechanical Engineering Commons

ANALYSIS AND STRUCTURAL HEALTH MONITORING OF

COMPOSITE PLATES WITH PIEZOELECTRIC

SENSORS AND ACTUATORS

By

Richard C. Mewer

B.S. The University of Maine, 2001

A THESIS

Submitted in Partial Fulfillment of the

Requirements for the Degree of

Master of Science

(in Mechanical Engineering)

The Graduate School

The University of Maine

May, 2003

Advisory Committee:

   Senthil Vel, Assistant Professor of Mechanical Engineering, Advisor

   Donald A. Grant, R. C. Hill Professor and Chair of Mechanical Engineering

   James Sucec, Professor of Mechanical Engineering

   Vincent Caccese, Associate Professor of Mechanical Engineering

ANALYSIS AND STRUCTURAL HEALTH MONITORING OF

COMPOSITE PLATES WITH PIEZOELECTRIC

SENSORS AND ACTUATORS

By Richard C. Mewer

Thesis Advisor: Dr. Senthil S. Vel

Structural vibration suppression and health-monitoring have been the focus of intense research over the past decade, and piezoelectric actuators and sensors are particularly well suited to serve in this application. The first part is an analytical investigation into the cylindrical bending vibrations of piezoelectric composite plates. The second part is a fully experimental investigation into various vibration based structural health-monitoring techniques for bolted composites.

The analytical solution consists of Fourier basis functions that satisfy the equations of motion and charge equation. The accuracy of the mechanical displacements, electric potential, and stresses are dependent on the number of terms in the series solution. The solution is validated by comparing the natural frequencies with published results for a simply supported piezoelectric plate. Studies were conducted to establish the convergence of the analytical solution. The analytical natural frequencies, electric

potential, displacements and stresses compared well with the finite element method for cantilever piezoelectric composite plates.

The bolted joint is one of the most common mechanical components in engineering structures. A common mode of failure for bolted joints is self-loosening. The objective of the second part of the thesis is to investigate different vibration based structural health monitoring schemes to actively interrogate a square composite plate to detect loose bolts in composite structures. The plate was excited using a piezoelectric actuator and piezoelectric shear accelerometers and dynamic strain sensors were used to characterize the system dynamics. The investigation began with the sensitivity of the fundamental frequency to changes in the bolt clamping force around the perimeter of the plate. Attempts were also made to quantify damage from changes in the transfer functions. The method of transmittance functions was employed extensively, and it was successful in detecting damage but proved to be unreliable in determining the damage location.

TABLE OF CONTENTS

LIST OF TABLES

LIST OF FIGURES

1. INTRODUCTION

This chapter provides an overview of the thesis. The thesis commences with the background information, followed by the motivations for the study and an outline of the thesis. The thesis consists of two distinct investigations, both related to smart structures. In the first part, an analytical solution for the vibration of laminated piezoelectric composite plates consisting of elastic and piezoelectric layers is developed. In the second part of the thesis different vibration based structural health monitoring schemes using a piezoelectric actuator and sensors for bolted composite structures are investigated.

1.1 Background

Smart Structures are systems in which actuators, sensors and controls have been integrated with structures for functionality. A special class of smart structures, obtained by integrating piezoelectric materials with structural systems, has found widespread use in engineering applications for self vibration suppression and health monitoring. Piezoelectricity is a phenomenon observed in certain crystals, e.g., quartz, PZT (Lead Zirconate Titanate) ceramic materials and PVDF (polyvinylidene fluoride) polymer. In the direct piezoelectric effect, a piezoelectric material generates an electric field when subjected to a mechanical strain. In the converse piezoelectric effect, the piezoelectric material exhibits mechanical deformation when subjected to an electric field. This coupling between electrical and mechanical energy makes piezoelectric materials very useful as transducers in many applications, e.g., accelerometers, ultrasonic transmitters and piezoelectric stack actuators. By bonding piezoelectric actuators to structures, desired localized strains can be induced by applying appropriate voltages to the actuators.

Piezoelectric materials bonded to structures can also be used as dynamic strain sensors. It should be noted that piezoelectric sensors measure only dynamic strains since piezoelectric materials are capacitive in nature and cannot measure continuous static stresses. While static stress will cause an initial output, this signal will slowly decay based on the piezoelectric material and time constant of the attached electronics.

More than a decade of intensive research in the area of smart materials and structures has demonstrated the viability and potential of this technology. Numerous applications have been proposed and conceived experimentally for piezoelectric smart structures, such as for active vibration suppression, noise cancellation, shape control and structural health monitoring.

1.2 Motivations

In order to effectively integrate piezoelectric materials with structural systems, a good understanding of the mechanical interaction between the actuators and the host structure is needed. Laminated composite structures consisting of piezoelectric and fiber-reinforced layers are commonly analyzed using plate theories. However, these methods are based on several kinematical assumptions for the displacements and electric potential. In order to validate these plate models, it is necessary to obtain three-dimensional analytical solutions that do not rely on simplifying assumptions. Most of the three-dimensional analytical solutions presented in the literature are applicable only when the edges are simply supported and subjected to specific types of electric boundary conditions. Since simply supported boundary conditions are rarely encountered in practice, it would be useful to develop analytical solutions for the vibration of

piezoelectric composite plates that are subjected to arbitrary boundary conditions at the edges. This is the objective of the first part of the thesis.

The bolted joint is one of the most common mechanical components in engineering structures. The United States Navy has particular interest in detecting degradation of bolted composite connections due to bolt loosening because of their current research in developing composite hull forms through the MACH project (Caccese, 2001). Often bolted joints are critical to the function of the structure and their failure could have huge costs or endanger lives. The failure modes of bolted joints can be very complex. The most frequent mode of failure for bolted joints is self-loosening. The objective of the second part of the thesis is to investigate different vibration based structural health monitoring schemes to detect loose bolts in composite structures.

1.3 Thesis Outline

As mentioned earlier, this thesis consists of two distinct parts covered by two distinctly different chapters. Chapter 2 presents the analytical solution for cylindrical bending vibration of piezoelectric composite plates, and is a purely analytical investigation. In contrast, Chapter 3 is a fully experimental investigation into various vibration based structural health-monitoring techniques for bolted composites.

A literature review of analytical solutions and a new analytical solution for the vibration of piezoelectric composite plates are presented in Chapter 2. The mathematical formulation of the problem is presented next along with the analytical solution. The natural frequencies and mode shapes of three different cases are found using the new solution technique. Confirmation of the technique is made through comparisons with published results (Heyliger and Brooks, 1996), and Finite Element models.

3

A literature review of previous work in the field of structural health monitoring using vibration techniques, and an experimental investigation of selected methods are given in Chapter 3. These include the transfer function method and the transmittance functions technique where the mathematical theories and experimental methods employed are presented in detail. And the thesis is wrapped up with a discussion of the results and performances of the investigated structural-health monitoring techniques.

2. ANALYTICAL SOLUTION FOR THE CYLINDRICAL BENDING VIBRATION OF PIEZOELECTRIC COMPOSITE PLATES

Smart structures, consisting of piezoelectric materials integrated with structural systems, have found widespread use in engineering applications for self vibration suppression and health monitoring. Piezoelectric materials are capable of altering the structure's response through sensing, actuation and control. They exhibit two basic electromechanical phenomena that have led to their use as sensors and actuators in the control of structural systems. In sensor applications, an applied mechanical strain induces an electric potential in the material due to the direct piezoelectric effect, whereas in actuator applications, an applied electric field causes the material to deform.

Presented in this chapter is the formulation and analytical solution for the cylindrical bending vibrations of linear piezoelectric laminated plates obtained by extending the Stroh formalism to the generalized plane strain vibrations of piezoelectric materials. The laminated plate consists of homogeneous elastic or piezoelectric laminae of arbitrary thickness. Fourier basis functions for the mechanical displacements and electric potential that identically satisfy the equations of motion and the charge equation of electrostatics are used to solve boundary value problems via the superposition principle. The coefficients in the infinite series solution are determined from the boundary conditions at the edges and continuity conditions at the interfaces between laminae, which are satisfied in the sense of Fourier series. The formulation admits different boundary conditions at the edges and is applicable to thick and thin laminated piezoelectric composite plates. Results

for laminated composite plates with distributed piezoelectric actuators are presented for different types of boundary conditions at the edges. The analytical displacements, stresses and electric potential compare very well with those obtained by the finite element method.

2.1 Literature Review

Initially piezoelectric actuators were used to control vibrations of beams (Bailey and Hubbard (1985), Crawley and de Luis (1987)). The piezoelectric actuators used in beams are thin rectangular elements usually bonded to their outermost surfaces and are poled in the thickness direction. The application of an electric field in the thickness direction causes the actuator's lateral dimensions to change. The localized strains induced by the piezoelectric in the host structure cause it to deform. In order to effectively integrate piezoelectric materials with structural systems, it is necessary to understand better the interaction between actuators and the base structure. Mechanical models have been developed by Crawley and de Luis (1987), Crawley and Anderson (1990) and others to analyze deformations and stresses in beams with surface-bonded piezoelectric actuators. Lee (1990), Wang and Rogers (1991), Batra and Ghosh (1995), and Mitchell and Reddy (1995) have developed plate theories for composite laminates with embedded and/or surface mounted piezoelectric sensors and actuators. Numerous finite element studies have also been conducted (Allik and Hughes (1970), Robbins and Reddy (1991), Ha et al. (1992), Batra and Liang (1997b)).

Three-dimensional analytical solutions for the deformations and stresses in simply supported composite plates with piezoelectric layers have been given by Heyliger (1994), Heyliger and Brooks (1996), Heyliger and Saravanos (1995), Bisegna and Maceri (1996),

Batra et al. (1996a), Batra and Liang (1997a), Lee and Jiang (1996) and Vel and Batra (2001). If one of the plate dimensions is very large as compared to the other two dimensions, then its deformations are generally regarded as being independent of the coordinate in that direction and it is known as cylindrical bending. Exact solutions for cylindrical bending of simply supported laminated plates were developed by Heyliger and Brooks (1996) and Vel and Batra (2001), and for the cylindrical bending vibrations by Brooks and Heyliger (1995) and Yang et al. (1994). Brooks and Heyliger (1994) and Batra et al. (1996b) simulated a segmented piezoelectric actuator by applying an electric potential only over a part of a distributed piezoelectric actuator. Most of the three-dimensional analytical solutions presented in the literature are applicable only when the edges are simply supported and subjected to specific types of electric boundary conditions. However, simply supported edges are rarely encountered in practice.

Vel and Batra (2000a) developed a three-dimensional quasi-static solution using the Stroh formalism for laminated piezoelectric rectangular plates subjected to arbitrary mechanical and electrical boundary conditions. Subsequently, they presented results for quasi-static cylindrical bending deformations of a laminated plate with segmented piezoelectric patches (Vel and Batra (2000b)). The solution procedure is extended to the analysis of the cylindrical bending vibrations of piezoelectric composite plates.

Three-dimensional equations of linear piezoelectricity for generalized plane strain deformations are exactly satisfied by the chosen Fourier basis functions. Instead of assuming that the mechanical displacements and the electric field in the direction of the very large plate dimension vanish identically, the electric potential and the three components of the mechanical displacement are assumed to depend only on the two in-

plane coordinates and time. The coefficients in the series solution are determined from boundary conditions at edges and continuity conditions at the interfaces between adjoining laminae. Computed natural frequencies, displacements and stresses for thick cantilever laminates containing either distributed or segmented actuators are found to compare very well with those obtained by the finite element method.

2.2 Problem Formulation

A rectangular Cartesian coordinate system, shown in Fig. 1, was used to describe the infinitesimal quasi-static N-layer deformations of an piezoelectric composite laminate occupying the region $[0,L] \times (-\infty,\infty) \times [H^{(1)}, H^{(N+1)}]$ in the unstressed reference configuration. The laminate is of infinite extent in the x_2-direction. Planes $x_3 = H^{(1)},...,H^{(n)},...,H^{(N+1)}$ describe the bottom bounding surface, the horizontal interfaces between adjoining laminae, and the top bounding surface. Each lamina is assumed to be made of a homogeneous material.

The equations of motion in the absence of body forces are

$$\sigma_{jm,m} = \rho\ddot{u}_j, \quad (j,m = 1,2,3),$$

(1)

where σ_{jm} are components of the Cauchy stress tensor and u_j are components of the mechanical displacement vector. A comma followed by index j indicates partial differentiation with respect to the present position x_j of a material particle, a superimposed dot indicates partial derivative with respect to time t, and a repeated index implies summation over the range of the index. The charge equation in the absence of free charges is

$$D_{m,m} = 0,$$

<div align="right">(2)</div>

where D_m are the components of the electric displacement vector.

The constitutive equations of a linear piezoelectric medium are (Tiersten, 1969)

$$\sigma_{jm} = C_{jmqr}\varepsilon_{qr} - e_{rjm}E_r, \quad D_m = e_{mqr}\varepsilon_{qr} + \epsilon_{mr}E_r,$$

<div align="right">(3)</div>

where C_{jmqr} is the elasticity tensor, ε_{qr} is the infinitesimal strain tensor, e_{rjm} are the piezoelectric coefficients that describe coupling between the mechanical deformation and electric field, E_r is the electric field and ϵ_{mr} is the electric permittivity tensor. The infinitesimal strain tensor and the electric field are related to the mechanical displacement u_q and electric potential ϕ by

$$\varepsilon_{qr} = \frac{1}{2}(u_{q,r} + u_{r,q}), \quad E_r = -\phi_{,r}.$$

<div align="right">(4)</div>

The symmetry of the stress and the strain tensors and the existence of the stored energy function imply the following symmetries

$$C_{jmqr} = C_{mjqr} = C_{qrjm}, \quad e_{rjm} = e_{rmj}, \quad \epsilon_{mr} = \epsilon_{rm}.$$

<div align="right">(5)</div>
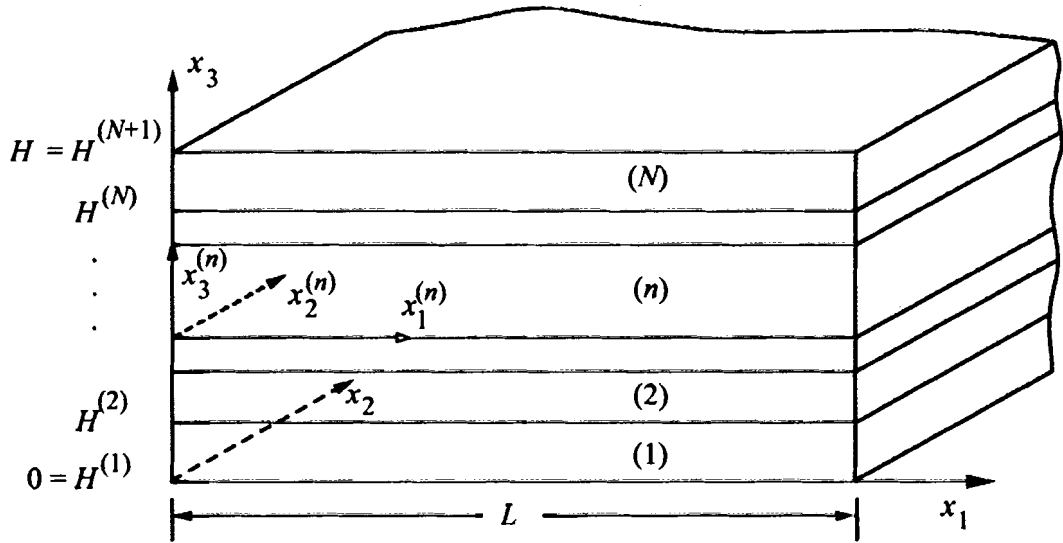
Figure 2-1 Piezoelectric Composite Plate

Material constants are assumed to yield a positive stored energy density for every non-rigid deformation and/or nonzero electric field. That is,

$$C_{jmqr}\varepsilon_{jm}\varepsilon_{qr} > 0, \quad \epsilon_{rm}E_r E_m > 0, \tag{6}$$

for every real nonzero ε_{jm} and E_r. The displacement or traction components prescribed on the edges $x_1 = 0$ and L, and bottom and top surfaces $x_3 = 0$ and H are presumed not to depend upon x_2, and are specified as follows [Ting (1996), pp.497-498]

$$\mathbf{I}_u^{(s)}\begin{bmatrix} \mathbf{u} \\ \phi \end{bmatrix} + \mathbf{I}_\sigma^{(s)}\begin{bmatrix} \boldsymbol{\sigma}_s \\ D_s \end{bmatrix} = \mathbf{f}^{(s)} \quad \text{on} \quad x_s = 0,$$

$$\tilde{\mathbf{I}}_u^{(s)}\begin{bmatrix} \mathbf{u} \\ \phi \end{bmatrix} + \tilde{\mathbf{I}}_\sigma^{(s)}\begin{bmatrix} \boldsymbol{\sigma}_s \\ D_s \end{bmatrix} = \tilde{\mathbf{f}}^{(s)} \quad \text{on} \quad x_s = L_s, \quad (s = 1,3),$$

$$\tag{7}$$

where $(\sigma_s)_k = \sigma_{ks}$ and $\mathbf{I}_u^{(s)}, \mathbf{I}_\sigma^{(s)}, \tilde{\mathbf{I}}_u^{(s)}$ and $\tilde{\mathbf{I}}_\sigma^{(s)}$ are 4×4 diagonal matrices that specify the type of boundary condition, while $\mathbf{f}^{(s)}$ and $\tilde{\mathbf{f}}^{(s)}$ are known vector functions that specify the boundary values. For most applications, these diagonal matrices have entries of either zero or one such that

$$\mathbf{I}_u^{(s)} + \mathbf{I}_\sigma^{(s)} = \tilde{\mathbf{I}}_u^{(s)} + \tilde{\mathbf{I}}_\sigma^{(s)} = \mathbf{I}, \quad (s = 1,3), \tag{8}$$

with $\mathbf{I}$ being the 4×4 identity matrix. In other words, for mechanical boundary conditions, one can specify either a component of the displacement or traction vector in each coordinate direction. The electrical boundary condition is specified by prescribing either the electric potential or the normal component of the electrical displacement vector. For example, if the surface $x_1 = 0$ is rigidly clamped and electrically grounded, then $\mathbf{I}_u^{(1)} = \mathbf{I}, \mathbf{I}_\sigma^{(1)} = \mathbf{0}$ and $\mathbf{f}^{(1)} = \mathbf{0}$, i.e. $u_1 = u_2 = u_3 = 0$ and $\phi = 0$. If the surface is free of electric charge (normal component of electric displacement vanishes) and traction free, then $\mathbf{I}_u^{(1)} = \mathbf{0}, \mathbf{I}_\sigma^{(1)} = \mathbf{I}, \mathbf{f}^{(1)} = \mathbf{0}$, i.e, $\sigma_{11} = \sigma_{12} = \sigma_{13} = 0$ and $D_1 = 0$. An example of mixed

boundary conditions would be a simply supported and electrically grounded edge for which $\mathbf{I}_u^{(1)} = \text{diag}[0,0,1,1], \mathbf{I}_\sigma^{(1)} = \text{diag}[1,1,0,0], \mathbf{f}^{(1)} = \mathbf{0}, \text{i.e}, \sigma_{11} = \sigma_{12} = 0, u_3 = 0$ and $\phi = 0$.

The interface continuity conditions on the surface $x_3 = H^{(n+1)}$ between laminae n and $n+1$ can be specified as follows:

(a) If the surface is an interface between two laminae, then displacements, surface tractions, electric potential and the normal component of the electric displacement between them are taken to be continuous. That is,

$$[\![\mathbf{u}]\!] = \mathbf{0}, [\![\sigma_3]\!] = \mathbf{0}, [\![\phi]\!] = 0, [\![D_3]\!] = 0 \quad \text{on } x_3 = H^{(n)}. \tag{9}$$

Here $[\![\mathbf{u}]\!]$ denotes the jump in the value of $\mathbf{u}$ across an interface. Thus the adjoining laminae are presumed to be perfectly bonded together.

(b) If the interface is electroded, the potential on this surface is a known function $g(x_1)$ while the normal component of the electric displacement need not be continuous across this interface, i.e.,

$$[\![\mathbf{u}]\!] = \mathbf{0}, [\![\sigma_3]\!] = \mathbf{0}, \phi = g(x_1)\cos\omega t \quad \text{on } x_3 = H^{(n)}. \tag{10}$$

It is assumed that the electrode is of negligible thickness and ignore its mechanical influence on the structure.

It is postulated that the displacement $\mathbf{u}$ and the electrical potential ϕ are functions of x_1, x_3 and time t; thus deformations of the laminate correspond to generalized plane state of deformation. This assumption is reasonable since applied loads (mechanical and electrical) and material properties are independent of x_2 and the body is of infinite extent in the x_2 direction.

11

2.3 Analytical Solution

Using a local coordinate system $x_1^{(n)}, x_2^{(n)}, x_3^{(n)}$ with origin at the point where the global x_3 axis intersects the bottom surface of the nth lamina; the local axes are parallel to the global axes (see Fig. 1). The thickness of the nth lamina is denoted by $h^{(n)} = H^{(n+1)} - H^{(n)}$. In this section, we drop the superscripts n for convenience; it is understood that all material constants and unknowns belong to this lamina.

An analytical solution is obtained by extending the Stroh (Eshelby et al., 1953; Stroh, 1958; Ting, 1996) formalism to the analysis of steady state vibrations of hybrid plates. Fourier basis functions for the mechanical displacements and the electric potential, which identically satisfy the equations of motion (1) and charge equation (2), are used to compute the solution of the boundary value problem via the superposition principle. The coefficients in the series solution are determined from the boundary conditions (7) and continuity conditions at the interfaces (9) or (10) at the interfaces between adjoining laminae.

2.3.1 Sinusoidal Basis Functions in the x_1-direction

The following form for the displacement vector and the electric potential is assumed,

$$\begin{bmatrix} \mathbf{u} \\ \phi \end{bmatrix} = \mathbf{a} \exp(\lambda i z) \cos \omega t,$$

(11)

where $z = x_1 + px_3, i = \sqrt{-1}$, λ is a real number and the vector $\mathbf{a}$ and the scalar p will be determined from the equations of motion and the charge equation. The assumed mechanical displacement and the electric potential fields in (11) vary sinusoidally in the x_1-direction and λ determines its wave length in that direction. Depending on whether p is complex or real, the assumed displacement and potential field (11) has either an exponential and/or sinusoidal variation in the x_3-direction. Substitution for $\mathbf{u}$ and ϕ from

12

(11) into (4) and for ε and $\mathbf{E}$ into (3) gives the following expressions for components

σ_{jm} of the stress tensor and D_m of the electric displacement vector

$$\sigma_{jm} = (C_{jmqr}a_q + e_{rjm}a_4)\lambda i(\delta_{r1} + p\delta_{r3})\exp(\lambda i z)\cos\omega t,$$

$$D_m = (e_{mqr}a_q - \epsilon_{mr}a_4)\lambda i(\delta_{r1} + p\delta_{r3})\exp(\lambda i z)\cos\omega t, \tag{12}$$

where δ_{rs} is the Kronecker delta. Substitution of (12) into the equation of motion (1)

gives

$$\left\{C_{j1q1} + p(C_{j1q3} + C_{q1j3}) + p^2 C_{j3q3}\right\} a_q + \left\{e_{11j} + p(e_{31j} + e_{13j}) + p^2 e_{33j}\right\}a_4 = \frac{\rho\omega^2}{\lambda^2}a_j, \tag{13}$$

which can be written as

$$\left\{\tilde{\mathbf{Q}} + p\left[\tilde{\mathbf{R}} + \tilde{\mathbf{R}}^T\right] + p^2\tilde{\mathbf{T}}\right\}\tilde{\mathbf{a}} + \left\{\mathbf{e}_{11} + p(\mathbf{e}_{31} + \mathbf{e}_{13}) + p^2\mathbf{e}_{33}\right\}a_4 = \frac{\rho\omega^2}{\lambda^2}\tilde{\mathbf{a}} \tag{14}$$

where

$$\tilde{Q}_{jq} = C_{j1q1}, \quad \tilde{R}_{jq} = C_{j1q3}, \quad \tilde{T}_{jq} = C_{j3q3}, \quad (e_{rm})_j = e_{rmj}, \quad \tilde{\mathbf{a}} = \begin{bmatrix} a_1 \\ a_2 \\ a_3 \end{bmatrix}. \tag{15}$$

Substitution for D_m from (12) into the charge equation (2) gives

$$\left\{e_{11q} + p(e_{31q} + e_{13q}) + p^2 e_{33q}\right\} a_q - \left\{\epsilon_{11} + p(\epsilon_{13} + \epsilon_{31}) + p^2\epsilon_{33}\right\} a_4 = 0, \tag{16}$$

which can be written as

$$\left\{\mathbf{e}_{11} + p(\mathbf{e}_{31} + \mathbf{e}_{13}) + p^2\mathbf{e}_{33}\right\}\tilde{\mathbf{a}} - \left\{\epsilon_{11} + p(\epsilon_{13} + \epsilon_{31}) + p^2\epsilon_{33}\right\} a_4 = 0 \tag{17}$$

The two equations (14) and (17) can be combined to obtain (Ting, 1996)

$$\left\{\hat{\mathbf{Q}} + p\left[\mathbf{R} + \mathbf{R}^T\right] + p^2\mathbf{T}\right\}\mathbf{a} = 0, \tag{18}$$

where

13

$$\hat{\mathbf{Q}} = \mathbf{Q} - \frac{\rho\omega^2}{\lambda^2}\cdot\mathrm{diag}[1,1,1,0], \quad \mathbf{Q} = \begin{bmatrix} \tilde{\mathbf{Q}} & \mathbf{e}_{11} \\ \mathbf{e}_{11}^T & -\epsilon_{11} \end{bmatrix},$$

$$\mathbf{R} = \begin{bmatrix} \tilde{\mathbf{R}} & \mathbf{e}_{31} \\ \mathbf{e}_{13}^T & -\epsilon_{13} \end{bmatrix}, \quad \mathbf{T} = \begin{bmatrix} \tilde{\mathbf{T}} & \mathbf{e}_{33} \\ \mathbf{e}_{33}^T & -\epsilon_{33} \end{bmatrix}. \tag{19}$$

Equation (18) can be stated as the following algebraic eigenvalue problem (Ting, 1996)

$$\mathbf{N}\begin{bmatrix} \mathbf{a} \\ \mathbf{b} \end{bmatrix} = p\begin{bmatrix} \mathbf{a} \\ \mathbf{b} \end{bmatrix}, \tag{20}$$

where

$$\mathbf{N} = \begin{bmatrix} -\mathbf{T}^{-1}\mathbf{R}^T & \mathbf{T}^{-1} \\ \mathbf{R}\mathbf{T}^{-1}\mathbf{R}^T - \hat{\mathbf{Q}} & -\mathbf{R}\mathbf{T}^{-1} \end{bmatrix},$$

$$\mathbf{b} = (\mathbf{R}^T + p\mathbf{T})\mathbf{a} = -\frac{1}{p}(\hat{\mathbf{Q}} + p\mathbf{R})\mathbf{a}. \tag{21}$$

The components (12) of the stress and electric displacement can be written as

$$\begin{bmatrix} \sigma_1 \\ D_1 \end{bmatrix} = \lambda i[\mathbf{Q} + p\mathbf{R}]\mathbf{a}\exp(\lambda i z)\cos\omega t,$$

$$\begin{bmatrix} \sigma_3 \\ D_3 \end{bmatrix} = \lambda i[\mathbf{R}^T + p\mathbf{T}]\mathbf{a}\exp(\lambda i z)\cos\omega t. \tag{22}$$

Since $\mathbf{N}$ is an 8×8 real matrix, there are eight eigensolutions $(p_\alpha,\mathbf{a}_\alpha), \alpha = 1,2,...,8$, to

the algebraic eigenvalue problem (20). If p is a complex eigenvalue and $\mathbf{a}$ is the

corresponding complex eigenvector, then the complex conjugates $\bar{p}$ and $\bar{\mathbf{a}}$ also form an

eigensolution. Let there be 2κ complex and $8 - 2\kappa$ real eigenvalues. They are arranged

as $p_1,...,p_\kappa,p_{\kappa+1},...,p_{2\kappa},p_{2\kappa+1},...,p_s$ such that

$$\mathrm{Im}(p_\alpha) > 0, \quad p_{\kappa+\alpha} = \bar{p}_\alpha, \quad \mathbf{a}_{\kappa+\alpha} = \bar{\mathbf{a}}_\alpha, \quad (\alpha = 1,\ldots,\kappa). \tag{23}$$

The basis function (11) constitutes one term of a Fourier series solution that will be

used to satisfy the boundary conditions on $x_3^{(n)} = 0$. Mechanical displacements, electric

potential, stresses and electric displacements vary sinusoidally in the x_1-direction on the

surface $x_3^{(n)} = 0$. For complex p_α, the basis function decays exponentially in the x_3-

direction due to the inequality in Eqn. (23). The basis functions corresponding to real p_α vary sinusoidally in the x_3-direction.

In a similar manner, the following basis functions are used to satisfy the boundary conditions on the surface $x_3 = h$ of laminae n

$$\begin{bmatrix} \mathbf{u} \\ \phi \end{bmatrix} = \mathbf{a} \exp\left[\lambda i(ph - z)\right] \cos \omega t.$$
(24)

Substitution of (24) into the equation of motion (1) and the charge equation (2) also results in the eigenvalue problem (20) for p and $\mathbf{a}$. The corresponding components of the stress tensor and electric displacement vector are

$$\begin{bmatrix} \sigma_1 \\ D_1 \end{bmatrix} = -\lambda i [\mathbf{Q} + p\mathbf{R}] \mathbf{a} \exp\left[\lambda i(ph - z)\right] \cos \omega t,$$

$$\begin{bmatrix} \sigma_3 \\ D_3 \end{bmatrix} = -\lambda i \left[\mathbf{R}^T + p\mathbf{T}\right] \mathbf{a} \exp\left[\lambda i(ph - z)\right] \cos \omega t.$$
(25)

2.3.2 Sinusoidal Basis Functions in the x_3-direction

The following form for the displacement vector and electric potential is assumed,

$$\begin{bmatrix} \mathbf{u} \\ \phi \end{bmatrix} = \mathbf{c} \exp(\xi iz/q) \cos \omega t,$$
(26)

where ξ is a real number, $z = x_1 + qx_3$ and the vector $\mathbf{c}$ and the scalar q are unknowns.

Note that $z/q = x_1/q + x_3$. The variation of the assumed mechanical displacement and electric field (26) in the x_3-direction is sinusoidal and ξ determines the wave length. Depending on whether q is complex or real, the assumed displacement and potential fields vary either exponentially and/or sinusoidally in the x_1-direction. From Eqns. (26), (4) and (3) the following is obtained

15

$$\sigma_{jm} = \frac{\xi i}{q}(C_{jmqr}c_q + e_{rjm}c_4)(\delta_{r1} + q\delta_{r3})\exp(\xi iz/q)\cos\omega t,$$

$$D_m = \frac{\xi i}{q}(e_{mqr}c_q - \epsilon_{mr}c_4)(\delta_{r1} + q\delta_{r3})\exp(\xi iz/q)\cos\omega t,$$

(27)

which is written as

$$\begin{bmatrix} \sigma_1 \\ D_1 \end{bmatrix} = \frac{\xi i}{q}[\mathbf{Q} + q\mathbf{R}]\mathbf{c}\exp(\xi iz/q)\cos\omega t,$$

$$\begin{bmatrix} \sigma_3 \\ D_3 \end{bmatrix} = \frac{\xi i}{q}[\mathbf{R}^T + q\mathbf{T}]\mathbf{c}\exp(\xi iz/q)\cos\omega t,$$

(28)

where $\mathbf{Q}$, $\mathbf{R}$ and $\mathbf{T}$ are defined in (19). Substitution of (27) into (1) and (2) gives

$$\left\{\mathbf{Q} + q\left[\mathbf{R} + \mathbf{R}^T\right] + q^2\hat{\mathbf{T}}\right\}\mathbf{c} = 0,$$

(29)

where

$$\hat{\mathbf{T}} = \mathbf{T} - \frac{\rho\omega^2}{\xi^2}\mathrm{diag}[1,1,1,0],$$

Eqn. (29) constitutes the following algebraic eigenvalue problem:

$$\mathbf{N}\begin{bmatrix} \mathbf{c} \\ \mathbf{d} \end{bmatrix} = q\begin{bmatrix} \mathbf{c} \\ \mathbf{d} \end{bmatrix},$$

(30)

where

$$\mathbf{N} = \begin{bmatrix} -\hat{\mathbf{T}}^{-1}\mathbf{R}^T & \hat{\mathbf{T}}^{-1} \\ \mathbf{R}\hat{\mathbf{T}}^{-1}\mathbf{R}^T - \mathbf{Q} & -\mathbf{R}\hat{\mathbf{T}}^{-1} \end{bmatrix},$$

$$\mathbf{d} = (\mathbf{R}^T + q\hat{\mathbf{T}})\mathbf{c} = -\frac{1}{q}(\mathbf{Q} + q\mathbf{R})\mathbf{c}.$$

(31)

Eigenvalues of (31) are arranged in the same way as those of (20). The basis function

(26) constitutes one term of a Fourier series solution used to satisfy boundary conditions

on the surface $x_1^{(n)} = 0$. Similarly, the following basis functions (32) are used to satisfy

the boundary conditions on the surface $x_1 = L$ of the lamina n

$$\begin{bmatrix} \mathbf{u} \\ \phi \end{bmatrix} = \mathbf{c}\exp[\xi i(L - z)/q]\cos\omega t,$$

(32)

The stresses and the electric displacements corresponding to the basis function (32)

are

16

$$\begin{bmatrix} \sigma_1 \\ D_1 \end{bmatrix} = -\frac{\xi i}{q}[\mathbf{Q} + q\mathbf{R}]\mathbf{c}\exp[\xi i(L - z)/q]\cos\omega t,$$

$$\begin{bmatrix} \sigma_3 \\ D_3 \end{bmatrix} = -\frac{\xi i}{q}[\mathbf{R}^T + q\mathbf{T}]\,\mathbf{c}\exp[\xi i(L - z)/q]\cos\omega t. \tag{33}$$

2.3.3 Superposition of Basis Functions

For distinct p_α, one can superimpose solutions of the form (11), (24), (26) and (32) to obtain the following mechanical displacement and electric potential fields:

$$\begin{bmatrix} \mathbf{u} \\ \phi \end{bmatrix} = \left\{ \sum_{k=0}^{\infty}\sum_{\alpha=1}^{8}\left\{ r_\alpha^{(k)}\exp(\lambda^{(k)}iz_\alpha^{(k)}) + s_\alpha^{(k)}\exp[\lambda^{(k)}i(p_\alpha^{(k)}h - z_\alpha^{(k)})] \right\} \mathbf{a}_\alpha^{(k)} \right.$$
$$\left. + \sum_{m=0}^{\infty}\sum_{\alpha=1}^{8}\left\{ v_\alpha^{(m)}\exp(\frac{\xi_\alpha^{(m)}i\,\tilde{z}_\alpha^{(m)}}{q_\alpha^{(m)}}) + w_\alpha^{(m)}\exp[\frac{\xi_\alpha^{(m)}i(L - \tilde{z}_\alpha^{(m)})}{q_\alpha^{(m)}}] \right\} \mathbf{c}_\alpha^{(m)} \right\}\cos\omega t, \tag{34}$$

where

$$\lambda^{(k)} = \begin{cases} \dfrac{k_0\pi i}{L} & \text{if } k = 0 \\[2mm] \dfrac{k\pi i}{L} & \text{if } k \geq 1 \end{cases}, \quad \xi_\alpha^{(m)} = \begin{cases} -\dfrac{m_0\pi i}{q_\alpha h} & \text{if } m = 0 \\[2mm] -\dfrac{m\pi i}{q_\alpha h} & \text{if } m \geq 1 \end{cases},$$

$$z_\alpha^{(k)} = x_1 + p_\alpha^{(k)}x_3, \tilde{z}_\alpha^{(m)} = x_1 + q_\alpha^{(m)}x_3 \text{ and } (k_0, m_0) \in (0,1). \tag{35}$$

The basis functions corresponding to $\lambda^{(0)}$ and $\xi_\alpha^{(0)}$ play the role of the constant term in the Fourier series expansion. The constants $r_\alpha^{(k)}, s_\alpha^{(k)}, v_\alpha^{(m)}$ and $w_\alpha^{(m)}$ are the Fourier coefficients in the series solution. In order to obtain real valued displacements and potentials, it is assumed that the coefficients $r_\alpha, s_\alpha, v_\alpha$, and w_α are complex for $\alpha \leq 2\kappa$ and real for $\alpha > 2\kappa$, such that

$$r_{\kappa+\alpha} = \bar{r}_\alpha, \quad s_{\kappa+\alpha} = \bar{s}_\alpha, \quad v_{\kappa+\alpha} = \bar{v}_\alpha, \quad w_{\kappa+\alpha} = \bar{w}_\alpha \text{ for } \alpha = 1,...,\kappa.$$

The components of the stress tensor and the electric displacement vector corresponding to the series solution (34), obtained by superposition of equations. (22), (25), (28), and (33), are

17

$$\begin{bmatrix} \sigma_1 \\ D_1 \end{bmatrix} = \left\{ \sum_{k=0}^{\infty} \sum_{\alpha=1}^{8} \lambda^{(k)} i \left\{ r_\alpha^{(k)} \exp(\lambda^{(k)} i z_\alpha^{(k)}) - s_\alpha^{(k)} \exp[\lambda^{(k)} i(p_\alpha^{(k)} h - z_\alpha^{(k)})] \right\} [Q + p_\alpha^{(k)} R] a_\alpha^{(k)} \right.$$
$$\left. + \sum_{m=0}^{\infty} \sum_{\alpha=1}^{8} \frac{\xi_\alpha^{(m)} i}{q_\alpha^{(m)}} \left\{ v_\alpha^{(m)} \exp(\frac{\xi_\alpha^{(m)} i \, z_\alpha^{(m)}}{q_\alpha^{(m)}}) - w_\alpha^{(m)} \exp[\frac{\xi_\alpha^{(m)} i(L - \tilde{z}_\alpha^{(m)})}{q_\alpha^{(m)}}] \right\} [Q + q_\alpha^{(m)} R] c_\alpha^{(m)} \right\} \cos \omega t,$$

(36)

$$\begin{bmatrix} \sigma_3 \\ D_3 \end{bmatrix} = \left\{ \sum_{k=0}^{\infty} \sum_{\alpha=1}^{8} \lambda^{(k)} i \left\{ r_\alpha^{(k)} \exp(\lambda^{(k)} i z_\alpha^{(k)}) - s_\alpha^{(k)} \exp\left[\lambda^{(k)} i(p_\alpha^{(k)} h - z_\alpha^{(k)}) \right] \right\} \left[R^T + p_\alpha^{(k)} T \right] a_\alpha^{(k)} \right.$$
$$\left. + \sum_{m=0}^{\infty} \sum_{\alpha=1}^{8} \frac{\xi_\alpha^{(m)} i}{q_\alpha^{(m)}} \left\{ v_\alpha^{(m)} \exp(\frac{\xi_\alpha^{(m)} i \, \tilde{z}_\alpha^{(m)}}{q_\alpha^{(m)}}) - w_\alpha^{(m)} \exp[\frac{\xi_\alpha^{(m)} i(L - \tilde{z}_\alpha^{(m)})}{q_\alpha^{(m)}}] \right\} [R^T + q_\alpha^{(m)} T] c_\alpha^{(m)} \right\} \cos \omega t.$$

(37)

2.4 Satisfaction of Boundary and Interface Conditions

The unknowns $r_\alpha^{(k)}, s_\alpha^{(k)}, v_\alpha^{(m)}, w_\alpha^{(m)}$ for each lamina are determined by imposing the interface continuity conditions and boundary conditions on all surfaces of the laminate by the classical Fourier series method. For example, let boundary conditions (7) be specified on the surface $x_3^{(1)} = 0$ of lamina 1. Multiply (7) for $s = 3$ by $\exp(j \pi i x_1 / L)$ and integrate with respect to x_1 from $-L$ to L to obtain

$$\int_{-L}^{L} \left\{ I_u^{(3)} \begin{bmatrix} u \\ \phi \end{bmatrix} + I_\sigma^{(3)} \begin{bmatrix} \sigma_3 \\ D_3 \end{bmatrix} - f^{(3)} \right\} \exp(j \frac{\pi i x_1}{L}) dx_1 = 0,$$

(38)

on $x_3^{(1)} = 0$ for $j = 0,1,2,\ldots$. In Eqn. (38) the functions multiplying the coefficients $r_\alpha^{(k)}$ and $s_\alpha^{(k)}$ ($k \neq 0$) have a sinusoidal variation in the x_1 direction and are extended over the interval $(-L,0)$ without modification since they form the basis functions on this surface. The functions multiplying $v_\alpha^{(m)}$ and $w_\alpha^{(m)}$ have an exponential or sinusoidal variation in the x_1 direction; these are extended as even functions over the interval $(-L,0)$. The functions multiplying $r_\alpha^{(0)}, s_\alpha^{(0)}$ are also extended as even functions since they play the

role of the constant term in the Fourier series expansion. The known function $\mathbf{f}^{(3)}(x_1)$ is extended in a suitable manner. The interface continuity conditions (9) or (10) can be enforced in a similar manner. Thus, upon imposing the boundary/interface conditions on all four bounding surfaces of every lamina of the laminated plate, an infinite system of linear algebraic equations for infinitely many unknown coefficients is obtained. A general theory for the solution of an infinite set of algebraic equations does not exist. However, reasonably accurate results may be obtained by truncating the series with summation indices k and m in (34) to K and $M^{(n)}$ terms respectively for the nth lamina. In general, the solution tries to maintain approximately the same wave length of the largest harmonic on all the bounding surfaces of the lamina by choosing $M^{(n)} = \text{Ceil}(K\,h^{(n)}/L)$, where $\text{Ceil}(y)$ equals the smallest integer greater than or equal to y. Thus the total number of unknowns will depend solely on the choice of integer K. Once the unknown coefficients have been evaluated by solving the truncated system of linear equations, the displacements and stresses in each lamina are obtained from (34), (36) and (37).

2.5 Finite Element Analysis

Numerical analysis of piezoelectric composite plates was performed using the Finite Element Method (ABAQUS, 2002) for comparison with the analytical solution. The piezoelectric plates were analyzed using plane strain elements. Each lamina was defined to be a two-dimensional deformable solid homogenous section. The natural frequencies of the piezoelectric plate were determined using a linear perturbation method. The accuracy of the finite element solution would depend on the number and type of elements used in the analysis. A finer mesh gives more accurate results at the cost of computational time. A mesh convergence study was conducted for both the simply

supported and cantilever cases to determine the size of elements required to obtain accurate results for comparisons with the analytical solution. Eight noded biquadratic plane strain piezoelectric quadrilateral elements were used for the piezoelectric and composite laminae. The hybrid piezoelectric composite plate consisted of either graphite epoxy or piezoelectric material. The non-zero material constants of the graphite/epoxy and the piezoceramic materials are listed in Table 1. Constraining the nodes at the interfaces to be tied together ensured perfect bonding of the lamine.

Table 2-1 Material Properties

Material Property	Graphite/epoxy	PZT-4	PZT-5A
C_{1111}(GPa)	183.443	138.499	99.201
C_{2222}(GPa)	11.662	138.499	99.201
C_{3333}(GPa)	11.662	114.745	86.856
C_{1122}(GPa)	4.363	77.371	54.016
C_{1133}(GPa)	4.363	73.643	50.778
C_{2233}(GPa)	3.918	73.643	50.778
C_{2323} (GPa)	2.870	25.6	21.100
C_{3131}(GPa)	7.170	25.6	21.100
C_{1212}(GPa)	7.170	30.6	22.600
e_{311} (C m^{-2})	0	-5.2	-7.209
e_{322} (C m^{-2})	0	-5.2	-7.209
e_{333} (C m^{-2})	0	15.08	15.118
e_{223} (C m^{-2})	0	12.72	12.322
e_{113} (C m^{-2})	0	12.72	12.322
ϵ_{11}(10^{-8} F/m)	1.53	1.306	1.53
ϵ_{22}(10^{-8} F/m)	1.53	1.306	1.53
ϵ_{33}(10^{-8} F/m)	1.53	1.1151	1.50
ρ (kg/m^3)	1590	7600	7750

2.6 Results and Discussion

A piezoelectric composite structure has a series of natural frequencies that can be arranged in ascending order as ω_j, $j=1,2,3....$ These are determined by applying a potential to the piezoelectric actuator and plotting the vertical or axial component of the displacement for a specific point in the plate as a function of the forcing frequency. The displacement becomes large at certain discrete values of the forcing frequency, which signifies the resonance phenomenon.

2.6.1 Validation of the Approach

The solution procedure and the program developed for numerical computations was validated by comparing the natural frequencies with those given by Heyliger and Brooks (1995) for the cylindrical bending vibration of a simply supported monolithic piezoelectric plate of length $L = 0.04$ m and thickness $H = 0.01$ m. The mechanical boundary conditions at the edges $x_1 = 0$ and L are specified as $u_3 = 0$, $\sigma_{11} = \sigma_{12} = 0$. The edges, and the bottom surfaces of the plate are electrically grounded to zero potential. Natural frequencies corresponding to the first axial mode of vibration are tabulated by Heyliger and Brooks (1995). A sinusoidal potential $\phi(x_1, H) = \phi_0 \sin(\pi x_1 / L) \cos \omega t$ is applied to the top surface to excite various thickness modes corresponding to the first axial mode of vibration. The plate is made of PZT-4 whose nonzero material constants are given in Table 2-1. The axial displacement $u_1(0,0)$ is plotted as a function of the normalized forcing frequency $\bar{\omega}$ in Fig. 1-2, where $\bar{\omega} = \omega(L^2 / H)\sqrt{\rho_0 / C_0}$, $\rho_0 = 7600 \, \text{kg/m}^3$ and $C_0 = 138.499$ Gpa. The axial displacement becomes large at $\bar{\omega} = 2.2603, 10.087, 24.088, 41.663$, and 49.511, which are natural frequencies of the

22

plate. It should be noted that the same set of natural frequencies would be obtained if the transverse displacement $u_3(L/2,0)$ is plotted as a function of the forcing frequency ω. The mode shapes corresponding to the natural frequencies are shown next to the peaks in the displacement vs. frequency curve in Fig. 2-2. Natural frequencies corresponding to the higher axial modes of vibration can be obtained by applying a sinusoidal potential $\phi(x_1, H) = \phi_0 \sin(q\pi x_1 / L)\cos\omega t$ to the top surface of the piezoelectric plate, where q is an integer that determines the axial mode.
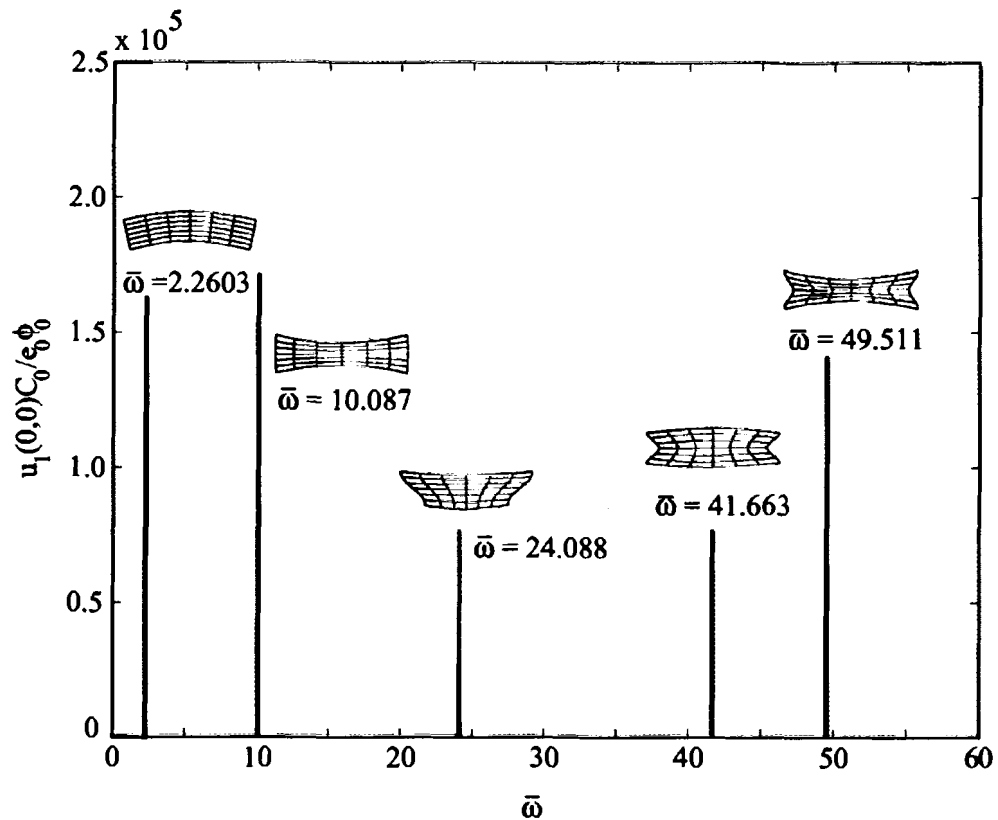
Figure 2-2 First Five Normalized Natural Frequencies and Mode Shapes

Finite element (FE) analysis was also performed using ABAQUS (ABAQUS, 2002) for comparison. The FE solution is based on the plane strain assumption in which $u_3 = 0$

and u_1, u_2 and ϕ are functions of x_1, x_2, and t. The FE mesh consisted of 10,000 eight nodded biquadratic elements. The first five thickness modes corresponding to the first axial mode of vibration obtained from our analytical solution are compared with those given by Heyliger and Brooks(1995) and the FE method in Table 2-2. The natural frequencies from the three solution procedures are nearly identical. The computational effort required to obtain the Fourier coefficients for the analytical solutions nearly the same as the effort required for the FE analysis. However, it should be noted that the analytical solution satisfies the equation of motion and charge equation exactly at every point within the body. In comparison, the FE solution satisfies the governing differential equations at the quadrature points, but not at every point within the body. Furthermore, once a computer program has been developed to compute the Fourier coefficients, the input is essentially trivial and discretization of the domain is not required.

Table 2-2 Normalized natural frequencies $\bar{\omega}$ of a simply supported thick piezoelectric plate ($L/H = 4$)

Thickness Mode	Present Analysis	Heyliger and Brooks (1995)	Finite Element Analysis
1	2.2603	2.2606	2.2602
2	10.087	10.082	10.087
3	24.088	24.086	24.085
4	41.663	41.700	41.663
5	49.511	49.616	49.511

2.6.2 Monolithic Thick Cantilever Piezoelectric Plate

The second example consists of homogenous monolithic PZT-5A piezoelectric plates. The dimensions are $L = 0.1$ m and $H = 0.025$ m. All four faces of the plate, $x_3 = 0$, $x_3 = H$, $x_1 = 0$, $x_1 = L$ are electrically grounded. The edge $x_1 = 0$ is clamped (i.e., $u_1 = u_2 = u_3 = 0$) and the edge $x_1 = L$ is traction free (i.e., $\sigma_{11} = \sigma_{12} = \sigma_{13} = 0$).

24

The effects of the truncation of the series on the accuracy of the natural frequencies, stresses, and electrical potential corresponding to the first mode of vibration is investigated by computing the solution at specific points in the laminate. The first natural frequency and the corresponding stresses, and electrical potential at specific points of the piezoelectric plate are listed in Table 2-3 for increasing number of terms K. The natural frequencies, stresses, and electrical potentials are normalized as

$$\bar{\omega}_j = \omega_j (L^2 / H)\sqrt{\rho_0 / C_0}, \quad \bar{\sigma}_{ij} = \sigma_{ij} L / C_0 u_3(L,H), \quad \bar{\phi} = \phi e_0 / C_0 u_3(L,H) \quad \text{where } \rho_0 =$$

7750 kg/m^3, $C_0 = 99.201$ Gpa, $e_0 = -7.209$ C m^{-2}. These results show that the natural frequencies, mechanical displacements, stresses and electric potential converge rapidly. A convergence study of stresses and electric potential at specific points in the plate corresponding to the fundamental frequency was conducted to determine the number of terms in the analytical model, and the number of elements required for the FEA model to obtain accurate values. Although the stresses and electrical potential show convergence, more than 220 terms are required for a complete convergence of the stresses and electrical potential. The stresses and electrical potentials used for the study and their corresponding locations are $\sigma_{11}(L/8,0)$, $\sigma_{13}(L/8,H/2)$ and $\phi(L/8,H/2)$. The FE model consisted of $16(n+1)$ divisions in the x_1 direction and $4(n+1)$ division in the x_3 direction. This scheme ensured that the stress and electrical potential values were extracted from nodes in the same geographic location for each case with different number of elements. The normalized analytical and FE results are shown in Table 2-3 and Table 2-4, respectively.

Table 2-3 Analytical Model Convergence Results for a Monolithic Thick Cantilever Piezoelectric Plate

K	ϖ	σ_{11}	σ_{13}	ϕ
10	9.148541×10^{-1}	3.271304×10^{-1}	3.312691×10^{-2}	9.889336×10^{-4}
20	8.775033×10^{-1}	2.523880×10^{-1}	3.158096×10^{-2}	9.874735×10^{-4}
40	8.656462×10^{-1}	2.743018×10^{-1}	3.049359×10^{-2}	9.911373×10^{-4}
80	8.620169×10^{-1}	2.692546×10^{-1}	3.014953×10^{-2}	9.936037×10^{-4}
100	8.616004×10^{-1}	2.661953×10^{-1}	3.010031×10^{-2}	9.939445×10^{-4}
120	8.614300×10^{-1}	2.710624×10^{-1}	3.007864×10^{-2}	9.941365×10^{-4}
140	8.613103×10^{-1}	2.736648×10^{-1}	3.006372×10^{-2}	9.943607×10^{-4}
180	8.611699×10^{-1}	2.662134×10^{-1}	3.011877×10^{-2}	9.939837×10^{-4}
220	8.611582×10^{-1}	2.726830×10^{-1}	3.003891×10^{-2}	9.946836×10^{-4}

Table 2-4 ABAQUS Convergence Results for a Monolithic Thick Cantilever Piezoelectric Plate

n	# elements	ϖ	σ_{11}	σ_{13}	ϕ
1	256	8.62502×10^{-1}	2.710433×10^{-1}	3.05570×10^{-2}	9.98858×10^{-4}
2	576	8.6194×10^{-1}	2.70842×10^{-1}	3.02506×10^{-2}	9.97179×10^{-4}
3	1024	8.61659×10^{-1}	2.70744×10^{-1}	3.01441×10^{-2}	9.96423×10^{-4}
4	1600	8.61519×10^{-1}	2.70684×10^{-1}	3.00945×10^{-2}	9.96009×10^{-4}
6	3136	8.61449×10^{-1}	2.70631×10^{-1}	3.00578×10^{-2}	9.95668×10^{-4}
12	10816	8.61238×10^{-1}	2.70539×10^{-1}	3.00221×10^{-2}	9.95144×10^{-4}
20	28224	8.61168×10^{-1}	2.70509×10^{-1}	3.00148×10^{-2}	9.94992×10^{-4}
22	33856	8.61168×10^{-1}	2.70505×10^{-1}	3.00140×10^{-2}	9.94970×10^{-4}

The through-the-thickness distributions of the normalized electric potential ϕ, longitudinal stress σ_{11}, and transverse shear stress σ_{13} at two sections along the span of the monolithic plate are shown in figures 2-3, 2-3, 2-4, and 2-5 respectively with the corresponding FE analysis data (ABAQUS, 2002) shown as squares. The results plotted are from the most accurate results of the convergence study; $K = 220$ and $n = 22$ for the analytical and FE models, respectively. The data in the plots have been normalized per the normalization equations discussed earlier in this section. The electrical potential ϕ,

and the transverse shear stress σ_{13} have a parabolic variation in their thickness direction, and the section closest to the clamped boundary exhibited the largest values. The normal stress σ_{11} is almost an affine function of the thickness coordinate for both paths. All three figures show good agreement between the FE and analytical results.
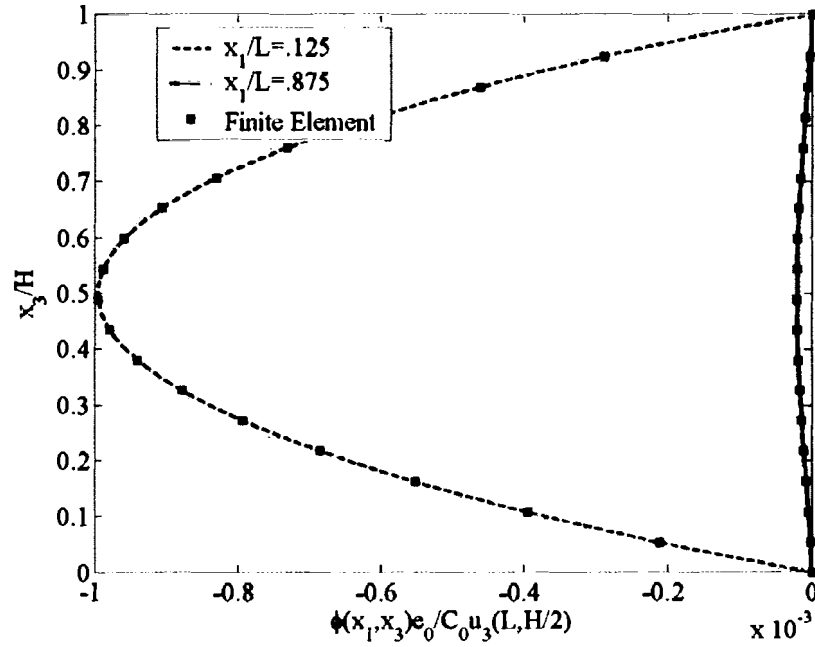
Figure 2-3 Analytical and FE Electrical Potential Variation Through-The-Thickness of the Monolithic Thick Cantilever Plate
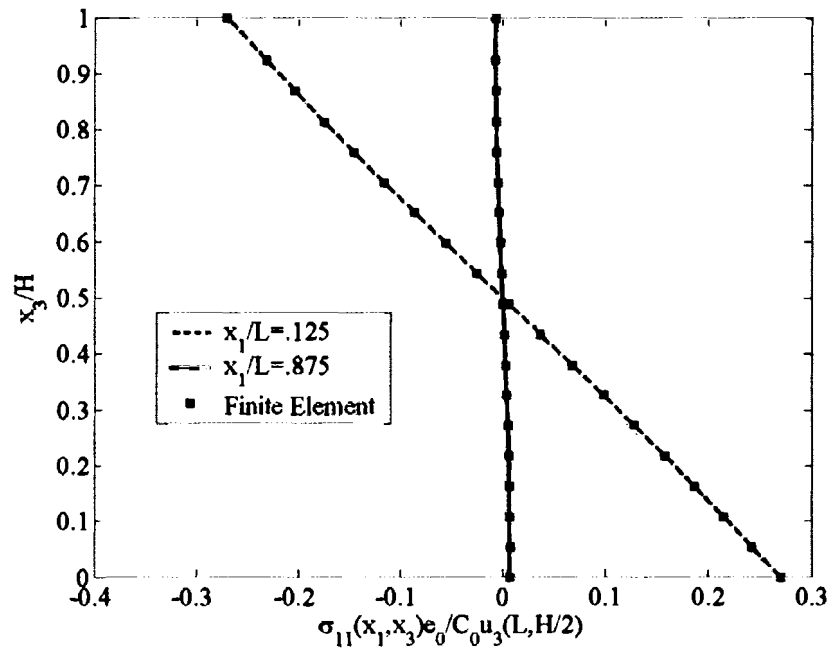
Figure 2-4 Analytical and FE Longitudinal Stress Variation Through-The-Thickness of the Monolithic Thick Cantilever Plate
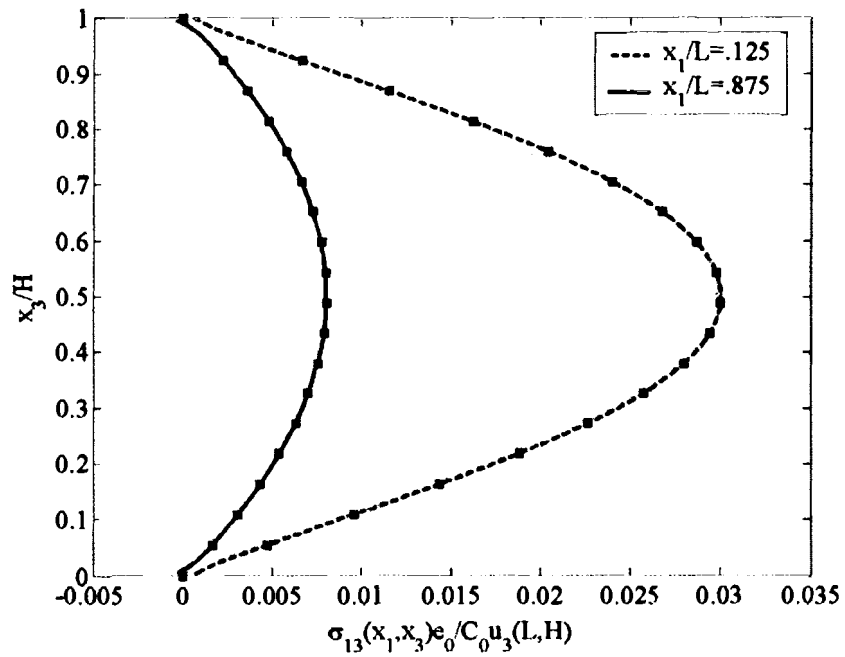
Figure 2-5 Analytical and FE Transverse Shear Stress Variation Through-The-Thickness of the Monolithic Thick Cantilever Plate

2.6.3 Two-layer Cantilever Composite Plate

Consider a two-ply piezoelectric composite laminate with the bottom layer made of graphite/epoxy with fibers parallel to the x_1-axis and the top layer made of PZT-5A. The dimensions of the composite plate are $L = 0.1$ m, $H = 0.025$ m and both layers are of equal thickness. The edge $x_1 = 0$ is clamped (i.e., $u_1 = u_2 = u_3 = 0$) and the edge $x_1 = L$ is traction free (i.e., $\sigma_{11} = \sigma_{12} = \sigma_{13} = 0$). The edges and top surface of the PZT-5A layer are electrically grounded to zero potential. The interface between the PZT-5A and graphite/epoxy layers is electroded and electrically grounded to zero potential.

The effect of truncation of the series on the accuracy of the natural frequencies, displacements and stress corresponding to the first mode of vibration is investigated by computing the solution at specific points in the laminate. The fundamental frequency and corresponding displacements, electric potential and stresses at specific points of the piezoelectric composite laminate are listed in Table 2-5 for increasing number of terms K, where $\rho_0 = 7750$ kg/m^3, $C_0 = 99.201$ GPa and $e_0 = -7.209$ C m^{-2}. The natural frequencies are normalized as $\bar{\omega}_j = \omega_j (L^2 / H)\sqrt{\rho_0 / C_0}$,. These results show that the natural frequencies, mechanical displacements, stresses and electric potential converge rapidly. The results in this section are computed using $K = 400$.

Table 2-5 Convergence Study for the Graphite/Epoxy-PZT5A Cantilever Composite
Laminate ($L/H = 5$)

K	$\frac{\omega_1 L^2}{H}\sqrt{\frac{\rho_0}{C_0}}$	$\frac{u_3(\frac{L}{2},\frac{H}{2})}{u_3(L,\frac{H}{2})}$	$\frac{u_1(\frac{L}{2},H)}{u_3(L,\frac{H}{2})}$	$\frac{10^5\phi(\frac{L}{2},\frac{3H}{4})\epsilon_0}{C_0 u_3(L,\frac{H}{2})}$	$\frac{10\sigma_{11}(\frac{L}{4},0)L}{C_0 u_3(L,\frac{H}{2})}$	$\frac{10\sigma_{13}(\frac{L}{4},\frac{3H}{4})L}{C_0 u_3(L,\frac{H}{2})}$
50	1.1164	0.4034	−0.1470	8.279	2.747	0.2416
100	1.1149	0.4031	−0.1471	8.345	2.746	0.2409
150	1.1146	0.4032	−0.1471	8.362	2.743	0.2408
200	1.1145	0.4032	−0.1471	8.368	2.744	0.2408
250	1.1144	0.4032	−0.1472	8.371	2.746	0.2408
300	1.1144	0.4032	−0.1472	8.374	2.747	0.2408
350	1.1144	0.4032	−0.1472	8.375	2.746	0.2408
400	1.1144	0.4032	−0.1472	8.375	2.746	0.2408

The first 12 mode shapes and the corresponding natural frequencies are shown in figure 2-6. The mode shapes are depicted by plotting the deformed shapes of material lines that in the reference configuration are parallel to the x_1- and x_3-axes. There is significant change in the thickness of the laminate for modes 9 and 12.

The through-the-thickness variation of the electric potential ϕ, axial displacement u_1, longitudinal stress σ_{11} and transverse shear stress σ_{13} at three sections along the span of the laminate for the first mode of vibration are shown in figures 2-7, 2-8, 2-9, and 2-10 along with values obtained from FE analysis (ABAQUS, 2002) shown by the black squares. Since displacements and stresses at a natural frequency are very large, they have been normalized by the value of the tip deflection, u_3(L,H/2). The analytical and FE values are almost identical. The electric potential ϕ in the piezoelectric layer has a parabolic variation in the thickness direction. The longitudinal stress σ_{11} is discontinuous at the interface $x_3/H = 0.5$ due to the discontinuity in the material properties of the two layers. The transverse shear stress σ_{13} is parabolic at the mid-span $x_1/L = 0.5$, it deviates

from the parabolic profile near the clamped and free edges. The axial variations of the electric potential, transverse deflection, longitudinal stress and transverse shear stress are depicted in figures 2-11, 2-12, 2-13, and 2-14. A steep variation of the electric potential ϕ and of the transverse shear stress σ_{13} is observed at the clamped edge. Here too, the analytical and FE results are in good agreement.

Mode 1: $\omega = 1.114$	Mode 2: $\omega = 4.316$	Mode 3: $\omega = 8.015$
Mode 4: $\omega = 9.737$	Mode 5: $\omega = 15.16$	Mode 6: $\omega = 18.93$
Mode 7: $\omega = 21.39$	Mode 8: $\omega = 26.67$	Mode 9: $\omega = 28.53$
Mode 10: $\omega = 29.38$	Mode 11: $\omega = 33.80$	Mode 12: $\omega = 37.26$
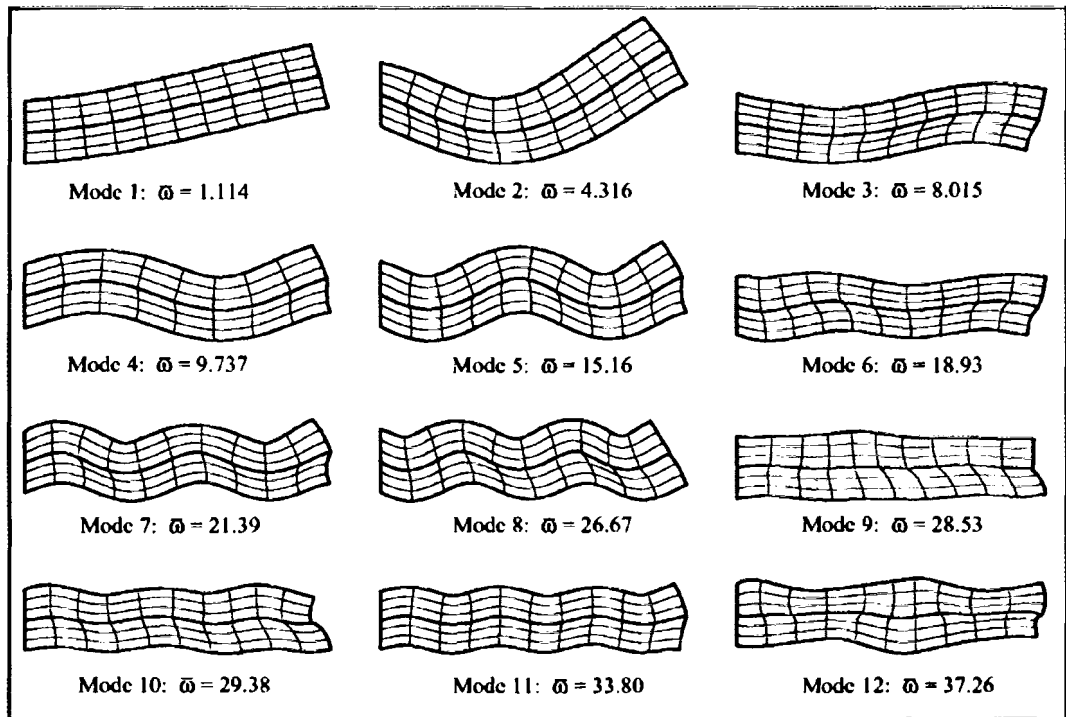
Figure 2-6 First Twelve Mode Shapes and Normalized Natural Frequencies for the Two-Layer Cantilever Plate

31

Figure 2-7 Analytical and FE Electrical Potential Variation Through-The-Thickness of the Two-Layer Thick Cantilever Plate for Mode 1

Figure 2-8 Analytical and FE Axial Displacement Variation Through-The-Thickness of the Two-Layer Thick Cantilever Plate for Mode 1

Figure 2-9 Analytical and FE Longitudinal Stress Variation Through-The-Thickness of the Two-Layer Thick Cantilever Plate for Mode 1

Figure 2-10 Analytical and FE Transverse Shear Stress Variation Through-The-Thickness of the Two-Layer Thick Cantilever Plate for Mode 1

33
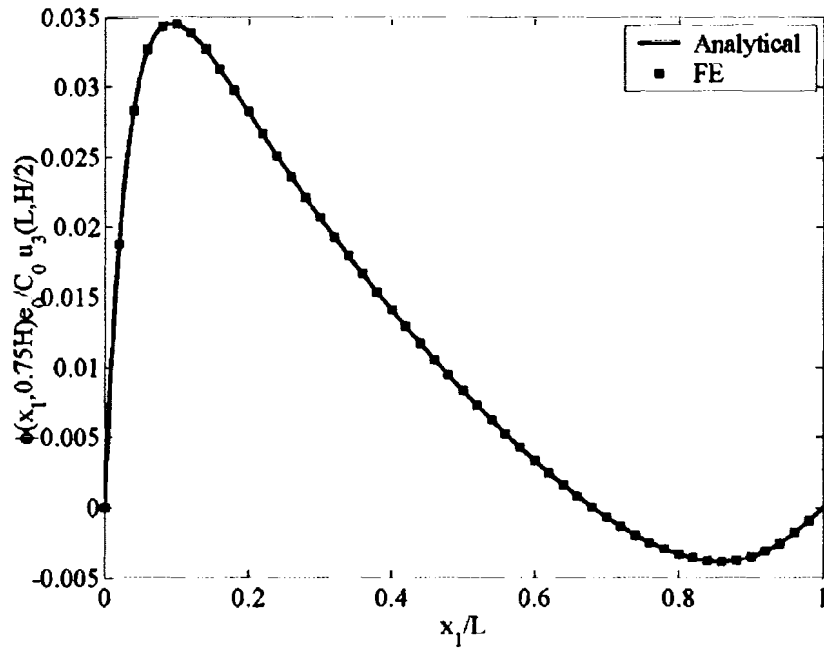
Figure 2-11 Analytical and FE Axial Electrical Potential Variation of the Two-Layer Thick Cantilever Plate for Mode 1
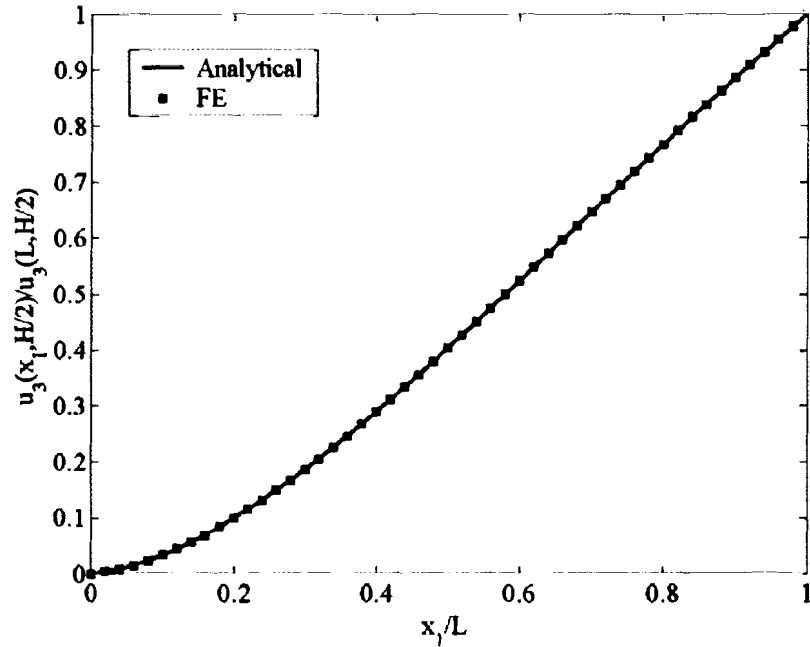
Figure 2-12 Analytical and FE Axial Transverse Displacement Variation of the Two-Layer Thick Cantilever Plate for Mode 1
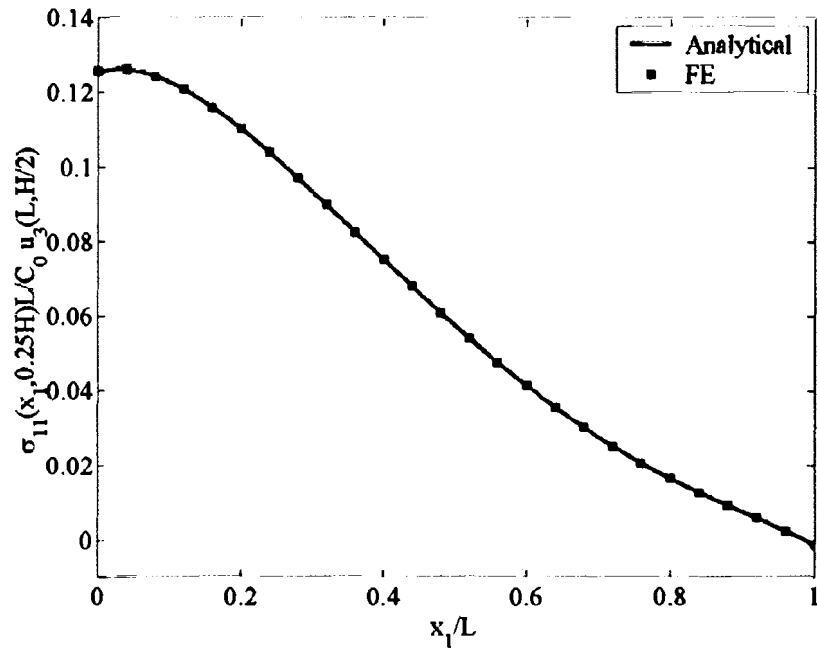
Figure 2-13 Analytical and FE Axial Longitudinal Stress Variation of the Two-Layer Thick Cantilever Plate for Mode 1
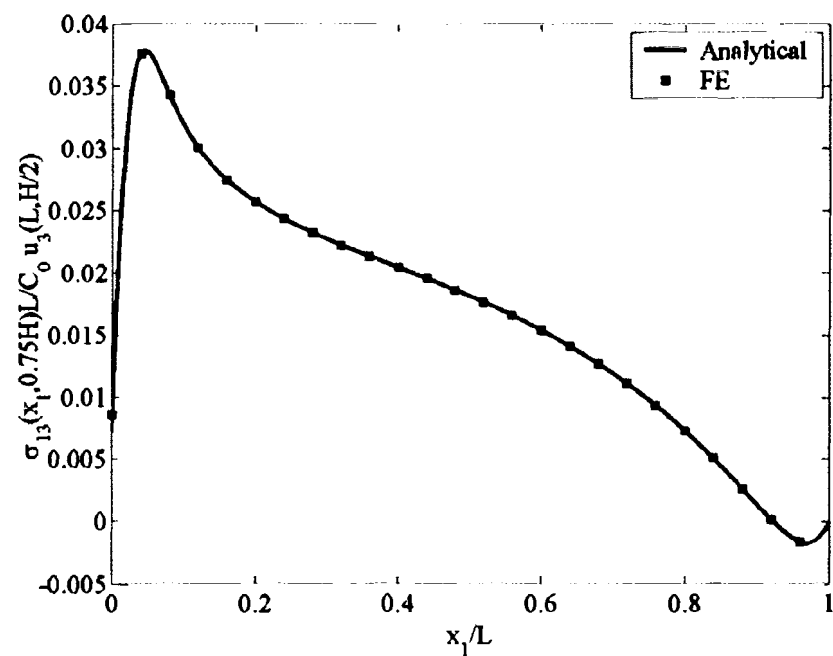
Figure 2-14 Analytical and FE Axial Transverse Displacement Variation of the Two-Layer Thick Cantilever Plate for Mode 1

35

The through-the-thickness distributions of the normalized axial displacement u_1, electric potential ϕ, longitudinal stress σ_{11} and transverse shear stress σ_{13} at four sections along the span of the cantilever laminate for the second mode of vibration are shown in figures 2-15, 2-16, 2-17, and 2-18. Although the axial displacement u_1 is an affine function of the thickness coordinate at the mid-span $x_1/L = 0.5$, it is nonlinear near the clamped edge $x_1 = 0.1L$ and the free edge $x_1/L = 0.9$ (see Figure 2-15). It should be noted that the transverse shear stress does not have a parabolic profile in the thickness direction as is usually the case for anisotropic monolithic plate.
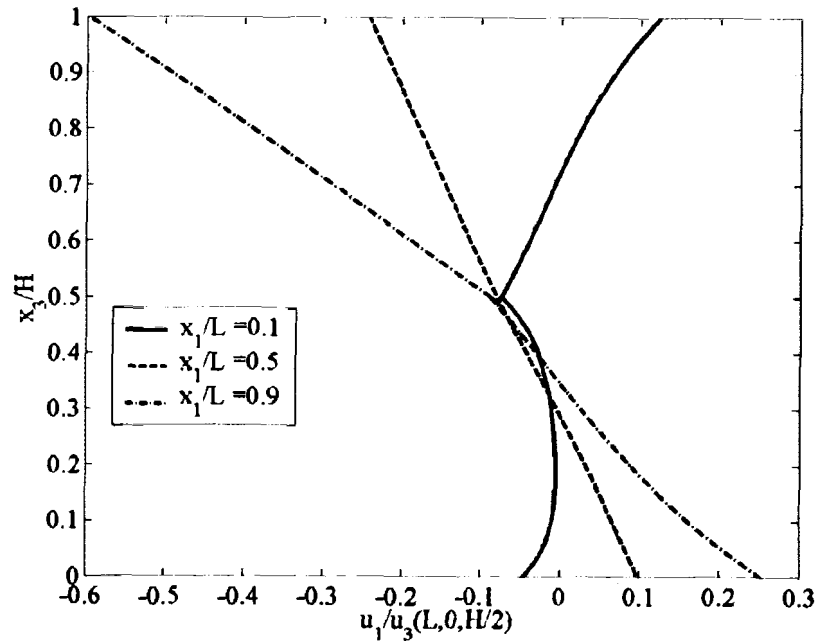
Figure 2-15 Analytical Axial Displacement Variation Through-The-Thickness of the Two-Layer Thick Cantilever Plate for Mode 2
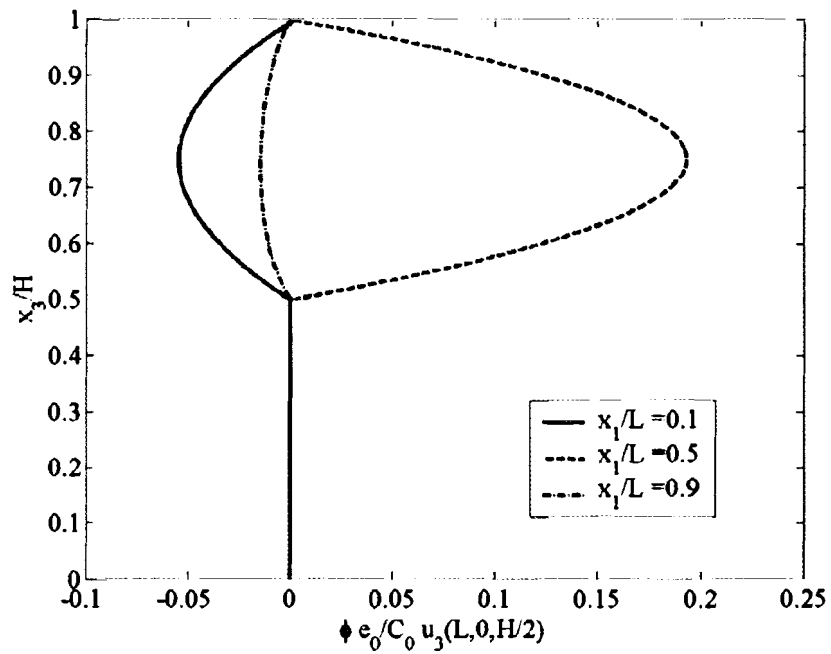
Figure 2-16 Analytical Electrical Potential Variation Through-The-Thickness of the Two-Layer Thick Cantilever Plate for Mode 2
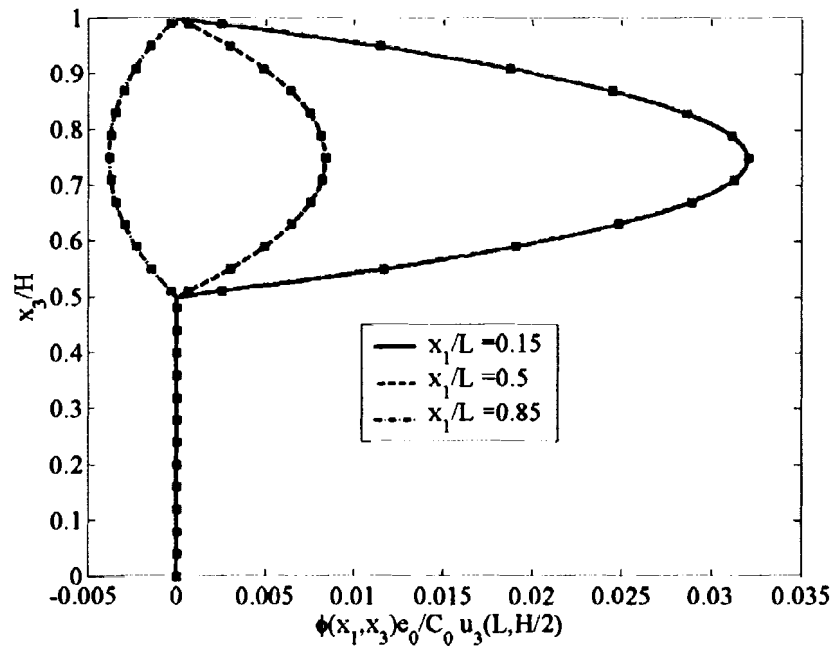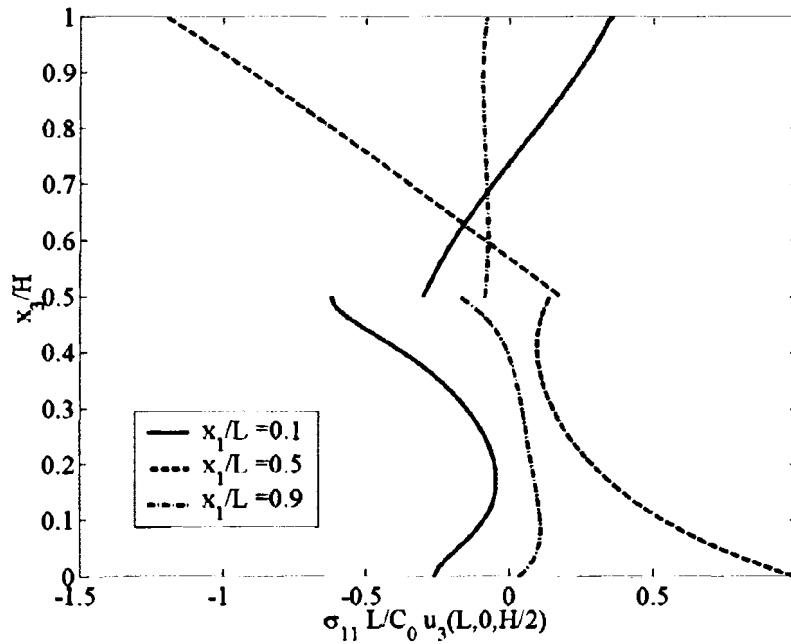

Figure 2-17 Analytical Longitudinal Stress Variation Through-The-Thickness of the Two-Layer Thick Cantilever Plate for Mode 2
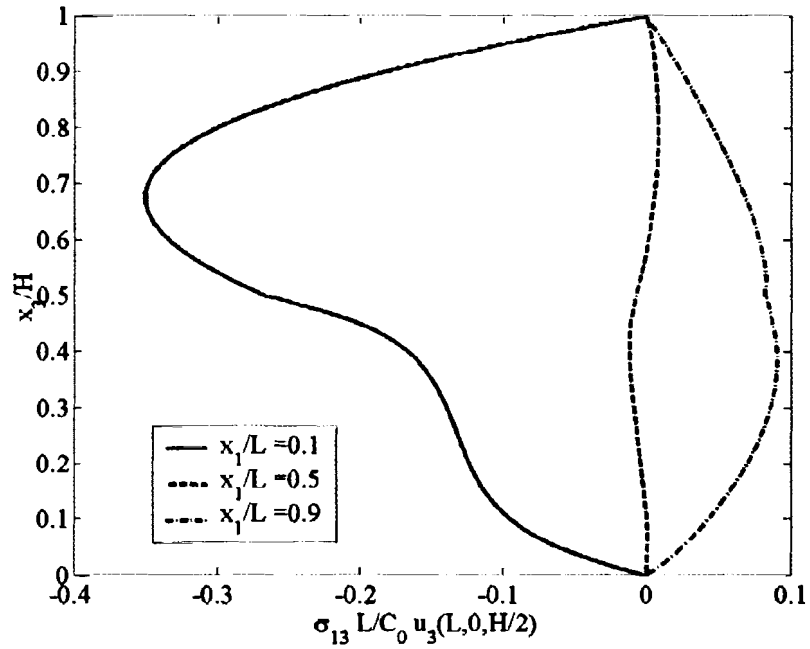
Figure 2-18 Analytical Transverse Shear Stress Variation Through-The-Thickness of the Two-Layer Thick Cantilever Plate for Mode 2

Figures 2-19, 2-20, 2-21, and 2-22 exhibit the through-the-thickness variation of the axial displacement and stresses for the third mode of vibration. The axial displacements of all points in the thickness direction have the same sign, thus indicating that this is primarily an axial mode of vibration. The transverse shear stress σ_{13} is very large at the interface between the PZT-5A and the graphite/epoxy layers near the clamped and free edges of the plate. The transverse normal stress σ_{33} is depicted in Figure 2-22. The longitudinal stress σ_{11} is an order of magnitude larger than the transverse shear stress σ_{13}, which in turn is an order of magnitude larger than the transverse normal stress σ_{33}.

38
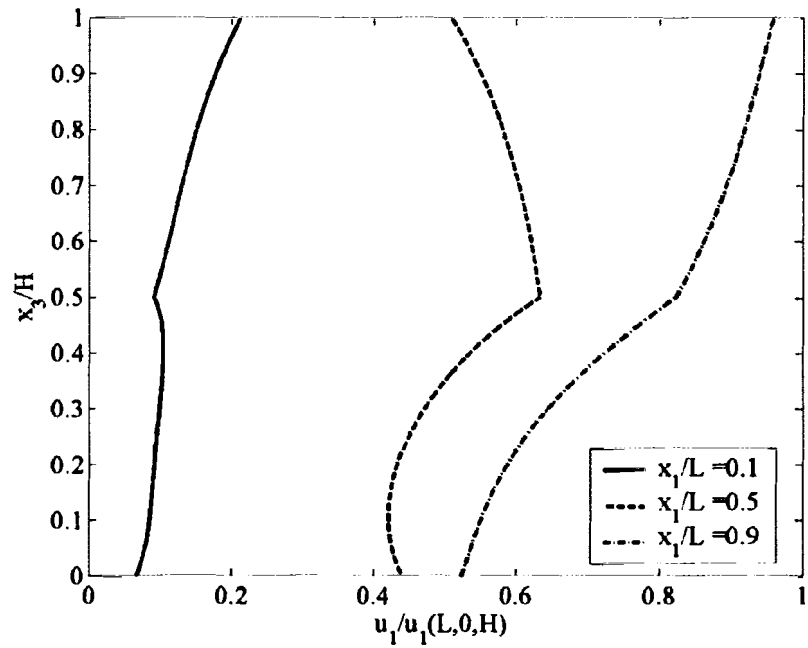
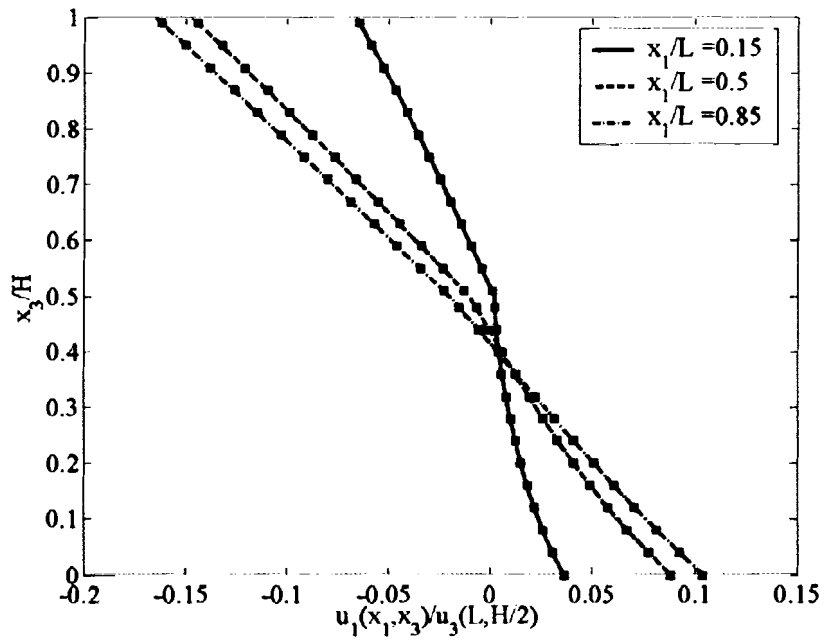Figure 2-19 Analytical Axial Displacement Variation Through-The-Thickness of the
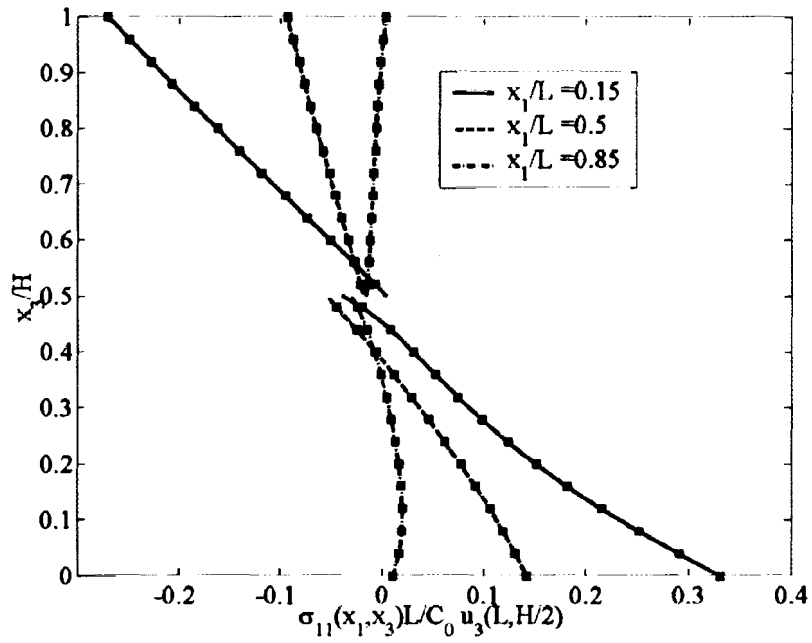Two-Layer Thick Cantilever Plate for Mode 3
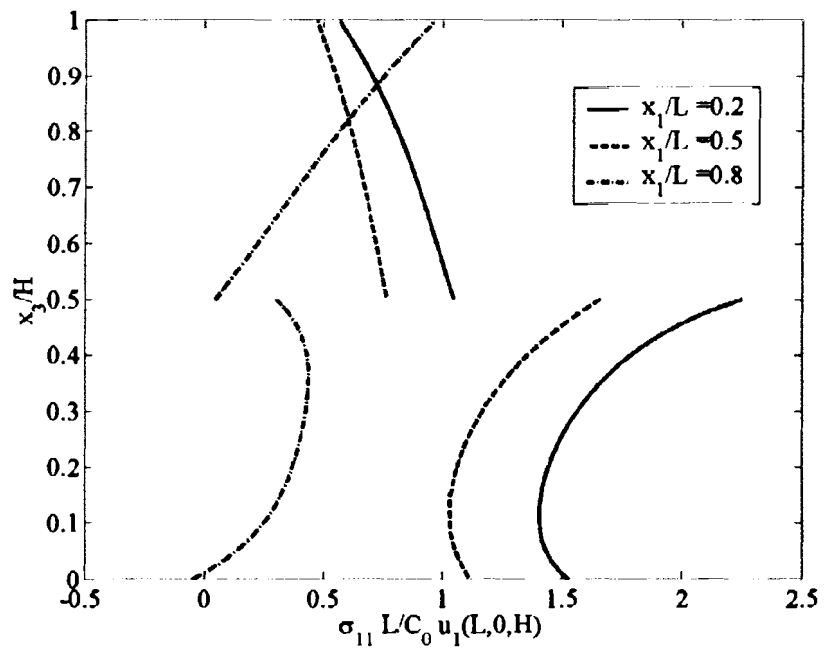
Figure 2-20 Analytical Longitudinal Stress Variation Through-The-Thickness of the
Two-Layer Thick Cantilever Plate for Mode 3

39
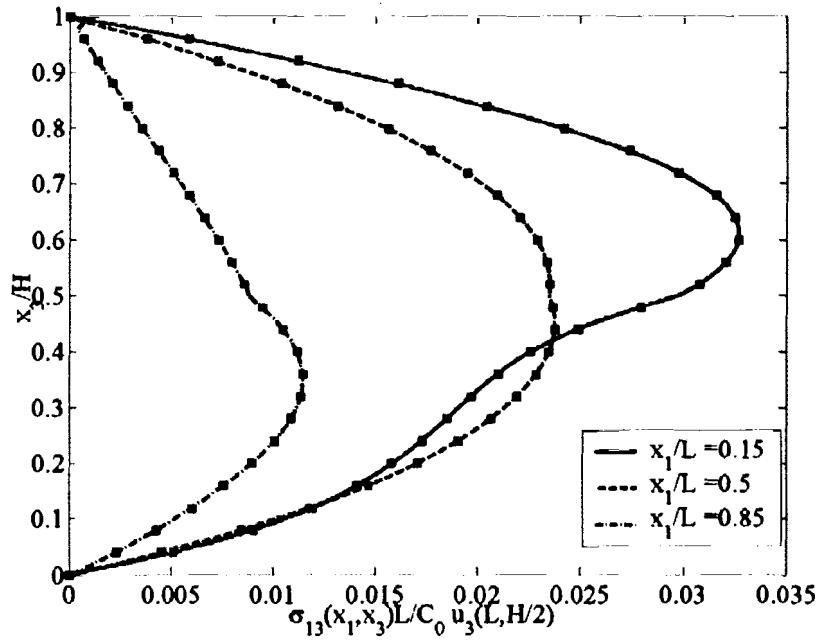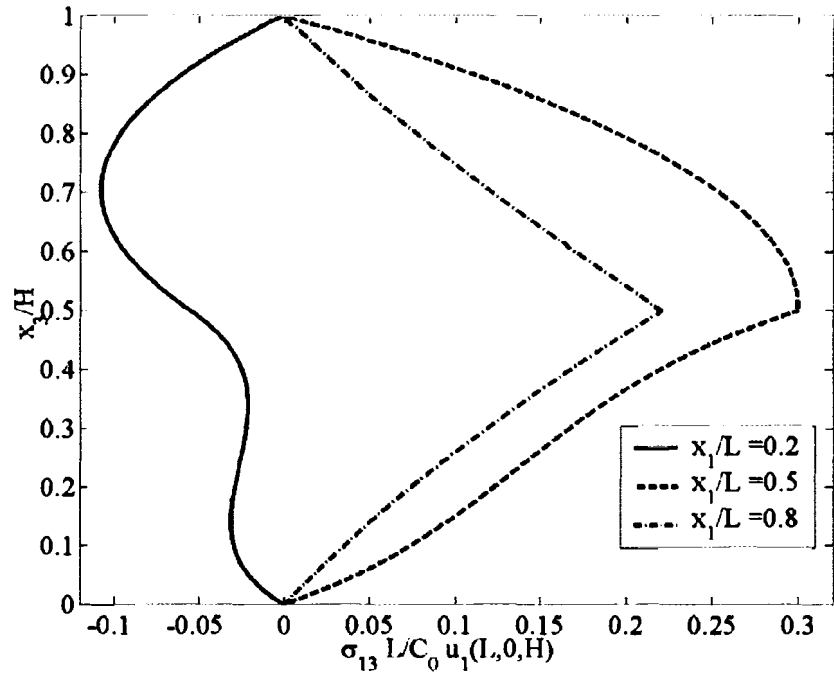
Figure 2-21 Analytical Transverse Shear Stress Variation Through-The-Thickness of the Two-Layer Thick Cantilever Plate for Mode 3
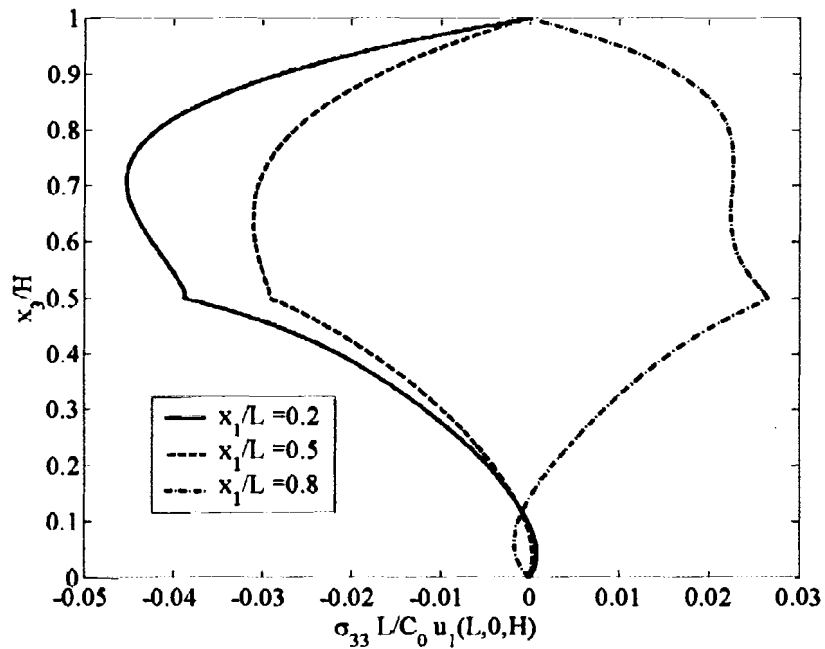

Figure 2-22 Analytical Transverse Normal Stress Variation Through-The-Thickness of the Two-Layer Thick Cantilever Plate for Mode 3

2.6.4 Conclusions

The Stroh formalism has been extended to obtain an analytical solution for the steady state vibration of a composite plate with either surface mounted or embedded piezoelectric patches. Fourier basis functions for the mechanical displacements and electric potential that identically satisfy the equations of motion and charge equation of electrostatics are used to solve the boundary value problem via the superposition principle. The boundary conditions at the edges and continuity conditions at interfaces between adjoining laminae are satisfied in the sense of Fourier series. The mechanical displacements, electric potential, stresses and electric displacement can be computed to a desired degree of accuracy by retaining sufficiently large number of terms in the series solution.

The solution procedure is validated by comparing the natural frequencies of a simply supported thick piezoelectric plate with those given by Heyliger and Brooks (1995). The first twelve natural frequencies and modes shapes for a two-layer graphite/epoxy-PZT cantilever composite plate were computed. The analytical displacements, stresses and electric potential compare very well with those obtained by the finite element method. As illustrated by the results, the method is versatile and capable of analyzing piezoelectric composite plates subjected to arbitrary boundary conditions.

3. STRUCTURAL HEALTH MONITORING OF BOLTED COMPOSITE PANELS USING PIEZOELECTRIC ACTUATORS AND SENSORS

The purpose of this study is to determine the effectiveness of different vibration-based techniques for the detection of loose bolts around the perimeter of a square composite plate. If a bolt becomes loose, then a method capable of determining the serverity and location of the loose bolt would be of great interest. The United States Navy has particular interest in detecting degradation of bolted composite connections due to bolt loosening because of their current research in developing composite hull forms. The U.S. Navy currently has a technical goal to develop systems that use composite materials. One item of concern for the U.S. Navy is composite bolted connections that loosen with time due to vibration and creep in the composite. Naturally, the U.S. Navy would be interested in methods that are capable of detecting degradation of bolted connections so to avoid catastrophic failures.

This section begins with a literature review of previous work in the field of structural health monitoring using vibration techniques, and then continues to a chosen few methods for case specific investigation. In particular, a method using transfer functions and transmittance functions to detect damage is focused upon. The theory of transfer and transmittance functions used in the investigated damage detection schemes is presented. The experimental hardware employed, and procedures followed for all of the experiments are also presented, as well as the respective results and discussions. This chapter ends with a discussion of conclusions drawn from the experimental results.

3.1 Literature Review

The development of structural health monitoring and damage detection schemes has been the focus of much research, especially for the health monitoring of composite structures. Composite materials are used increasingly in engineering applications because of their high specific stiffness and strength. However, they are susceptible to many types of damage such as moisture absorption, matrix cracking, fiber breakage or pullout and delamination. Composite joints in particular are susceptible to fatigue, bolt loosening due to creep, temperature effects and moisture absorption. There are several structural health monitoring techniques currently available. There has not been much research on the structural health monitoring of bolted composite panels, although ideas from other methods that have been reported in the literature can be applied to this problem.

The fundamental idea behind vibration-based damage detection techniques is that changes in the physical properties of a system will alter a system's modal properties. Thus changes in mass, damping, and stiffness of a system should lead to measurable changes in the system's dynamic properties, such as the natural frequencies, mode shapes and damping. Comprehensive literature reviews on the subject of structural health monitoring can be found in references (Doebling et al.,1996), (Farrar et al.,1997) and (Zou et al., 2000). Three of the major structural health monitoring techniques discussed here are techniques using impedance sensors, transfer functions and transmittance functions.

The use of statistical analysis procedure was applied to a vibration based damage detection scheme by (Fugate et al., 2001). Statistical pattern recognition is applied to the problem of damage detection in this paper. This method relies on measuring a healthy

43

system's characteristics first, and then generating errors as the system's characteristics deviate when damage occurs. Damage was detected when a statistically significant number of error terms occurred outside a determined control limit.

A passive control technique using piezoelectric materials was used to detect damage (Lew and Juang, 2002). In this method, the natural frequencies of a system are identified to detect damage in a closed loop system, and stability is ensured. A system's damping almost always increases when a virtual passive controller is added.

Techniques based on neural networks require a model to "train" the system to be able to detect damage (Wang and Huang, 2000). Zubaydi et al. (2002) investigated the damage detection of composite ship hulls using neural networks (Zubaydi, 2002). They developed a Finite Element model for a stiffened plate to simulate dynamic response of the structure with and without damage. They were successful in identifying crack length and location on the faceplate.

Very small damages in composite materials, such as cracks, were successfully found using wavelet analysis (Yan and Yam, 2002). They used a Finite Element model and micro-mechanics theory of composite damage. A crack size as small as 0.06% of the total plate area can be efficiently detected using the wavelet analysis technique.

An interesting method of detecting damage was presented by (Todd et al., 2001) using a state-space method. A novel feature called the *local attractor variance ratio* was presented. The paper showed how through a chaotic excitation a robust method was developed to detect structural damage using a states space method.

Localized flexibility matrices properties were the focus of the model-based structural damage detection investigated by (Park et al., 1998). The three flexibility methods

44

investigated were; a free-free substructural flexibility method, a deformation-based flexibility method, and a strain-basis flexibility method. The structural damage detection methods were based on the relative changes in localized flexibility.

Often damage detection is shown theoretically to work, and then investigated experimentally. Kim presented one such paper, where he used a finite element analysis package (ABAQUS, 2002) to evaluate a two-span continuous beam with modeled damage. A derived algorithm was used to predict the locations and severities of damage using changes in modal characteristics (Kim, 2002). Banks and Emeric (1998) used a Galerkin method to approximate the dynamic response of structures with piezoelectric patches acting as sensors and actuators. Non-symmetrical damage such as a cut that extended part of the way into a beam was investigated. The analytical results were compared well with experimental results in the range of investigation up to 1000 Hz.

Ganguli (2001) used a fuzzy logic system to locate damage on helicopter rotor blades. A fuzzy logic system can be expressed as a linear combination of fuzzy basis function and is a universal function approximator (Ganguli, 2001). The purpose of this study was to determine the approximate location of the damage and then allow for other more intrusive techniques to pinpoint the damage location.

3.1.1 Damage Detection through Changes in Natural Frequencies

Salawu (1997) has presented an excellent review of various investigations on the effects of structural damage on natural frequencies. Many damage location methods use changes in resonant frequencies because frequency measurements can be quickly conducted and are often reliable. However changes in ambient conditions such as temperature can cause significant frequency changes in composite materials, and findings

45

suggest that detection of damage using frequency measurements might be unreliable when the damage is located at regions of low stress (Salawu, 1997). Similar results were presented by Kessler et al. (2002) where the frequency response method was found to be reliable for detecting damage in simple composite structures, but information about damage type, size, location and orientation could not be obtained. Another investigation by Zak et al. (2000) showed good agreement between experimental and numerical calculations of the first three bending natural frequencies of a delaminated composite beam. Kuo and Jayasuriya (2002) used transfer functions to determine the extent of joint loosening in automobile vehicle frames with high mileage. The method was successful as presented in the paper, but did not give specifics for frequency ranges investigated and what type of frequency response functions were utilized.

3.1.2 Impedance Based Methods

Impedance-based structural health monitoring techniques show much promise, but require some rather expensive hardware. The impedance-based technique utilizes the direct and converse electromechanical properties of piezoelectric materials, which allows for simultaneous actuation and sensing. The fundamental principle is to track the high frequency (typically > 30 kHz) electrical point impedance of a piezoelectric material bonded onto a structure (Park, 2000). A change in the structural mechanical impedance is caused by physical changes in the structure, which induces a change in the electrical impedance of the piezoelectric material because of the electromechanical coupling between the piezoelectric material and the structures. Thus, structural damage can be identified by monitoring the changes in electrical impedance of the piezoelectric material. This technique is very sensitive at high frequencies because the wavelength of the

excitation is small enough to detect incipient-type damage like slight delaminations or loose joints (Kabeya, 1998). Some problems associated with the electrical impedance methods are that the material properties of both the piezoelectric material and composite structures are temperature dependant, so temperature variation can be interpreted as damage. A frequency range of 70kHz to 80kHz was used by Kabeya (1998). Since the excitation frequencies are very high, the piezoelectric sensors are limited in their sensing areas and a large number of piezoelectric sensors and actuators are required to adequately cover the structure. Moreover, since this technique only uses point measurements of the electrical impedance of sensors and does not use mutual information between them, the ability to identify damage location is poor. One major benefit of the impedance method is that it does not based on a theoretical model as were most other techniques presented earlier, and thus can be applied to complex structures. The application of impedance based monitoring techniques was presented by Berman et al. (1999) for the fiber reinforcement of masonry structures.

3.1.3 Transmittance Functions

Transmittance functions (TF) are derived as the complex ratio between Fourier transforms of a response point and a reference point on a structure. The motivation for using the TF is that excitation does not need to be measured since changes in the structure due to the environmental effects (temperature and moisture) are partly cancelled. Also, the cross-spectral density used in TF is a measure of the linearity between two response points on the structure and can detect local damage by propagation changes (phase delay and amplitude modulation) in the structural response. Since the cross-spectral density function is the Fourier transform of the cross-correlation function, it represents the

frequency domain characterization of the similarity of the magnitude and phase of two signals, e.g. of two nearby response points on the structure. Hence, if used in the correct frequency range, it can accurately detect damage over small distances on a structure. Furthermore, measured transmittance data inherit certain advantages over modal data. Firstly, transmittance functions have little sources for computing error, except the minimal error from the numerical Fast Fourier Transform. Secondly, they carry complete information on the dynamic behavior of the test structure in terms of both the vibration modes and the damping at many frequency points, including away from the responses of the structure (Zhang et al., 1999).

The transmittance function does not depend on whether the receptance, mobility or inertance spectral densities are measured since it is a ratio of the frequency response functions. Therefore, different sensor types can be used to measure the vibration response. When damage occurs, the peaks and valleys of the transmittance function misalign. This misalignment caused by a change between the healthy and damaged system can be quantified. Generally, the sensitivity of the technique to detect small damage increases as the actuator and sensor move close to the damage, and as the frequency of excitation increases (Schultz et al., 1999). The damage values for some cases are nearly four times larger at high frequencies (10-20 kHz) than at low frequencies (200-1800 Hz) (Zhang et al., 1999). However, the size of the PZT sensors plays a role in the effective frequency range that the sensor can detect damage. Different sized sensors are more tuned for certain vibration frequencies. A larger sensor would not be as effective as a small sensor for detecting high frequency vibration, because the sensor would be much larger than the vibration wavelengths. Also, at the higher frequencies

there are additional hardware concerns because of a higher sampling, more FFT lines, and sensors must be spaced closer as their range decreases due to the shorter wavelengths.

Advantages of transmittance functions as stated by Schulz et al. (1997) are:

1. No structural model is needed.

2. Excitation does not need to be measured.

3. The non-resonant and anti-resonant (zeros) parts of the transmittance functions are very sensitive and can detect small damage (cracks) that other methods miss.

4. Simultaneous multiple damages can be detected.

5. Well developed sensor and signal processing techniques are used rather than unproven impedance methods.

6. Transmittance functions are highly repeatable diagnostic procedures, because environmentally induced changes in the physical properties of the structure are mostly cancelled by the ratio of response quantities in the transmittance functions.

7. Transmittance functions have a high dynamic range and can decompose the response signal/noise into different frequency bands to focus on abrupt spectral changes due to damage.

8. Measurement noise tends to be canceled by the normalization in the transmittance function.

9. The transmittance function technique is algorithmically simple and suitable for autonomous damage detect.

Of course, more tests on other types of structures and damages need to be performed to confirm these characteristics of this method. Successful transmittance function testing

for wind turbine blade damage analysis was presented by Ghoshal et al. (2000) and by Schultz et al. (1999) for beams and plates.

3.2 Theory of Transfer and Transmittance Functions

3.2.1 Transfer Functions

Transfer functions characterize the dynamic properties of a system. Transfer functions are measured dynamically by initiating a system response with some type of forcing function, and measuring the resulting system output. In vibration measurements the output that can be measured are displacement, velocity, or acceleration. A transfer function of a system is a measure of the system's response to a given input excitation. The equation of motion of a single degree-of-freedom system consisting of a spring, mass and damper subjected to an excitation force is

$$m\frac{d^2x}{dt^2} + c\frac{dx}{dt} + kx = F(t) \qquad \qquad \textbf{(39)}$$

The Laplace transform of the system's equation of motion equation (39) for system under forced excitation is the transfer function H. The Laplace transform converts equation (39) from the time domain to the frequency domain. The corresponding Laplace transform of the equation of motion is given in equation (40).

$$H(j\omega) = \frac{X(j\omega)}{F(j\omega)} = \frac{1}{m(j\omega)^2 + c(j\omega) + k} \qquad \qquad \textbf{(40)}$$

Transfer functions are excellent tools for determining a system's natural frequencies. When the driving frequency equals the undamped natural frequency, the system's response peaks because of the following condition $k - m\omega^2 = 0$. This allows the natural frequencies to be determined from a plot of the transfer function magnitude versus forcing frequency. For higher-order systems with multiple natural frequencies, the resonant frequencies correspond to the plots peaks, as can be seen by the representative

transfer function in Figure 3-1, and the first three peaks correspond to frequencies of 1050 Hz, 1650 Hz, and 2400 Hz, respectively.
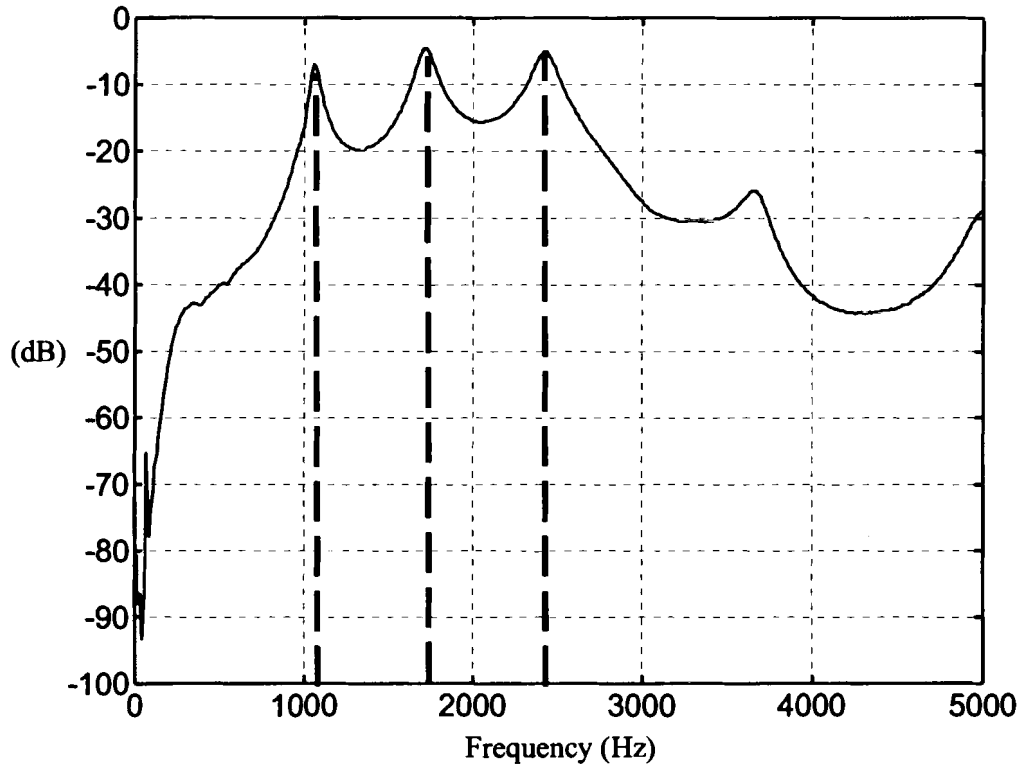
Figure 3-1 Representative Transfer Function

Experimental measurement of the transfer function of continuous systems is not as simple as taking the Laplace transform of the equation of motion as illustrated earlier. The mass, stiffness, and damping matrices can be estimated, but not calculated exactly for most real continuous systems. Thus, the responses measured by the transducers are discretized in order to take advantage of computers computational power. Discretization of the data, and noise in the systems prohibits the data to be analyzed in a deterministic fashion as shown earlier. Presented subsequently is the method used to estimate the transfer function of a system.

For a discrete signal, the position, velocity, or acceleration relative to time can be measured. A measure of how fast that signal is changing is the autocorrelation given by Equation (41). Likewise a measure of how one signal $x(t)$ is changing relative to another signal $f(t)$ is the cross-correlation of the signals given by equation (42). Here $x(t)$ is the response of the system, and $f(t)$ is the forcing function.

$$R_{xx} = \frac{\lim}{T \to \infty} \frac{1}{T} \int_0^T x(t)x(t+\tau)dt \qquad (41)$$

$$R_{xf} = \frac{\lim}{T \to \infty} \frac{1}{T} \int_0^T x(t)f(t+\tau)dt \qquad (42)$$

The autocorrelation and cross-correlation is then converted to the frequency domain by employing the discrete Fourier transform. The spectral density is the discrete Fourier transform of the autocorrelation, and likewise the cross-spectral density is the discrete Fourier transform of the cross-correlation. Equations (43) and (44) are the spectral density and cross-spectral density respectively.

$$S_{xx}(\omega) = \frac{1}{2\pi} \int_{-\infty}^{\infty} R_{xx}(\tau)e^{-j\omega\tau}d\tau \qquad (43)$$

$$S_{xf}(\omega) = \frac{1}{2\pi} \int_{-\infty}^{\infty} R_{xf}(\tau)e^{-j\omega\tau}d\tau \qquad (44)$$

The spectral and cross-spectral densities can be used to compute the transfer function of a system as shown by the spectral densities relationship equations (45) and (46) given below. A development of equations (45) and (46) is described by Inman (2000). The signal processing hardware used to estimate the transfer functions employs these equations in it's estimation of the transfer function. $S_{xx}(\omega)$ is the spectral density of the response, and $S_{xf}(\omega)$ is the cross-spectral density of the response with respect to the

52

forcing function $f(t)$. Likewise $S_{fx}(\omega)$ is the cross-spectral density of the forcing function with respect to the response $x(t)$, and $S_{ff}(\omega)$ is the spectral density of the forcing function.

$$S_{xx}(\omega) = H(j\omega)S_{xf}(\omega) \tag{45}$$

$$S_{fx}(\omega) = H(j\omega)S_{ff}(\omega) \tag{46}$$

The coherence function is used as a measure of the quality of data gathered using the spectral densities. The coherence function can only range from zero to one, with one meaning that the transfer functions obtain by equations (45) and (46) are equal. If the coherence equals zero then the two transfer functions are uncorrelated different, and the signal is pure noise.

$$\gamma^2 = \frac{\left|S_{xf}(\omega)\right|^2}{S_{xx}(\omega)S_{ff}(\omega)} \tag{47}$$

The transfer functions found in the following experiments were estimated using discretized signals using the methodology presented here.

3.2.2 Transmittance Functions

Transmittance functions (TF) characterize the response at two different points of a system for a given input. Transmittance functions are a ratio of the response cross-spectral density between two sensors, and the response auto-spectral density at a point, and it is a non-dimensional complex quantity that defines how vibration is transmitted between two locations as function of frequency. Displacement, velocity, or acceleration measurements can be used to compute the transmittance function. The transmittance functions are found similarly to the transfer functions discussed in section 3.2.1. But instead of computing the spectral densities of the forcing function, the spectral density and cross-spectral density are calculated for two separate sensors on a system excited by

the same input. The transmittance function of sensor A with respect to sensor B is defined as

$$T_{ab}(\omega) = \frac{S_{ab}(\omega)}{S_{bb}(\omega)}$$ (48)

whereas the transmittance function of sensor B with respect to sensor A is defined by

$$T_{ba}(\omega) = \frac{S_{ba}(\omega)}{S_{aa}(\omega)}$$ (49)

The forcing function does not need to be measured, as long as the measurements at the two different sensors are taken simultaneously to calculate the spectral and cross-spectral densities. The transmittance function estimation is mathematically the same as transfer functions estimation, with the difference being transfer functions are measures of a response to an input, while transmittance functions are measures of response to another response.

3.3 Experimental Setup

The platform for the various health-monitoring schemes investigated here was a bolted composite plate. The configuration investigated is a 24.5-inch square fiberglass plate bolted to a steel frame with 16 ½-inch diameter grade eight bolts. In this section the experimental setup is described in detail.

3.3.1 Fiberglass Plate Configuration

The fiberglass plate used in the following experiments was cut from a larger panel fabricated by Keith Berube and staff at the University of Maine using Vacuum Assisted Resin Transfer Moulding (VARTM). Panel number 35 from which the smaller 24.5 inch square plate was cut was 48 by 30 inches, and ¼ inch thick. Four symmetric layers of fiber glass in the 0/90 configuration made up the plate to be ¼ inch thick with Dow Derakane 8084 resin used as matrix. Sixteen 9/16 inch holes were drilled around the

plate so that it could be clamped to the steel base. A 9/16 inch diamond tipped drill bit

supplied by Accurate Diamond Tool Corporation of Emerson, New Jersey, was used to

drill the holes. The bolt pattern used for the fiberglass plate matches with the bolt pattern

shown in Figure 3-2 for the steel frame.
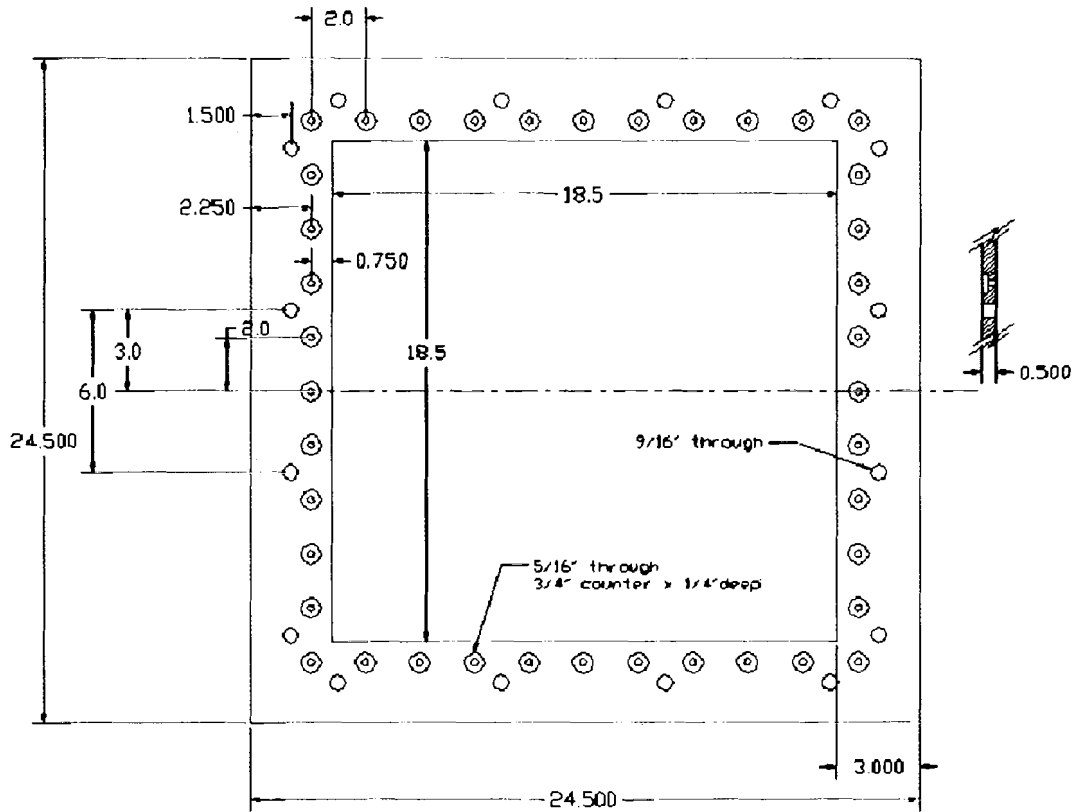
Figure 3-2 Steel Frame Schematic with Dimensions in Inches

Figure 3-2 above depicts the steel frame that was fabricated by Alexander's Welding

and Machine of Greenfield, Maine. The larger 9/16 inch holes are for the ½ inch grade

eight bolts that attached the fiber-glass plate to the frame. The smaller counter sunk holes

are for the ¼ inch bolts to attach the frame to the worktable. The table used has a ¼

diameter bolt pattern spaced two inches on center. Wooden blocks were used to support

the plate above the table to facilitate access to the bottom of the frame for tightening and loosening the ½ bolts.

All of the grade eight bolts used to fasten the plate were supplied by A.L. Design Inc. of Buffalo, New York. The bolts were ½ inch diameter by 2 inches long with 1.5 inches of thread. For the experiments discussed in this chapter, one of the bolts was internally gauged with strain gauges. This instrumented load sensing bolt model ALD-BOLT-1/2-2 serial number 220807 was the same as the other bolts, except for the internal strain gauges. The strain gauge was excited by 10 V DC in full bridge configuration and the output read in mV is correlated to the bolt load.

The complete calibration sheet for ALD-BOLT-1/2-2 serial #: 22087 can be found in Appendix A. Figure 3-3 below shows an instrumented bolt configuration. The fiber-glass plate is on top of the steel frame with wooden blocks supporting the frame above the table.
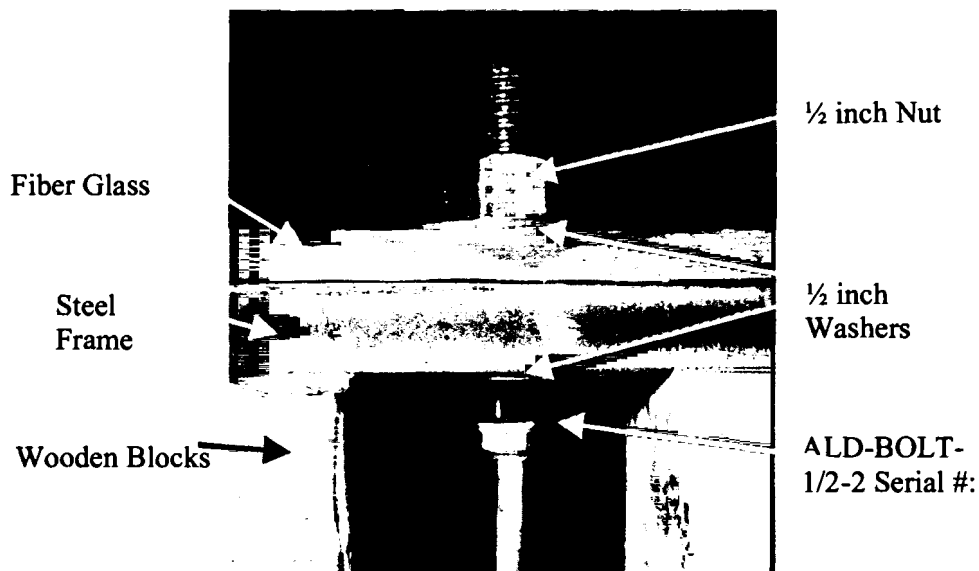
Figure 3-3 Instrumented Bolt Configuration

3.3.2 Dynamic Sensors and Actuators

A piezoelectric actuator (ACX QP 10W) was bonded to the center of the plate by applying epoxy between the actuator and plate and vacuum bagging it for three or four hours. Complete specifications of the ACX piezoelectric actuator are given in Appendix C. ACX actuators were chosen because of their slim low profile design, and they came with the wire leads already attached to the piezoelectric wafers. Early in the investigation soldering wire leads to piezoelectric wafers was experimented with, but this proved to be cumbersome. Figure 3-4 below shows the setup with the actuator bonded at the center of the plate, and sensors for the high frequency tests located near two of the bolts.
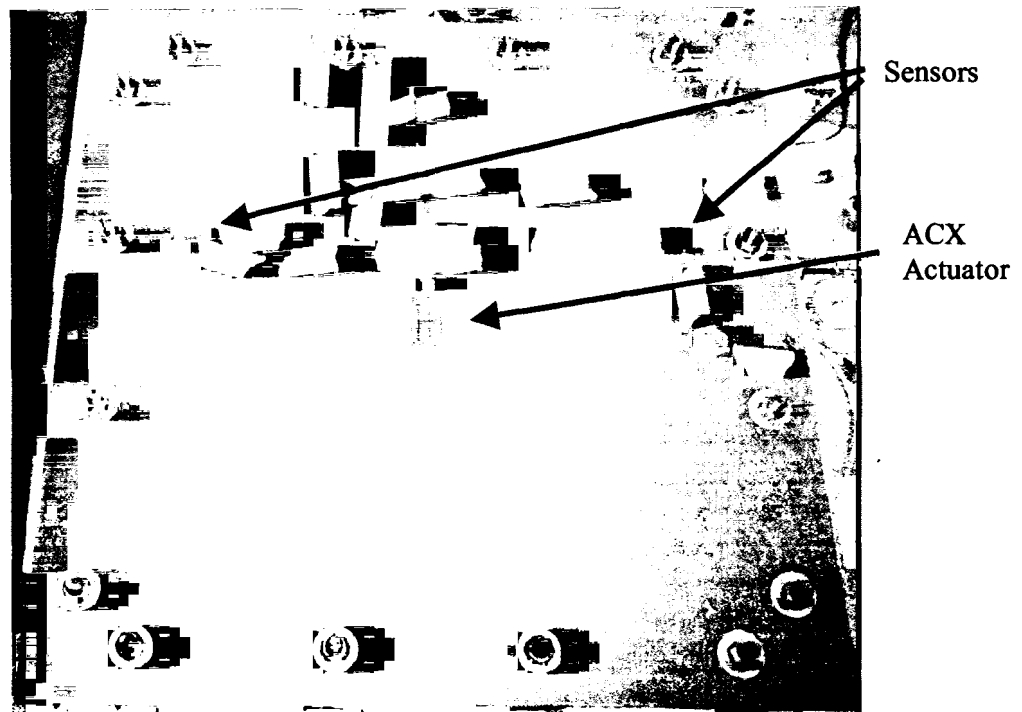
Figure 3-4 Sensors and Actuators Mounted on the Plate

Accelerometers and dynamic strain sensors were used to measure the response of the plate to an excitation. The accelerometer senses the accelerations transverse to the plane

of the plate, while the strain sensor measures the in-plane dynamic strain induced in the plate from the vibration. Both sensors were supplied by PCB Piezotronics of Depew, New York. Model 352B10 ceramic shear ICP accelerometers were chosen for being able to measure low amplitude vibration, having minimal mass, and being able to operate in a frequency range of up to 25 kHz. ICP is a trademark of PCB, and sensors with this designation have internal signal conditioning circuitry that minimizes noise and improves sensor accuracy. Complete specifications for model 352B10 accelerometers are given in Appendix D. The dynamic strain sensor model 740B02 was chosen for it's low profile, and because it is less expensive than accelerometers. Because of cost considerations strain sensors are attractive for large scale health monitoring schemes. The accelerometer and dynamic strain sensor used in these experiments are depicted below in Figure 3-5. Complete dynamic strain sensor specifications can be found in Appendix D. For the lower frequency dynamic measurements 352A24 model PCB accelerometer was used. This accelerometer was used for the early experiments to determine the fundamental frequency before the higher frequency accelerometers were purchased. The reader is referred to Appendix D for specifications.
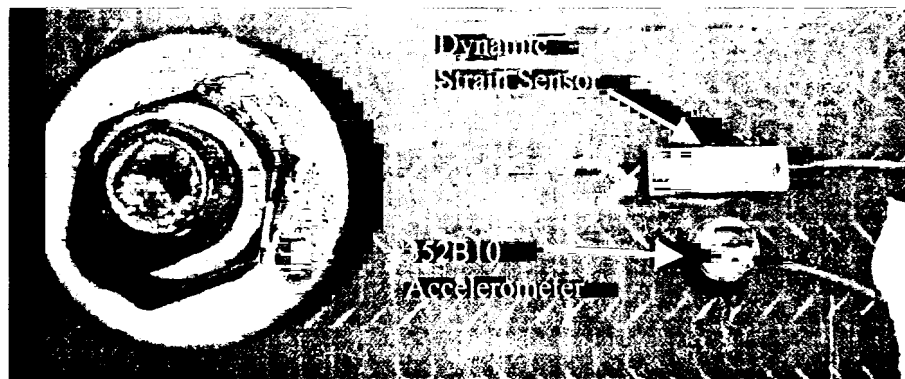
Figure 3-5 Dynamic Strain Sensor and Accelerometer

3.3.3 Electronics

Various electronic components were employed to complete the experimental setup. Voltage sources and measurement devices were used with the sensors, and a sophisticated data acquisition system completed the setup.

The instrumented bolts were excited per specifications by a Hewlett Packard 3245A Universal Source serial #: 2831A02484 set to 10 volts DC, and a Micronta Auto-Range Digital Mulitmeter Serial #: 22-195S was used to read the output voltage. The ACX actuator's excitation signal was generated by Siglab and amplified by a PCB 790A01 signal conditioner serial number 274 with a set gain of 25. PCB accelerometers and dynamic strain sensors signals were conditioned by a 482A20 PCB ICP sensor signal conditioner. The signal conditioner was set to unity gain for the accelerometers. However, the strain sensor's lower output required a gain of ten for the lower frequency ranges, at frequencies over one kHz the stain sensors required a unity gain. The excitation signal was generated using a SigLab dynamic signal acquisition and processing hardware. SigLab is a dynamic signal and system analyzer that runs on a MATLAB platform with function generation, spectrum analyzer, oscilloscope, and network analyzer capabilities. The SigLab hardware has 2 input and 2 output channels and has a bandwidth of 20 kHz. SigLab is used as the function generator, data acquisition system, and data analyzer in our experiments. Hardware specifications for the PCB signal conditioner, and SigLab is presented in Appendix E and Appendix B respectively.

Figure 3-6 Siglab Hardware

3.4 Experimental Procedure

The experimental procedures followed in conducting the various studies are described

in detail in this section.

3.4.1 Bolt Torque Repeatability

Bolt torque repeatability experiments were conducted to determine how reliable a

torque wrench was at applying the desired torque, thus causing consistent tensile loads in

the bolts. Although it was desirable to know the force in each of the bolts, it was

prohibitively expensive to use instrumented bolts for all 16 bolts around the perimeter of

the plate. Therefore, it would be useful to correlate the applied torque to the bolt load.

In this experiment, the torque of the instrumented bolt was varied, while the other

bolts were maintained at constant torque sufficient to prevent any plate movement. The

instrumented bolt was lubricated with Loctite antiseize and threaded through the bolt hole

with the nut on the top of the plate, as shown in Figure 3-3. The HP power source was

then connected to the appropriate leads on the instrumented bolt and set to 10 volts DC.

A Micronta multimeter was also turned on, and connected to the instrumented bolt. The

electronics were left on for a period of time not less than 20 minutes for each trial before starting the tests. This warm-up period is required to ensure accuracy of the bolts output per A. L. Design Inc. information sheet in appendix A. The bolt was then tightened to 20 foot-lbs by the 10 to 100 foot pound torque wrench (serial number 4010486831). After the voltage readout was recorded, the torque was increased by five foot-lbs to 25 foot-lbs and the voltage recorded again. The torque was increased by five foot-lbs increments and the corresponding voltage recorded until the final torque of 50 foot-lbs. Then the process was repeated five more times for a total of six ranges from 20 to 50 foot-lbs for each trial. Six trials were completed for a total of 336 measurements.

3.4.2 Variation of Fundamental Frequency with Uniform Torque for all Bolts

The purpose of the variation of fundamental frequency on uniform bolt torque study is to investigate the effects a perimeter clamping force has on the fundamental natural frequency of a plate. The 24.5 inch square fiberglass plate is clamped to the steel frame using sixteen ½" diameter grade eight bolts. The torques were applied to the bolts using two different Armstrong micrometer torque wrenches. The smaller torque wrench (serial number 960831060) had a torque range of 50 to 250 inch pounds of torque, while the larger wrench was capable of 10 to 100 foot pounds of torque (serial number 4010486831). The response of the plate was sensed by a PCB 352A24 accelerometer mounted 0.75 inches from the edge of the ACX actuator as shown in Figure 3-7.
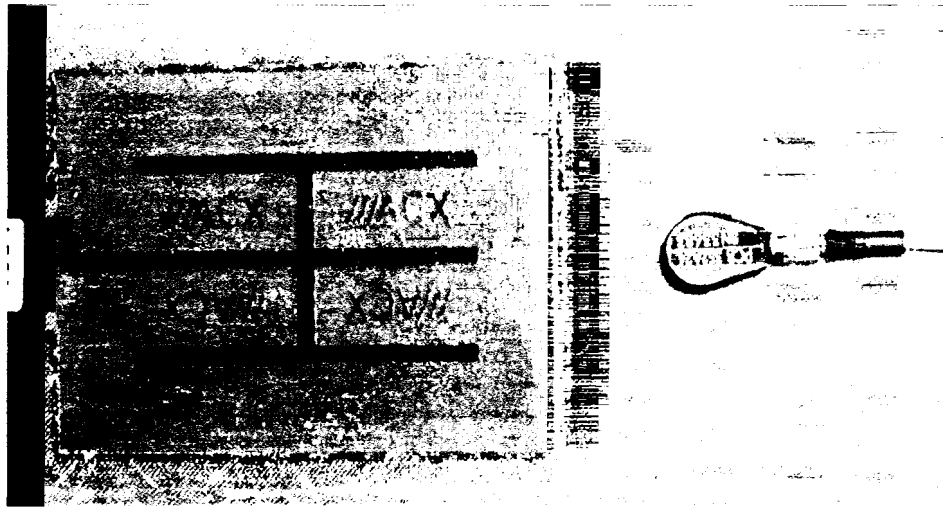
Figure 3-7 352A24 Accelerometer Placement Relative to the ACX Actuator

Fifteen regulator grade eight bolts were threaded through the plate holes with the sixteenth bolt being the instrumented bolt. All of the bolts were lubricated with Loctite nickel antiseize and nuts threaded down so that they did not quite touch the washers.

After the installation of the plate, the HP function generator and Micronta multimeter were switched on and connected to the instrumented bolt, as were the ACX actuators and PCB accelerometer connected to their respective signal conditioners. The electronics and the SigLab hardware were also turned on and allowed to warm up for a period of at least 20 minutes.

For the first trial, the bolts were left loose enough to rattle in the holes. The Siglab's dynamic signal analyzer was set to average the data from three trials consisting of 4096 data points recorded. The system excitation was a two volts root mean square (VRMS) chirp function over a frequency range of 0 to 1000 Hz. Estimation of the transfer function was performed with the network analyzer module (VNA) of the SigLab interface program. The fundamental frequency was estimated from the transfer function. Another

experiment with a narrower bandwidth of 100 Hz around the fundamental frequency was performed to accurately determine the fundamental frequency. Both transfer functions were then saved to file, and the fundamental frequency and the instrumented bolt load were recorded.

Next, the bolts were torqued to 50 inch pounds using the 50 to 250 in-lb torque wrench in the order shown in Figure 3-8. The corresponding transfer function and pertinent data were recorded. The 10 to 100 foot pound torque wrench was used for torques greater than 300 in-lb. During the lower torque trials, the torque was incremented by 10 inch pounds, whereas for higher torques, larger torque increments were used. The following torques were applied to all the bolts: 0, 50, 60, 70, 80, 90, 100, 110, 120, 130, 140, 150, 160, 170, 200, 230, 300, 480 and 720
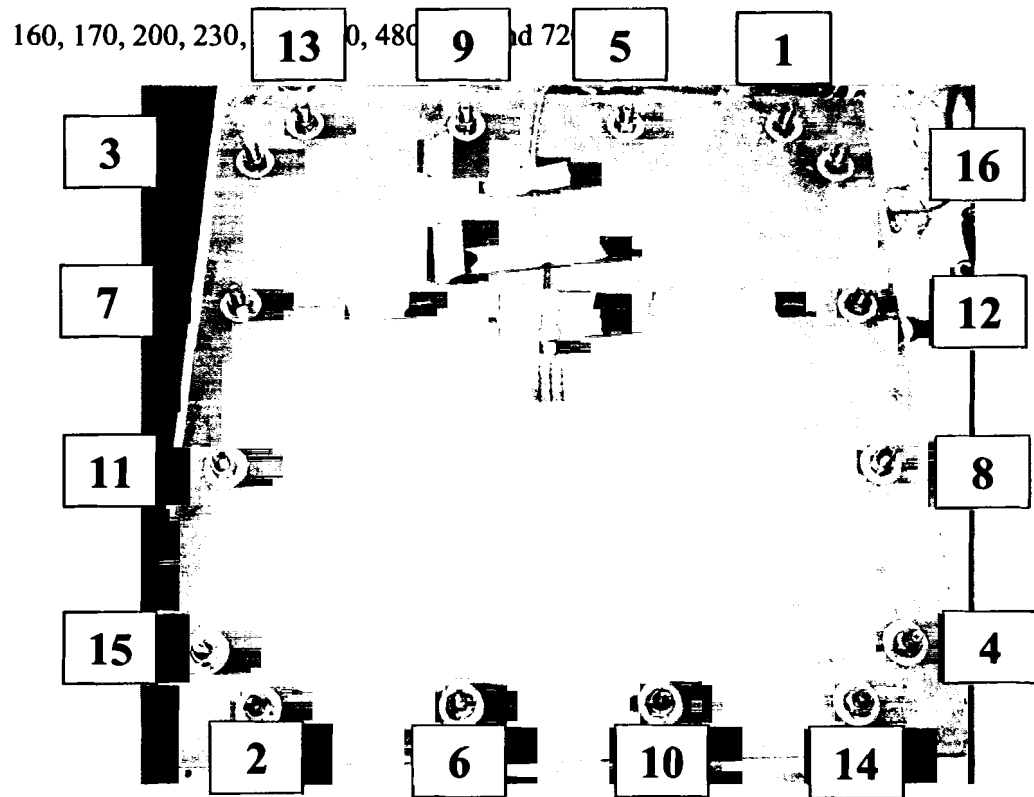
Figure 3-8 Bolt Torque Pattern

3.4.3 Fundamental Frequency Dependency on Single Bolt

In the previous section the dependency of the fundamental frequency on the perimeter clamping force was investigated. The sensitivity of the fundamental frequency on a single bolt loosening is investigated here. The bolt torque for all other bolts are unchanged in this investigation. The experimental procedure is identical to the procedure given in section 3.4.2, except that only one bolt has the torque varied as opposed to adjusting the torque of all 16 bolts as done in section 3.4.2.

For the first trial the bolts were tightened to the full torque load of 720 inch pounds. The Siglab's dynamic signal analyzer settings were adjusted as discussed in the experimental setup. The Siglab's network analyzer, was used to record the transfer function of the plate for a frequency range of 0 to 1000 Hz. The fundamental frequency was picked off the transfer function and a second transfer function was found for a narrower bandwidth of 100 Hz around the fundamental frequency. Both transfer functions outputs were then saved, and the fundamental frequency with the instrumented bolt's voltage recorded.

The instrumented bolt was loosened, and then tightened to 600 inch pounds using the 10 to 100 foot pound torque wrench. The transfer function was found again, and the corresponding data recorded. The torque was decreased from 600 inch pounds to finger tight (or 0 inch pounds) in reverse in the following steps: 600, 480, 360, 230, 200, 170, 160, 150, 140, 130, 120, 110, 100, 90, 80, 70, 60, 50 and 0 in-lbs.

3.4.4 High Frequency Responses

In the high frequency response experiments the frequency response of two sensors for a frequency range of 13 kHz to 17 kHz are found each change in torque. The torque of only one bolt is changed throughout the experiment. One sensor was placed directly next

64

to the bolt that has the torque varying and another sensor was placed directly on the other side of the plate. Both accelerometers and dynamic strain sensors were employed to determine which sensor gave better results. Figure 3-9 below shows the high frequency experimental configuration with the accelerometers and dynamic strain sensors.
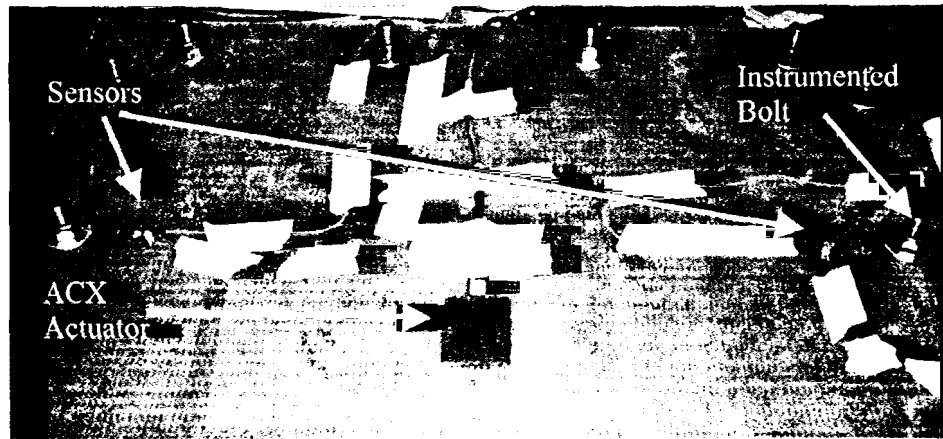
Figure 3-9 High Frequency Test Configuration

The procedure for this section is similar to the procedure given in section 3.4.3, except for the frequency range investigated, the types of sensors used, and the sensor locations. The accelerometers, and dynamic strain sensors were placed next to the instrumented bolt, and the bolt directly opposite as shown in Figure 3-9 above. Only the instrumented bolt was loosened to conduct the tests. Model 352B10 ceramic shear ICP accelerometers were the accelerometers employed for these tests as opposed to the 352A24 accelerometer that was used for the lower frequency tests. Siglab hardware generated the chirp excitation function for the ACX actuator, and measured the two separate transfer functions for a frequency range of 13 kHz to 17 kHz. The PCB ICP signal conditioner was set for a gain of one when using the accelerometers, and a gain of ten when using the dynamic strain sensors. The transfer functions for both sensor locations were saved. The

bolt torque was set and varied for the instrumented bolt in the same manner as done in section 3.4.3.

3.4.5 Transmittance Testing

Transmittance testing procedures are similar to the procedures following for the transfer function techniques. For the transmittance tests the response of two sensors are compared between each other, whereas when measuring transfer functions the response of one sensor is compared with the excitation signal. Thus, for the transmittance testing, sensor A was connected to input 1 and sensor B was connected to input 2 of the Siglab hardware. Input 2 was the reference channel for Siglab, thus the transmittance function A with respect to B (T_{AB}) was found with input channel one being A, and input channel 2 being B. Manhattan switch boxes were used switch between sensor pairs for each transmittance function to be tested. The switch boxes had four inputs and one output. All four sensors used were connected to each switch box and the corresponding signal of interest was selected by turning the dial as shown in Figure 3-10. Then the switch boxes were employed to facilitate a quick change of sensors so that multiple transmittance functions could be recorded easily. This continued until all of the desired transmittance functions were found for a given frequency range and level of damage present in the system.
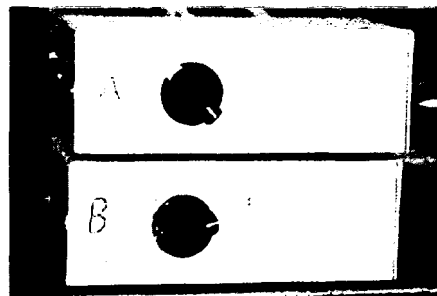
Figure 3-10 Manhattan Switch Boxes

3.4.5.1 Frequency Range Investigation.

The Siglab dynamic signal analyzer is capable of investigating systems from 0 Hz to 20 kHz, thus this is the absolute limits for the transmittance testing. A frequency bandwidth of 4 kHz was used for the testing in order to give good frequency resolution for the transmittance results. Tests were conducted for the following five frequency ranges in kHz: 0-4, 4-8, 8-12, 12-16, 16-20. An A. L. Designs instrumented bolt was loosened between sensors 2 and 3 for the damage in these series of tests as shown in Figure 3-11 below. Since the transmittance method was being explored to detect bolt loosening on a composite plate only the transmittance functions T23 and T32 were recorded in this investigation. Tests were performed per the basic procedure given earlier for all sixteen bolts tightened to 720 in-lbs by the Armstrong 10 to 100 ft-lbs torque wrench. The bolt indicated in Figure 3-11 was then loosened to 540 in-lbs and the experiment run again. Then the bolt was loosened to 300 and 60 in-lbs successively. For the 60 in-lb case the smaller 50 to 250 in-lb torque wrench was used. The actual tensile load in the bolt was recorded by measuring the output voltage for each step.
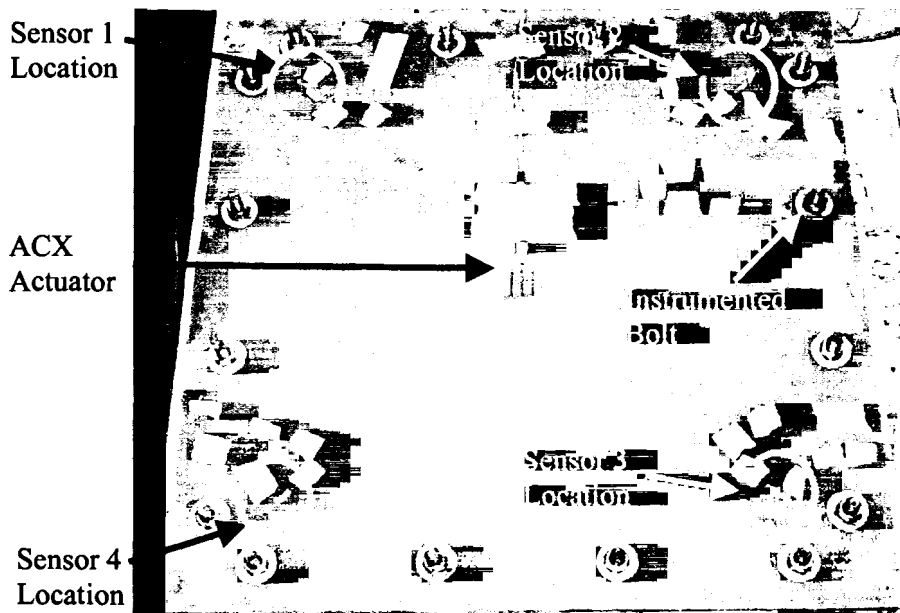
Figure 3-11 Transmittance Testing Sensor Locations

3.4.5.2 Transmittance Investigation for One Bolt Loosening. Extensive testing

was conducted using the transmittance functions for the bolt loosening done in the

frequency range survey. The two frequency ranges found to produce the best results

were used in these series of tests. The same basic transmittance function testing

procedures were followed, except tests were conducted for two different frequency

ranges simultaneously. A test was conducted for the 7 kHz to 9 kHz range, then 18 kHz

to 20 kHz range. The bolt torque for the loosened instrumented bolt was 720, 660, 600,

540, 480, 420, 360, 300, 240, 180, 120, and 60 inch pounds. The bolt torque was

adjusted using the Armstrong 10 to 100 ft-lb torque wrench, for all of the adjustments

except for the 120 and 60 settings that were done with the 50 to 250 in-lb torque wrench.

A complete set of transmittance tests were conducted for each torque setting and

frequency range. The transmittance tests were conducted between for the following

sensors pairs: 12, 21, 23, 32, 34, 43, 41, 14, 13, 31, 24, and 42. The output voltage of the

instrumented bolt was recorded for each test. The tests were conducted using both accelerometers and dynamic strain sensors.

3.4.5.3 Repeatability Procedures.

The repeatability of the transmittance test results were investigated for the results obtained by following the procedures of section 3.4.5.2. A baseline healthy set of data was recorded when all bolts were set to 720 in-lbs by the torque wrench. The remaining fifteen bolts were torqued to 720 in-lbs two days prior. The test was not immediately conducted to allow the initial composite creep to subside in an attempt to limit the effects of creep during the experiment. The transmittance functions were recorded between the following sensor pairs: 12, 21, 23, 32, 34, 43, 41, and 14. For all of the damage tests the bolt was set to 240 in-lbs. The tests were conducted approximately 5 to 10 minutes after each time the bolt was set to 240 in-lbs to allow any initial creep to subside. After the test was conducted the bolt was loosened and retightened to 240 in-lbs and the tests run again after the initial wait for the creep to subside. The start time of each test was recorded, as was the instrumented bolt voltage for each test. Ten damaged cases were run over about an hour period.

3.4.5.4 Different Bolt Procedure.

The procedure to investigate the effects of loosening a different bolt was identical to the extensive transmittance testing procedure, except only the accelerometers were used in the 7 kHz to 9 kHz range, a different bolt was loosened, and only the following torque values in inch pounds were investigated: 720, 600, 480, 360, 240, and 120. The effects of damage located elsewhere on the plate is investigated here. The bolt loosened for this experiment is on the left side of Figure 3-12.
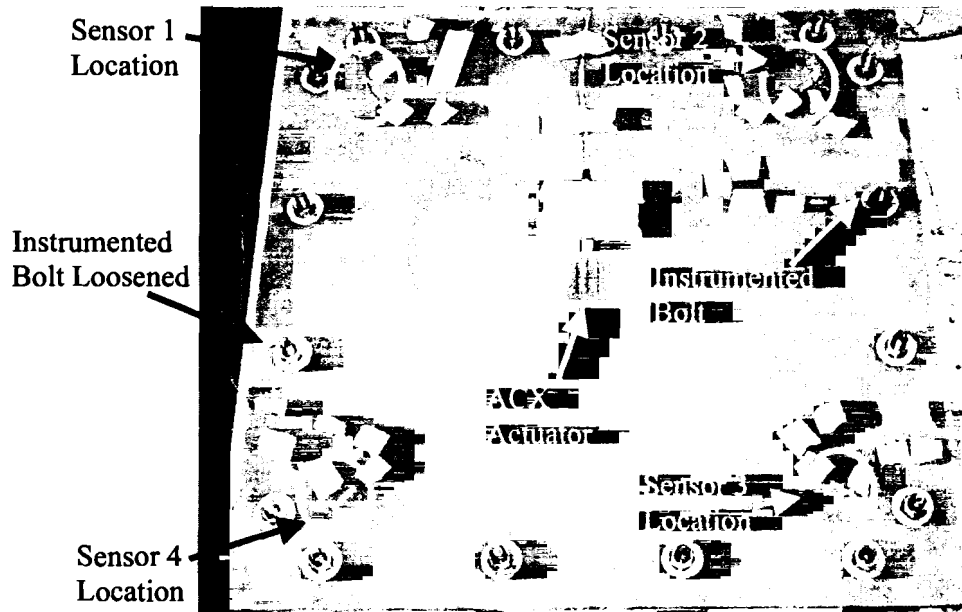
Figure 3-12 Different Damage Locations

3.5 Results and Discussion

3.5.1 Bolt Torque Repeatability

The repeatability of applying a torque with the Armstrong micrometer torque is presented in this section, and an equation for determining the bolt load from the applied torque. The calibration plot for the ALD-BOLT-1/2-2 serial number 220807 used in this study is presented in Figure 3-13. It shows the relationship of the bolt load to the voltage output, and the linear relationship is given with the equation on the plot.

70
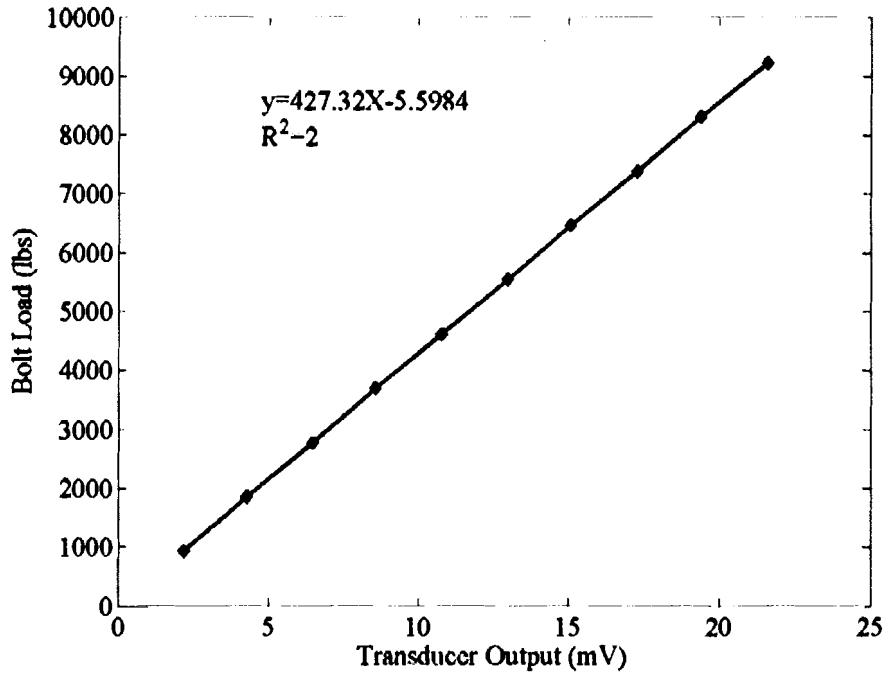
Figure 3-13 Instrumented Bolt Calibration Chart

For each of the seven trials, the output voltage was averaged for each applied torque.

Table 3-1 below reports these averages for each trial.

Table 3-1 Trial Average Output (lbs)

Applied Torque (ft-lbs)	Trials						
	1	2	3	4	5	6	7
20	3344.442	3180.778	3059.808	3216.357	3251.936	3166.546	3195.009
25	4112.952	4013.33	3892.361	3984.867	4120.068	3977.751	3999.098
30	4881.462	4888.578	4717.798	4824.535	4881.462	4717.798	4803.188
35	5585.929	5735.362	5557.466	5600.161	5678.435	5479.192	5614.393
40	6247.702	6510.988	6336.65	6382.903	6425.598	6276.165	6304.628
45	6987.748	7279.498	7144.297	7122.949	7151.413	6973.517	7073.138
50	7628.173	7927.038	7749.143	7784.722	7777.606	7706.448	7827.417

Table 3-2 below shows some statistics from the repeatability measurements. The low

values of the coefficient of variation shows that for a given torque the applied bolt load is

71

repeatable. The highest variation occurred with the torque of 20 foot-pounds with approximately 2.5 percent variation. The higher torques varied a little more than 1 percent.

Table 3-2 Repeatability Statistics

Applied Torque (ft-	Mean	Standard Deviation	Coefficient of Variation
20	3202.125	80.1462544	0.025029084
25	4014.3465	73.8939925	0.018407477
30	4816.4026	69.0354844	0.014333412
35	5607.2767	76.4508693	0.013634225
40	6354.9474	85.1020979	0.013391472
45	7104.6513	97.4826235	0.013720958
50	7771.5065	86.8538666	0.011175937

The consistency of the applied torque to the induced bolt load, is illustrated in Figure 3-14. A final equation was developed using the averages from each of the trials that gives the relationship between the applied torque and the resulting bolt load. The bolt load vs. torque equation is shown with the resulting plot in Figure 3-15.
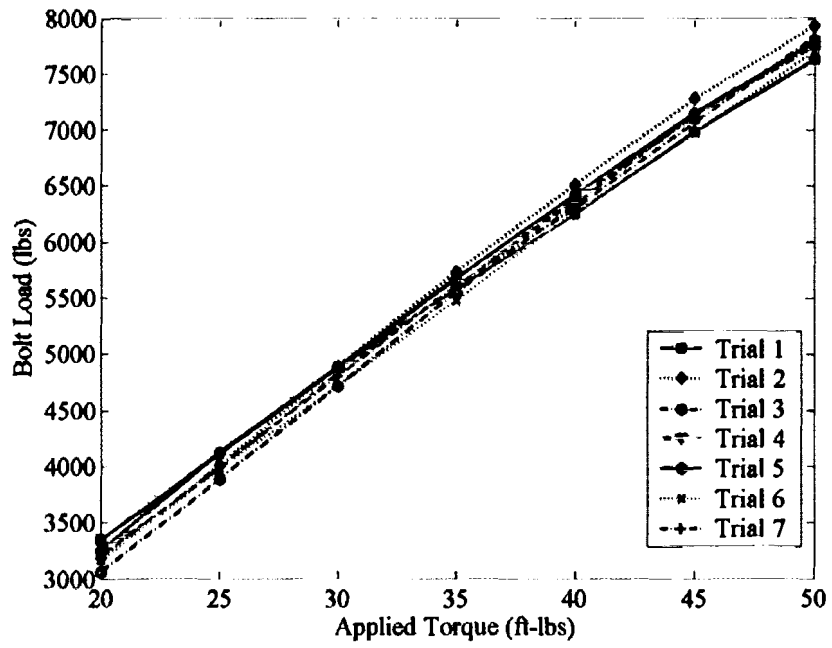
Figure 3-14 Average Results for Seven Different Trials
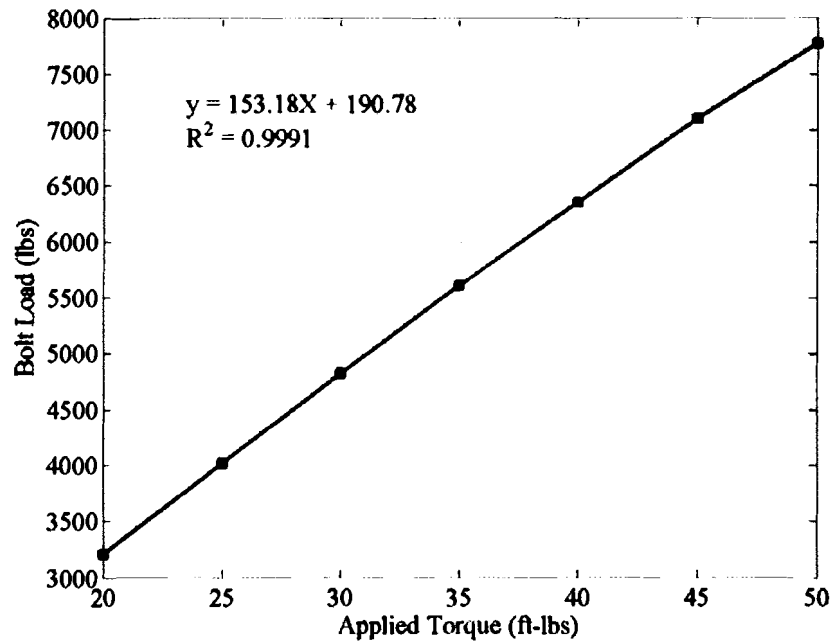
Figure 3-15 Resulting Bolt Load Correlation to Applied Torque

3.5.2 Fundamental Frequency Dependency on Uniform Clamping Force

The results of changing the bolt torque around the perimeter of the plate are presented

here. Table 3-3below reports the natural frequency and the corresponding bolt load for

each step in the applied bolt torque. The results show that a change in the tension of the

bolts around the perimeter of the plate does not significantly change the fundamental

frequency of the plate. The results are illustrated in Fig. 2-12. As can be seen in Fig. 2-

12 the fundamental frequency does not show a dependency on the uniform clamping

force around the perimeter.

Table 3-3 Uniform Clamping Force Test Results

Applied Torque (in-lbs)	1st Nat Freq (Hz)	Bolt Voltage (mV)	Bolt Tension (lbs)
0	30.25	0.00	0.00
50	135.94	0.80	336.26
60	137.25	1.00	421.72
70	137.31	1.10	464.45
80	137.56	1.30	549.92
90	137.88	1.50	635.38
100	138.13	1.70	720.85
110	138.25	1.90	806.31
120	138.50	2.20	934.51
130	138.50	2.50	1062.70
140	138.81	2.70	1148.17
150	138.81	3.00	1276.36
160	139.06	3.20	1361.83
170	139.06	3.50	1490.02
200	139.38	4.20	1789.15
230	139.38	5.20	2216.47
300	139.63	7.40	3156.57
360	139.75	8.90	3797.55
480	139.81	11.60	4951.31
600	139.81	14.80	6318.74
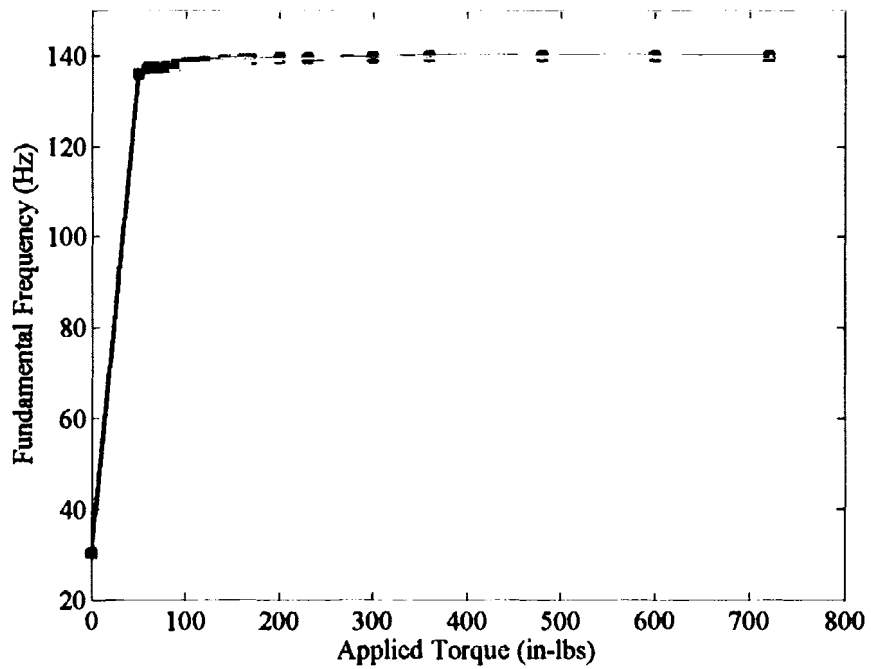
Figure 3-16 Fundamental Frequency Dependency on Uniform Perimeter Torque

3.5.3 Fundamental Frequency Dependency on Single Bolt

The fundamental frequency showed little dependency on the uniform perimeter torque

in section 3.4.3. Figure 3-17 shows the fundamental frequency when all sixteen of the

bolts are torque to 720 inch pounds of torque, and only one bolt is loosened in successive

steps. The results are similar as in section 3.4.3, where there is no significant effect of

the bolt torque on the fundamental frequency.
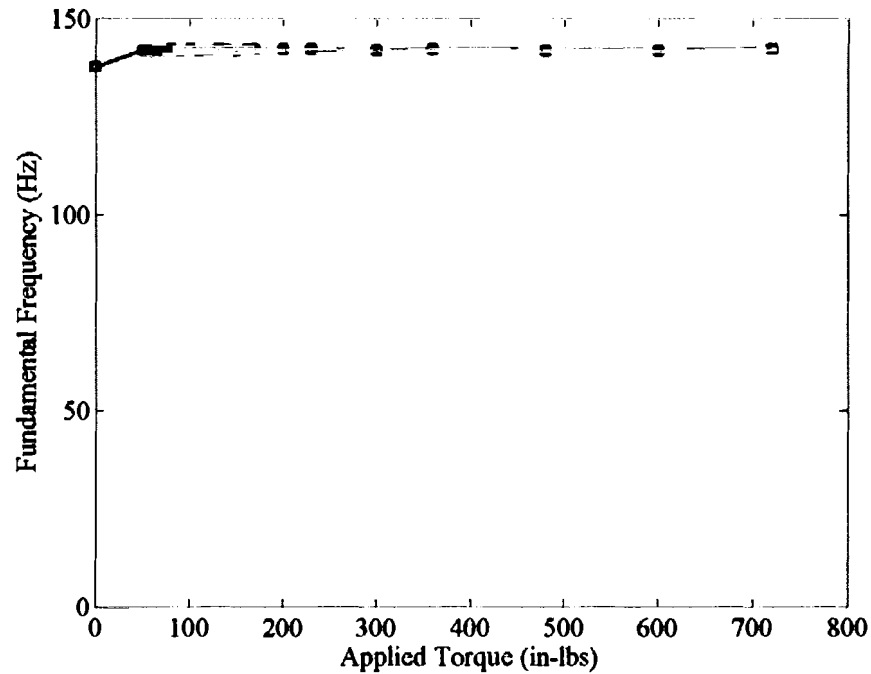
Figure 3-17 Fundamental Frequency Dependency With Single Bolt Loosening

The effects on the fundamental natural frequency when only one bolt is loosened are similar to the results in section 3.4.2. Figure 2-13 shows the calculated natural frequency for each torque setting for the instrumented bolt. There is almost no change in the fundamental frequency due to the effects of one bolt being loosened as shown in Figure 3-17 with the slope of the line close to zero after the initial torque is applied

The effect of bolt torque on the damping coefficient for the fundamental frequency was also investigated. The damping coefficients were computed using the half-power bandwidth method. In this method, there are two points corresponding to half power points (3-dB smaller than the peak response). The damping coefficient is computed using the following equation,

$$\varsigma = \frac{\omega_b - \omega_a}{2\omega_d},\qquad\qquad (50)$$

where ω_a and ω_b are the half-power frequencies and ω_d is the frequency corresponding to the maximum response.

Figure 3-18 is a representative plot of the transfer function in the dB scale about the fundamental frequency from these tests. Figure 3-19 depicts the transfer function in a narrow region about the fundamental frequency and the half-power frequencies used in calculating the damping coefficient. The Matlab program written to compute the damping coefficient from the transfer function data is available in appendix F. Figure 3-20 is a plot of the damping coefficients as a function of applied bolt torque to the bolt that was loosened. The figure shows that there is no significant change in the level of damping when the torque on one of the sixteen bolts is altered.
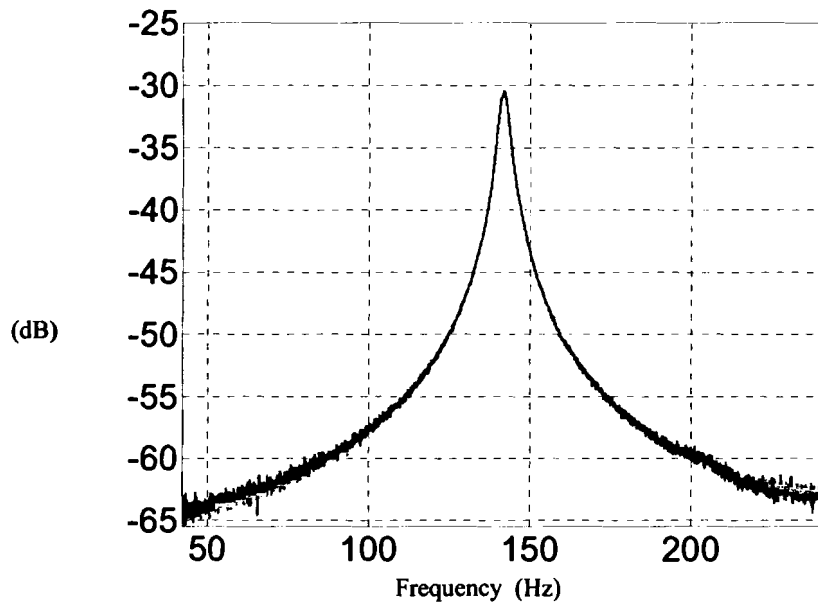

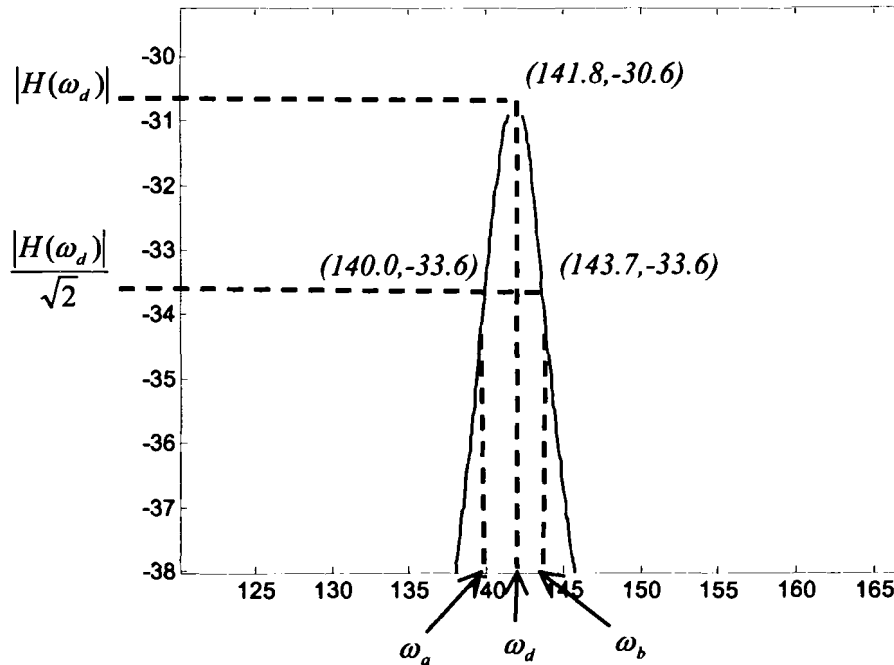Figure 3-18 Frequency Response About the Fundamental Frequency

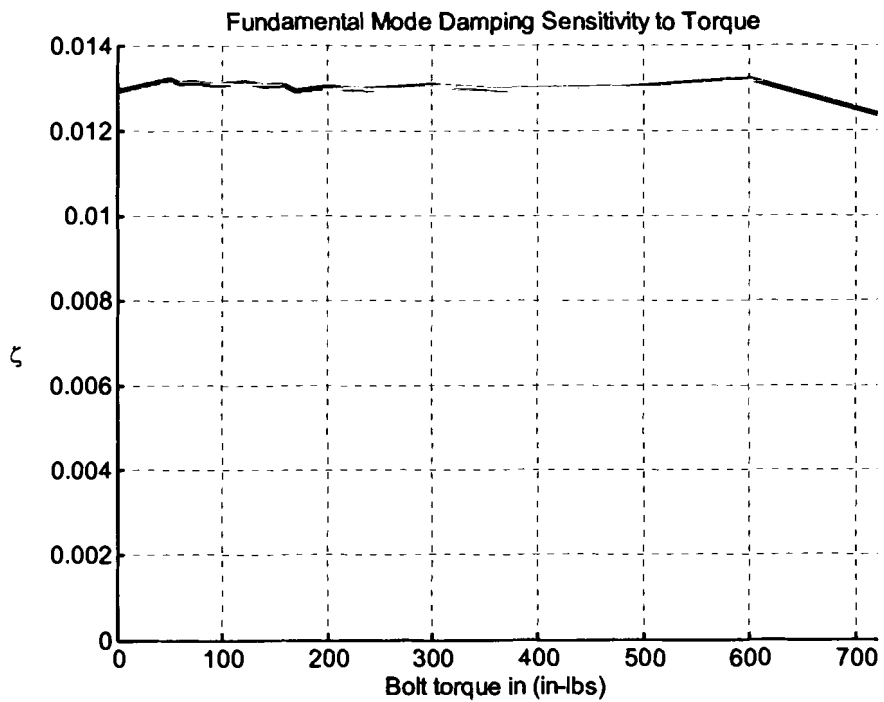Figure 3-19 Damping Estimation Illustration

Figure 3-20 Fundamental Mode Damping Sensitivity to Torque

3.5.4 High Frequency Response

The high frequency tests were conducted using both the dynamic strain sensors and the shear accelerometers. Tests 1 and 2 were conducted with the dynamic strain sensors, while test number 3 was conducted with the shear accelerometers. Two tests were conducted using the dynamic sensors to see the differences in the results between tests conducted on different days. The differences were not quantified, but rather by inspecting the differences in the plots generated from these two tests. Figures 3-21, 3-22, and 3-23 shows the recorded transfer functions of tests 1, 2 and 3 respectively for the sensors next to the loosened bolt. Figures 3-24, 3-25, and 3-26 show the recorded transfer functions for tests 1, 2, and 3 respectively for the sensors away from the loosened bolt. The plots show the response measured on the decibel scale as a function of both the loosened bolt load and frequency range investigated. The figures show that the transfer functions change as the bolt load is reduced. The change of the transfer functions as the load is changed is quantified with the damage index (D):

$$D = \frac{\int_{f_1}^{f_2} |T_h - T_d| df}{\int_{f_1}^{f_2} |T_h| df} \tag{51}$$

The frequency range used to calculate the damage index is denoted by f_1 and f_2. T_h is the reference healthy transfer function when all of the bolts are torqued to the same value. T_d represents the transfer functions for the damaged system, which in this case is due to a loose bolt. Plots of the damage index for test one, two, and three are shown in Figures 3-27, 3-28, and 3-29 respectively. Inspection of the damage index plots show an increasing change in the integral as the bolt is loosened.

The damage index plots do not show significant dependence on the location of the sensors relative to the loosened bolt. The transfer function plots change as the bolt load

80

varies, and thus the damage index plots change. The results do show that there is a change in the dynamic characteristics of the system with a bolt loosening, and that the sensitivity to the changes are different depending on what type of sensor is used. The damage index plots for dynamic strain sensors shows that there are greater changes for the sensor away from the bolt, than the sensor next to the loosened bolt as seen in Figures Figure 3-27 and Figure 3-28. The damage index plot using the accelerometers (test three) shows a larger damage index response for the sensor located closer to the loosened bolt, and a smaller damage index response for the senor place on the opposite side of the plate in Figure 3-29.

Figure 3-21 Test 1's Transfer Functions for Sensor Next to the Bolt

Figure 3-22 Test 2's Transfer Functions for Sensor Next to the Bolt

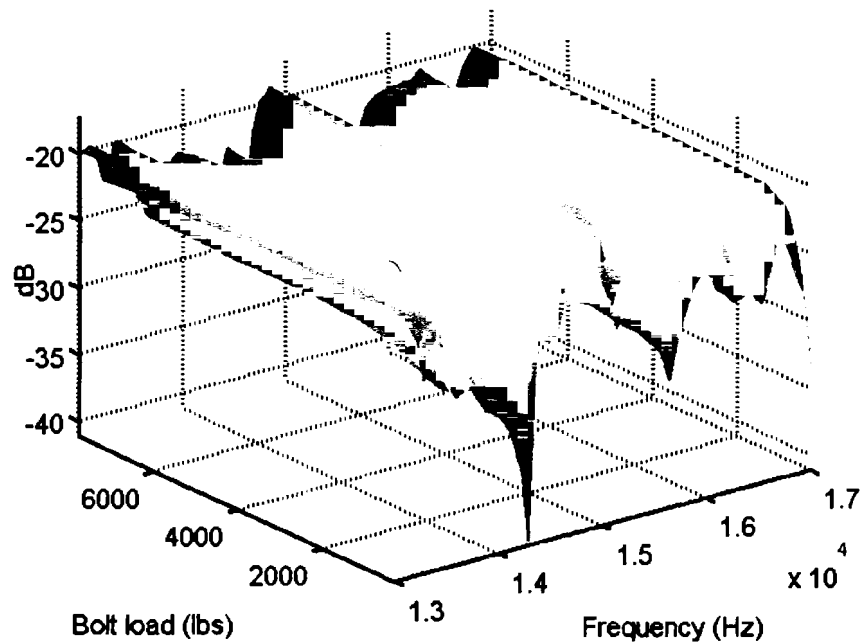Figure 3-23 Test 3's Transfer Functions for Sensor Next to the Bolt

Figure 3-24 Test 1's Transfer Functions for Sensor Away from the Bolt
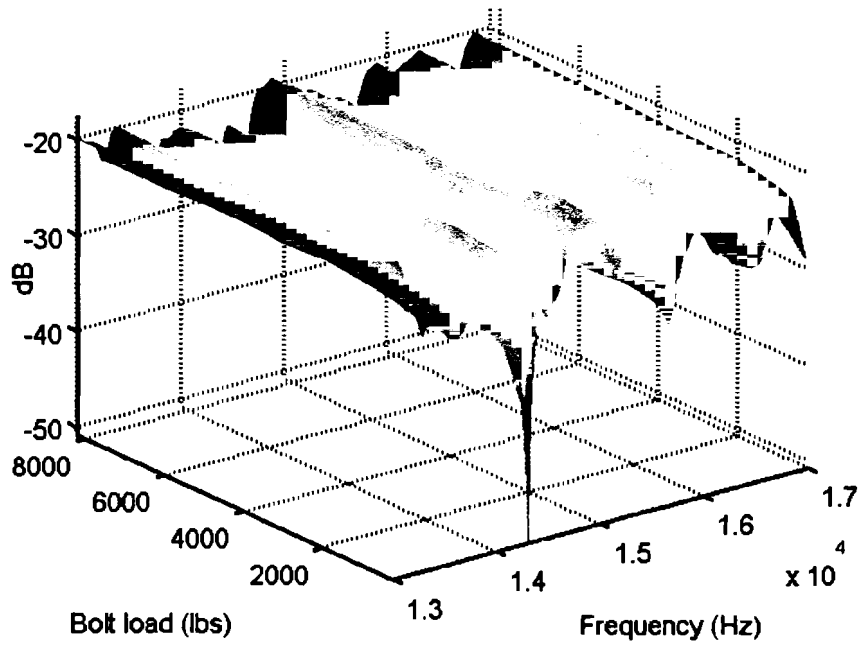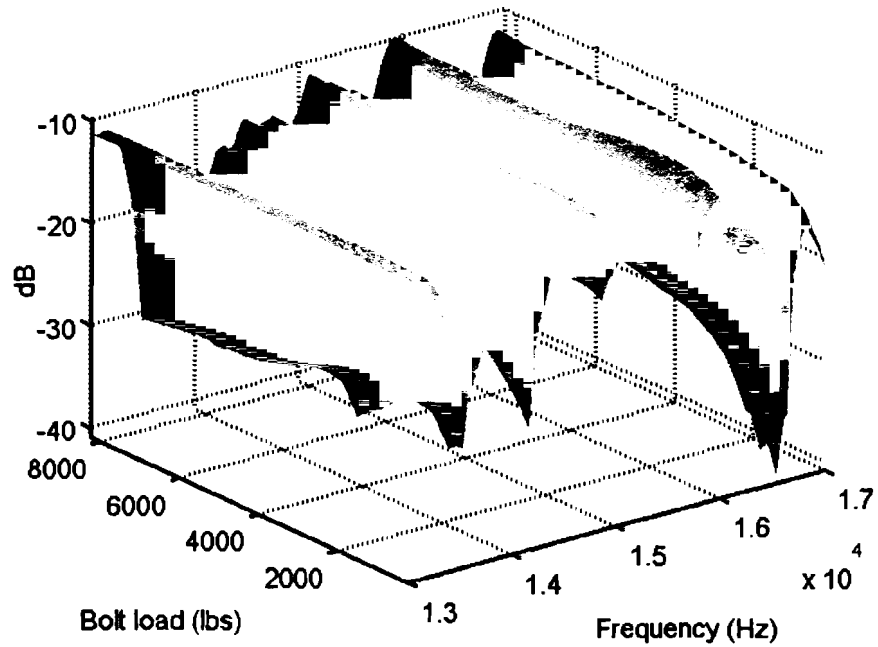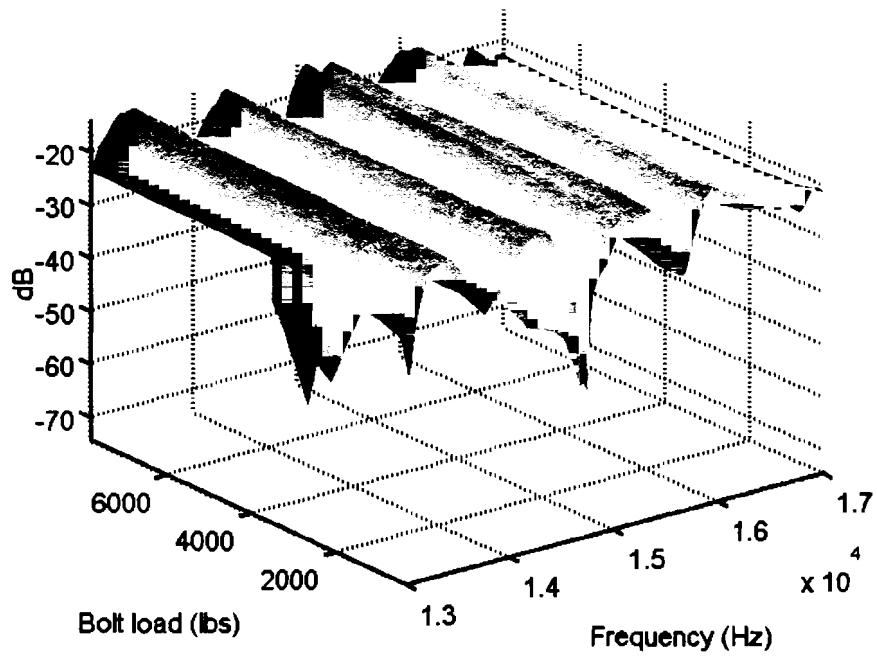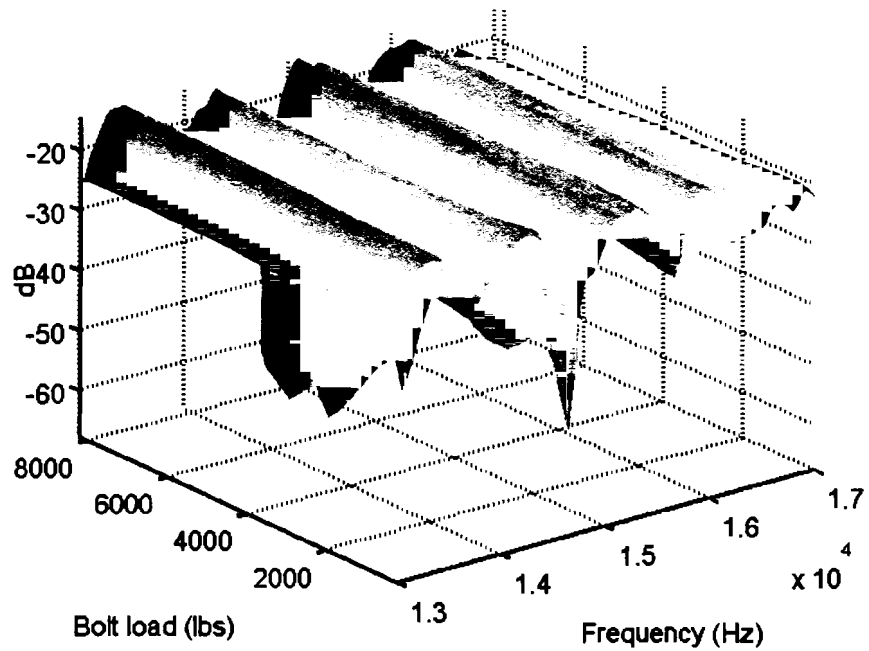

Figure 3-25 Test 2's Transfer Functions for Sensor Away from the Bolt
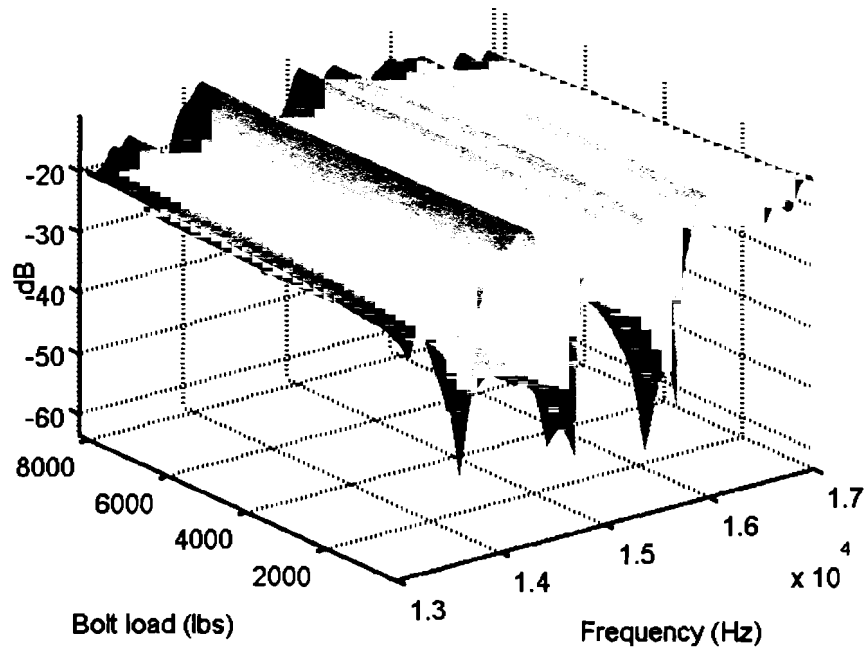
Figure 3-26 Test 3's Transfer Functions for Sensor Away From the Bolt
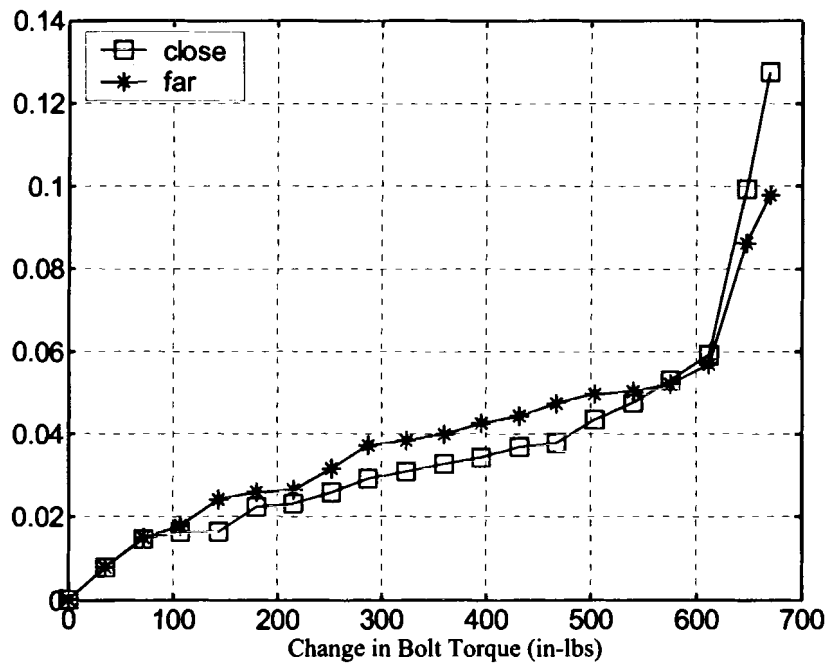
Figure 3-27 Loosening Indicator for Test 1
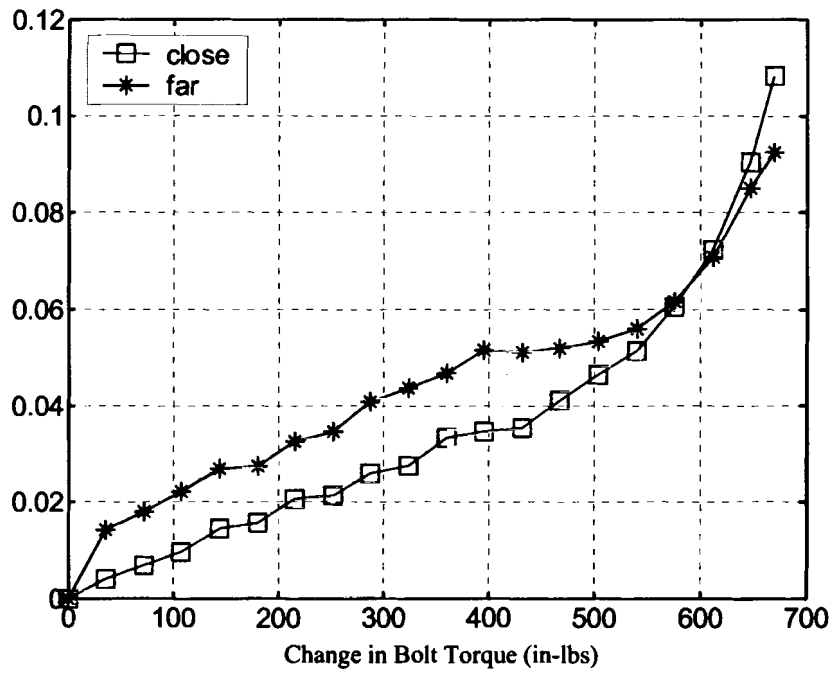
Figure 3-28 Loosening Indicator for Test 2
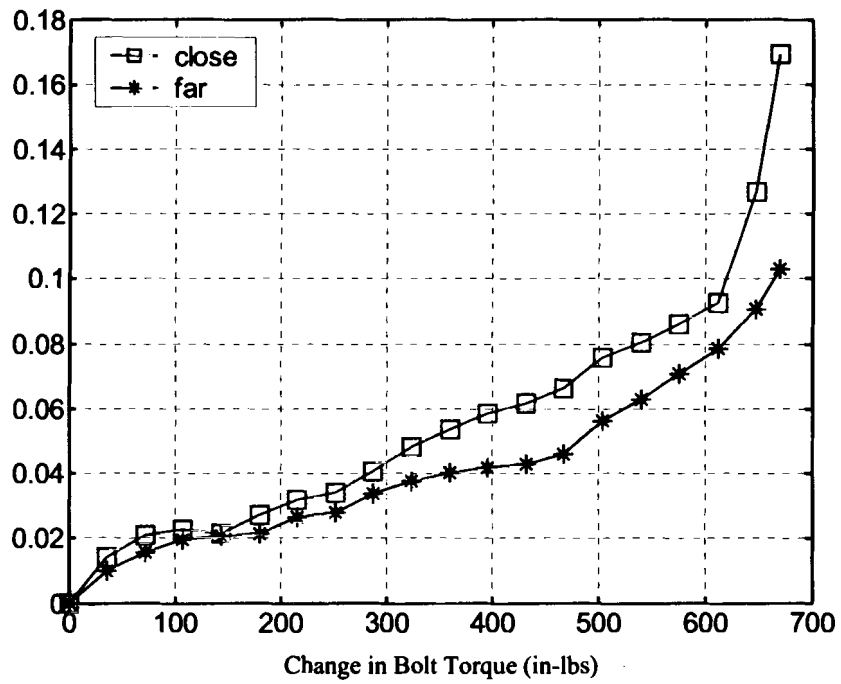
Figure 3-29 Loosening Indicator for Test 3

The results presented in this section shows that change in the boundary conditions of a bolted plate can be detected using the transfer functions technique presented here. However the dynamic strain sensors were not able to accurately predict the damage location. A higher damage index is obtained for the sensor far away from the damage than a sensor located closer to the damage. The accelerometer test returned a larger damage index for the sensor next to the loosened bolt, but the difference between the indices values were not significantly large. In the transfer function experiments, the investigation had the benefit of knowing the damage location, and placed a sensor near that location. However, this is not possible in practical applications. Based on these results, the transfer function technique was abandoned for another technique that showed more promise for a generic structural health monitoring system.

3.5.5 Transmittance Testing

3.5.5.1 Frequency Range Investigation. The frequency range from 0 Hz to 20 kHz was investigated for the best possible frequency range to excite a system and detect damage. The frequency investigation was done by splicing together five smaller successive 4 kHz bandwidth test results. Smaller bandwidths allowed a higher frequency resolution than would be possible over 20 kHz. Damage indices were calculated for different bandwidths within the entire range, and the bandwidths were chosen to maximize the damage index where the damage occurred. Larger damage indices were found using the accelerometers over the dynamic strain sensors. Two different frequency ranges or bandwidths were found to produce the greatest damage indices for T23 and T32 when the instrumented bolt in Figure 3-11 was loosened. The results from the accelerometer plots are shown in Figures 3-30 and 3-31. Figure 3-30 corresponds to the

lower frequency bandwidth of 7 kHz to 9 kHz, and Figure 3-31 is for the 18 kHz to 20

kHz bandwidth. Both figures show the computed damage indices values, the

transmittance function plots for each torque setting as a function of the frequency, and the

difference (delta) between each torque setting and the "healthy" setting of 720 in-lbs .
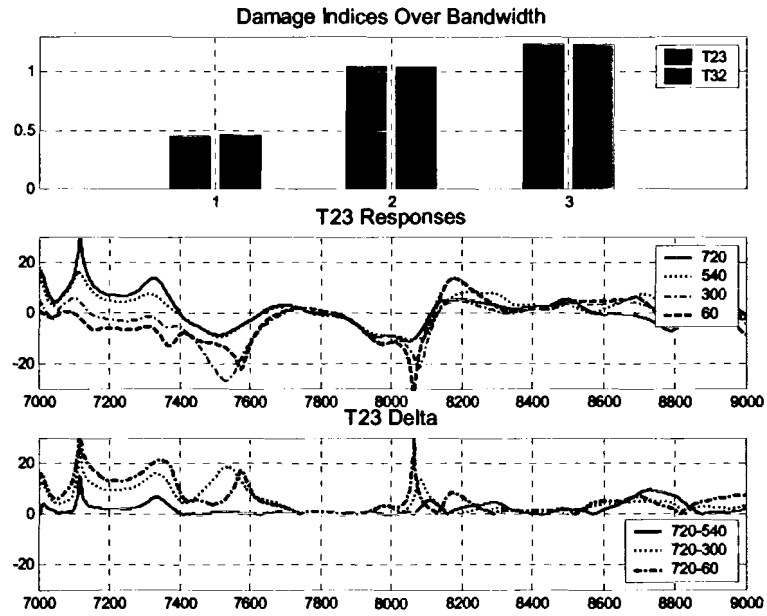
Figure 3-30 7 kHz to 9 kHz Investigation Using Accelerometers
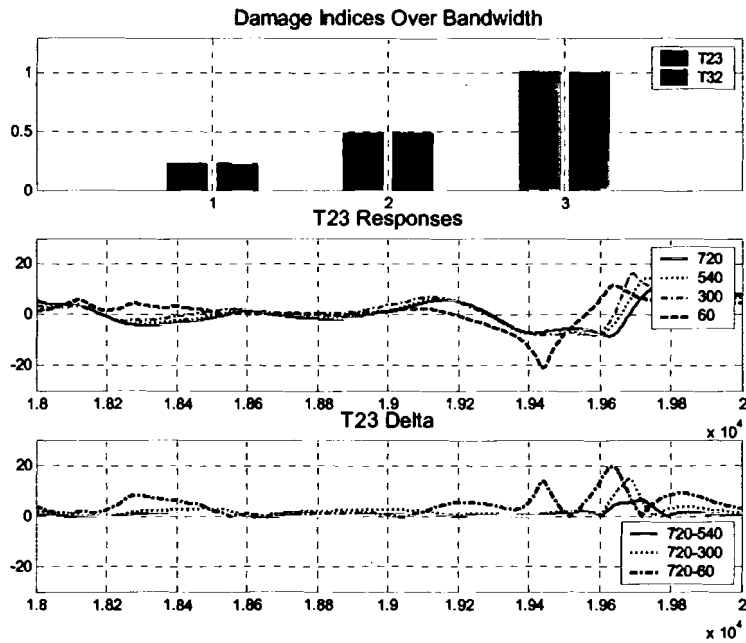
Figure 3-31 18 kHz to 20 kHz Investigation Using Accelerometers

The calculated damage indices were larger for the 7 kHz to 9 kHz range than the damage indices calculated in the 18 kHz to 20 kHz range. The results for the dynamic strain sensor tests are shown in Figures 3-32 and 3-33 below. The dynamic strain sensors were not as sensitive to the level of damage in the plate as were the accelerometers as shown by the smaller magnitude of the damage indices. However the dynamic strain sensors were able to show the successive levels of damage in the system.
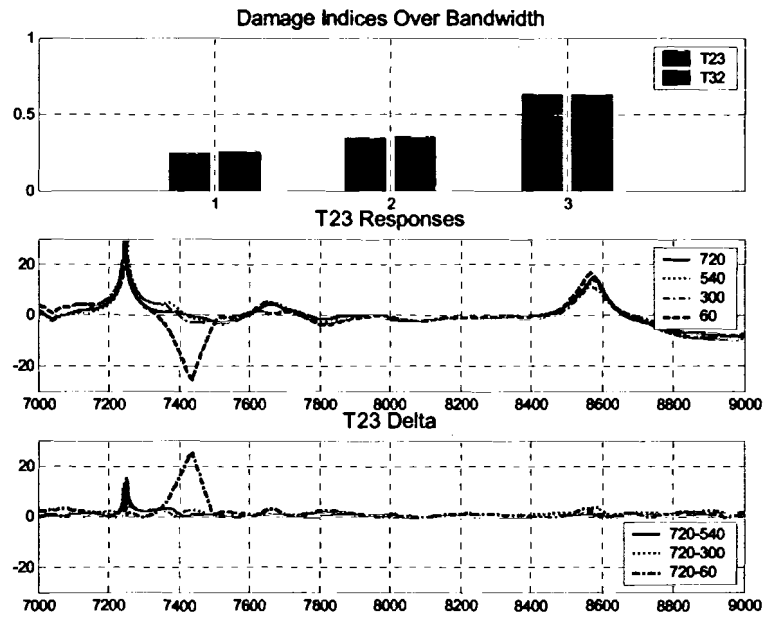
Figure 3-32 7 kHz to 9 kHz Investigation Using Dynamic Strain Sensors
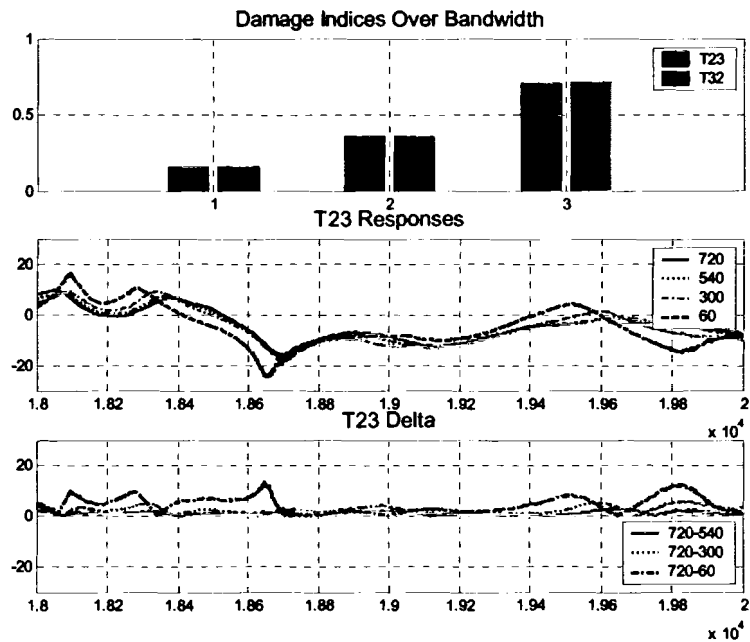
Figure 3-33 18 kHz to 20 kHz Investigation Using Dynamic Strain Sensors

3.5.5.2 Investigation for Reduction of Torque on One Bolt. A sensor was placed at each of the four corners of the bolted composite plate as described earlier in section 3.4.5.2. Extensive transmittance testing using accelerometers over the frequency ranges determined in section 3.5.5.1 showed that a bolt loosened between sensors 2 and 3 could be detected as depicted in Figure 3-11. The damage levels for the transmittance function T23 was higher than all other reported transmittance functions in the 7 kHz to 9 kHz frequency range when using accelerometers as sensors. Thus, according to Figure 3-34 the transmittance testing technique indicated that there was damage between sensors 2 and 3, which was the location of the bolt that was loosened.
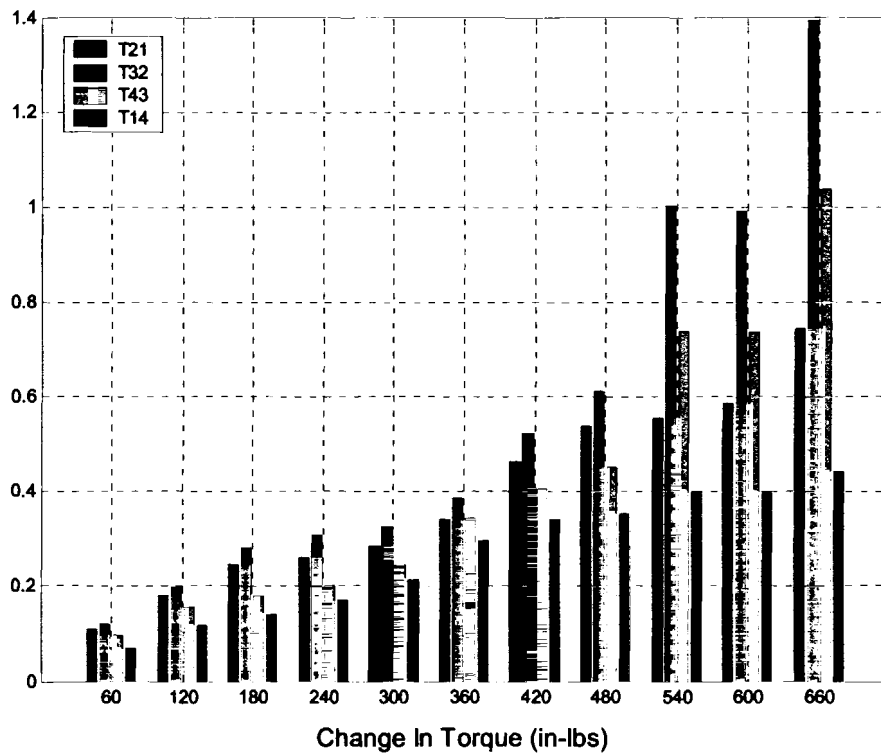
Figure 3-34 Damage Indices for 7 kHz to 9 kHz Freq. Range Using Accelerometers

Figure 3-35 below depicts the damage indices for the transmittance functions measured using accelerometers for the frequency range of 18 kHz to 20 kHz. The results as shown in Figure 3-35 do not show as strong a sensitivity to the damage as the transmittance results for the 7 kHz to 9 kHz range. The T23 damage index values were not always the largest damage index as shown for the 7 kHz to 9 kHz shown in Figure 3-34. The lower and intermediate changes in bolt torque tests in Figure 3-35 such as a change in bolt torque of 420 in-lbs shows larger damage index for T12 than T23. It is expected that T12 would show considerable sensitivity to the loosened bolt in these experiments because Sensor 2 is close to the bolt being loosened thus it is reasonable that sensor 2's response was affected by bolt being loosened in proximity to it. However, for the two frequency ranges investigated using accelerometers the 7 kHz to 9 kHz range produced better results. Tests conducted using both frequency ranges did show increasing damage indices for all transmittance functions as the bolt was progressively loosened.
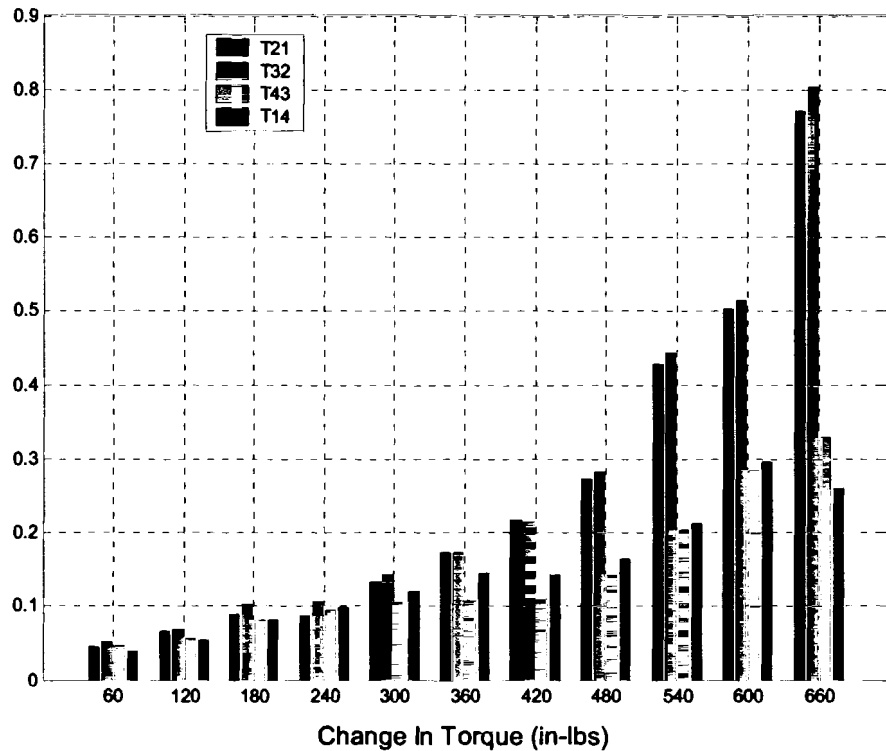
Figure 3-35 Damage Indices for 18 kHz to 20 kHz Using Accelerometers

The transmittance tests were repeated using the dynamic strain sensors. The higher frequency range of 18 kHz to 20 kHz gave the T23 damage index being the maximum index only for when there was a large change in the bolt torque such as 480 in-lbs and higher. T43 showed the largest damage index values for the lower change in torque tests, and had the second largest damage index for the high change in torque tests. These results are reported in Figure 3-36 below. The transmittance test results for the dynamic strain sensor in the 7 kHz to 9 kHz range did not shown any correlation between the damage indices and actual damage locations.
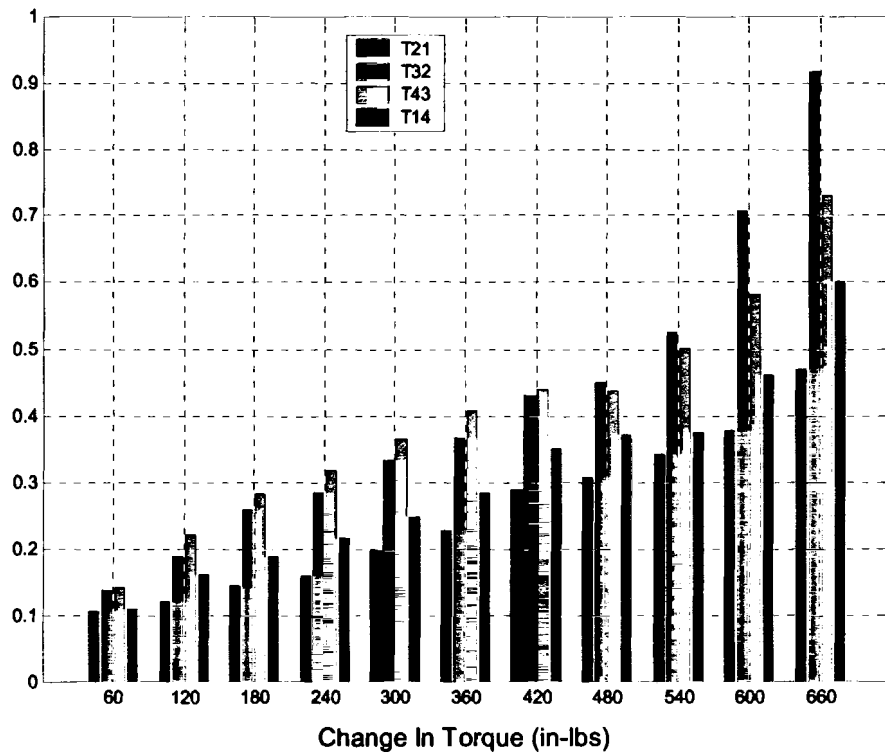
Figure 3-36 Damage Indices for 18 kHz to 20 kHz Using Dynamic Strain Sensors

3.5.5.3 Repeatability.

The repeatability of the most promising transmittance results was investigated here. The damage index for T23 and T32 were calculated using accelerometers for the 7 kHz to 9 kHz frequency range. The tests showed damage indices calculated from the transmittance functions had some variation. The T23 damage indices had a minimum of 0.677 and a maximum of 0.758, or +/-0.041, which is approximately 6% of the smaller value. The largest variation was in the transmittance pair T23 and T32 as shown in Figure 3-37. The other damage indices results exhibited lesser variation than T23.
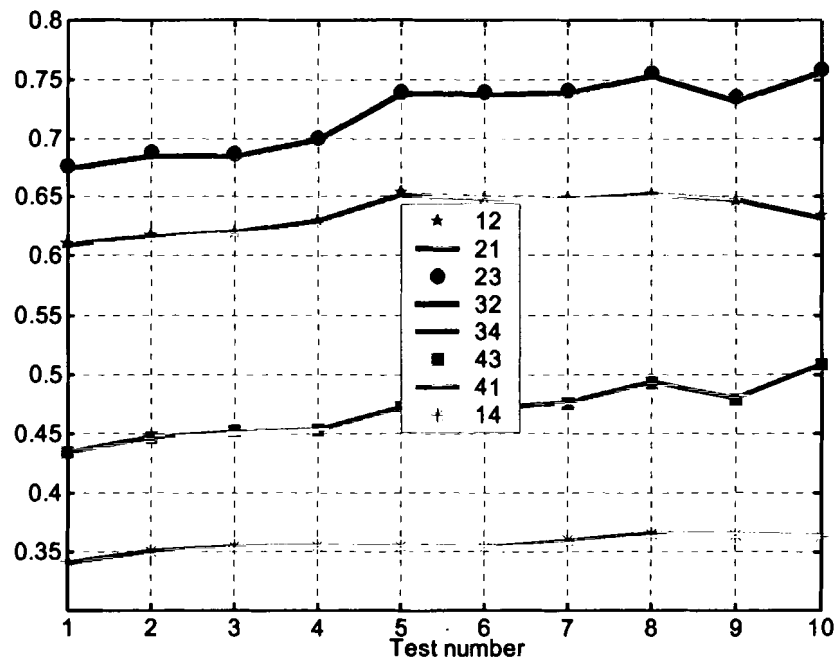
Figure 3-37 Transmittance Function Repeatability

3.5.5.4 Bolt Loosened at a Different Location.

The previous work for locating the damage on a plate used the same damage location. The frequency range investigation was conducted to maximize the damage detection that occurred between sensors 2 and 3.

94

The next the experiments were performed by loosening a bolt between sensors 1 and 4. Figure 3-38 plots the damage indices levels found from the transmittance functions. The results displayed here show that the method investigated thus far is not successful in locating damage that has occurred on the other side of the plate. If the method worked as hypothesized then T14 should have been greater than the other transmittance pairs for each torque setting. As Figure 3-38 shows the damage index for T14 is not the largest for each change in bolt torque, and T14 even has the smallest damage index for the largest change in bolt torque. However, since the average damage index is large, the method is still capable of detecting a loose bolt, although it cannot determine the location.
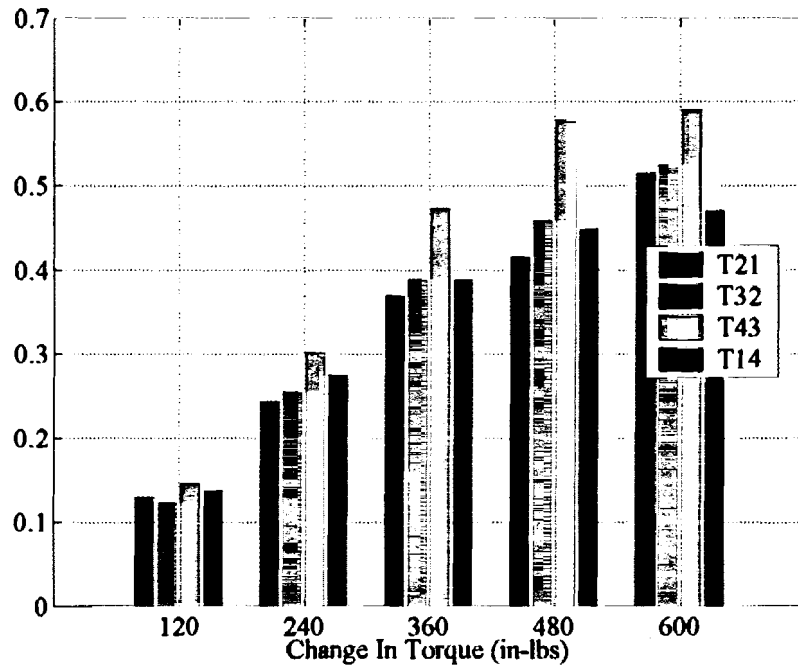
Figure 3-38 Damage Indices for Bolt Loosened at a Different Location

3.5.6 Summary and Conclusions

Various vibration-based methods of structural health monitoring have been investigated here. The investigation began by looking into possibly detecting damage through changes in the plate's fundamental frequency. The results have shown that the plate's fundamental frequency is not appreciably affected by changes in the bolt torque around the perimeter. The changes of transfer functions from sensors located next to, and away from a loosened bolt were also investigated for frequencies well outside the first several natural frequencies. It was hoped that at higher frequencies with smaller characteristic wave lengths of vibration, that the transfer function and transmittance function techniques would be sensitive to localized damages. The transfer function changes were quantified through a scalar damage index. However the transfer function technique presented here was not sufficiently sensitive to local damages to be an effective structural health monitoring technique.

A thorough investigation of using transmittance techniques to locate damage was presented finally. Two different frequency ranges were determined that increased the sensitivity of transmittance function to localized damage. The initial damage scenario investigated showed that when using accelerometers capable of measuring the normal acceleration of the plate excited by a chirp function , localized damage could be detected. The ideal frequency range to excite the plate with a chirp function was found to be 7 kHz to 9 kHz. And these results were determined to be repeatable. But the transmittance method failed when the damage location on the plate was moved. If a bolt was loosened on the opposite side of the plate from where the damage was for the previous work, the transmittance method was not successful in determining the damage location. The reason for this has not been explained. Possible theories are that the system needs to be

interrogated for a different frequency range than 7 kHz to 9 kHz, the transmittance function technique is not suited for flat plats, or that it was just a coincidence that the method seemed to work for the earlier tests.

Both the transfer function and the transmittance function methods presented here are capable of detecting a change in the system when only one bolt is loosened. A change was detected for the last transmittance function case where the damage location was altered. The transfer and transmittance function methods were successful in detecting a change, but were not successful in pin pointing the location of the damage.

4. CONCLUSIONS AND FUTURE WORK

Presented here are the summary conclusions for the work presented in this thesis from both major investigations

4.1 Conclusions

The analytical solution presented in Chapter 2 extended the Stroh formalism to obtain an analytical solution for the steady state vibration of a composite plate with either surface mounted or embedded piezoelectric layers. The boundary conditions at the edges and continuity conditions at interfaces between adjoining laminae are satisfied in the sense of Fourier series. The accuracy of the mechanical displacements, electric potential, stresses and electric displacement are dependent on the number of terms in the series solution. However, it should be noted that, unlike the FE solution, the analytical solution satisfies the equation of motion and charge equation exactly at every point within the body. In this thesis the new analytical method was applied to a case with clamped boundary conditions. While the previous exact dynamic solutions for thick composite plates were only for the mathematically simpler simply supported boundary conditions. Stresses, electrical potentials, and displacements were reported for various configurations with accuracy.

An assortment of vibration-based structural health monitoring methods was investigated in Chapter 3. The investigation began by looking into possibly detecting damage through changes in the plate's fundamental frequency, and through changes of transfer functions for frequency ranges well outside the first several natural frequencies.

And lastly, the ability of transmittance functions to detect damage was investigated. Damage detection through changes in a plate's fundamental frequency proved to be ineffective, and the changes in transfer functions were not sensitive enough. The most promising method out of the methods investigated was the transmittance method. Both the transmittance function method and the transfer function method were able to detect that damage occurred in the structure, and both methods could not detect the damage location reliability. The transmittance function technique presented showed promise in the literature, and seemed to work very well according to the preliminary results at locating the damage. However, most of the success in the literature was with a one-dimensional system such as a beam, and there was not a lot of success with a two dimensional system such as a plate. Schultz et al. (1999) was successful in detecting and locating damage in a cantilever beam, but was not as successful in consistently locating delamination in a composite plate.

4.2   Future Work

The transmittance function technique may still work for a two-dimensional structural health-monitoring scheme with further investigation. Perhaps even higher frequency excitation would be successful. This investigation was limited to 20 kHz because of hardware constraints, but similar Siglab units are capable of analysis up to 50 kHz. Also the addition of more sensors to the detection scheme may produce better results, but at an added cost of complexity and expense. A Finite Element simulation of both the transfer function, and transmittance function methods for rectangular plates would prove useful in deciding whether this method is advantageous. Such a mathematical simulation would not be subject to complicating factors such as temperature, viscoeleastic creep, and

benefit from ideal material properties and supports. Future experimental investigations may lessen these effects by beginning with an isotropic elastic material such as aluminum.

REFERENCES

ABAQUS Users Manual, 2002, Version 6.3, Hibbit, Karlson & Sorensen, Inc.

Allik, H., Hughes, T. J. R., 1970, Finite Element Method for Piezoelectric Vibration. *International Journal for Numerical Methods in Engineering*, Vol. 2, pp. 151-157.

Bailey, T., Hubbard, J. E., 1985, Distributed Piezoelectric-Polymer Active Vibration Control of a Cantilever Beam, *Journal of Guidance, Control, and Dynamics*, Vol. 8, pp. 605-611.

Banks, H. T., Emeric, P. R., 1998, Detection of Non-Symmetrical Damage in Smart Plate-Like Structures, *Journal of Intelligent Material Systems and Structures*, Vol. 9, pp. 818-828.

Batra, R. C., Geng, T. S., 2002, Comparison of Active Constrained Layer Damping by Using Extension and Shear Mode Actuators, *Journal of Intelligent Material Systems and Structures*, Vol. 12, pp. 349-368.

Batra, R. C., Ghosh, K., 1995, Deflection Control During Dynamic Deformations of a Rectangular Plate Using Piezoceramic Elements, *AIAA Journal*, Vol. 33, pp. 1547-1548.

Batra, R. C., Liang, X. Q., 1997a, The Vibration of a Rectangular Laminated Elastic Plate with Embedded Piezoelectric Sensors and Actuators, *Computers and Structures*, Vol. 63, pp. 203-216.

Batra, R. C., Liang, X. Q., 1997b, Finite Dynamic Deformations of Smart Structures, *Computational Mechanics*, Vol. 20, pp. 427-438.

Batra, R. C., Liang, X. Q., Yang, J. S., 1996a, The Vibration of a Simply Supported Rectangular Elastic Plate Due to Piezoelectric Actuators, *International Journal of Solids and Structures*, Vol. 33, pp. 1597-1618.

Batra, R. C., Liang, X. Q., Yang, J. S., 1996b, Shape Control of Vibrating Simply Supported Rectangular Plates, *AIAA Journal*, Vol. 34, pp. 116-122.

Berman, J., Quattrone, R., Averbuch, A., Lalande, F., Cudney, H., Raju, V., Cohen, G.L., 1999, *Piezoelectric Patch Sensors for Structural Integrity Monitoring of Composite-Upgraded Masonry and Concrete Structures*, US Army Corps of Engineers, Construction Engineering Research Laboratory, CERL Technical Report 99/72.

Bisegna, P., Maceri, F., 1996, An Exact Three-Dimensional Solution for Simply Supported Rectangular Piezoelectric Plates, *Journal of Applied Mechanics*, Vol. 63, pp. 628-638.

Brooks, S., Heyliger, P., 1994, Static Behavior of Piezoelectric Laminates With Distributed and Patched Actuators, *Journal of Intelligent Material Systems and Structures*, Vol. 5, pp. 635-646.

Caccese, V., 2001, Modular Advanced Composite Hull-form (MACH) Technology, Proposal funded by Office of Naval Research Project Number 5-6-46601, University of Maine.

Crawley, E. F., Anderson, E. H., 1990, Detailed Models of Piezoceramic Actuation of Beams, *Journal of Intelligent Material Systems and Structures*, Vol. 1, pp. 4-25.

Crawley, E. F., de Luis, J., 1987, Use of Piezoelectric Actuators as Elements of Intelligent Structures, *AIAA Journal*, Vol. 25, pp. 1373-1385.

Doebling, S. W., Farrar, C. R., Prime, M. B., Shevitz, D. W., 1996, Damage Identification and Health Monitoring of Structural and Mechanical Systems From Changes in Their Vibration Characteristics: A Literature Survey, Los Alamos National Laboratory, Report No. LA-12767-MS, Los Alamos, NM.

Eshelby, J. D., Read, W. T. and Shockley W., 1953, Anisotropic Elasticity With Applications to Dislocation Theory, *Acta Metallurgica*, Vol.1, pp. 251-259.

Farrar, C.R., Doebling, S.W., 1997, An Overview of Modal-Based Damage Identification Methods, *Proceedings of DAMAS Conference*, Sheffield, UK.

Fugate, M. L., Sohn, H., Farrar, C. R., 2001, Vibration-Based Damage Detection Using Statistical Process Control, *Mechanical Systems and Signal Processing*, Vol. 15, No. 4, pp. 707-721.

Ganguli, R., 2001, A Fuzzy Logic System for Ground Based Structural Health Monitoring of a Helicopter Rotor Using Modal Data, *Journal of Intelligent Material Systems and Structures*, Vol. 12, pp. 397-407.

Ghosh, K., Batra, R. C, 1995, Shape Control of Plates Using Piezoceramic Elements, *AIAA Journal*, Vol. 33, pp. 1354-1357.

Ghoshal, A., Sundaresan, M. J., Schulz, M. J., Pai, P. F., 2000, Structural Health Monitoring Techniques for Wind Turbine Blades, *Journal of Wind Engineering and Industrial Aerodynamics*, Vol. 85, pp. 309-324.

Ha, S. K., Keilers, C., Chang, F. K., 1992, *Finite Element Analysis of Composite Structures Containing Piezoceramic Sensors and Actuators*, AIAA Journal, Vol. 30, pp. 772-780.

Heyliger, P., 1994, Static Behavior of Laminated Elastic/Piezoelectric Plates, *AIAA Journal*, Vol. 32, pp. 2481-2484.

Heyliger, P., 1997, Exact Solutions For Simply Supported Laminated Pizoelectric Plates, *Journal of Applied Mechanics*, Vol. 64, pp. 299-306.

Heyliger, P., Brooks, S, 1995, Free Vibration of Piezoelectric Laminates In Cylindrical Bending, *International Journal of Solids and Structures*, Vol. 32, pp. 2945-2960.

Heyliger, P., Brooks, S., 1996, Exact Solutions For Laminated Piezoelectric Plates In Cylindrical Bending, *Journal of Applied Mechanics*, Vol. 63, pp. 903-910.

Heyliger, P., Saravanos, D. A., 1995, Exact Free-Vibration Analysis Of Laminated Plates With Embedded Piezoelectric Layers, *Journal of the Acoustical Society of America*, Vol. 98, pp. 1547-1555.

Inman, D. J., 2001, *Engineering Vibrations*, Prentice Hall, New Jersey.

Kabeya, K., 1998, *Structural Health Monitoring Using Multiple Piezoelectric Sensors And Actuators*, Master's Thesis, Virginia Polytechnic Institute and State University.

Kessler, S. S., Spearing, S. M., Atalla, M J., Cesnik, C. E. S., Soutis, C., 2002, Damage Detection in Composite Materials Using Frequency Response Methods, *Composites: Part B*, Vol. 33, pp. 87-95.

Kim, J.-T., Stubbs, N., 2002, Improved Damage Identification Method Based on Modal Information, *Journal of Sound and Vibration*, Vol. 252, No. 2, pp. 223-238.

Kuo, E.Y, Jayasuriya, A.M.M., 2002, A High Mileage Vehicle Body Joint Degradation Estimation Method, *International Journal of Materials and Product Technology*, Vol. 17, Nos. 5/6, pp. 400-410.

Lee, C. K., 1990, Theory of Laminated Piezoelectric Plates for the Design of Distributed Sensors/Actuators. Part 1: Governing Equations and Reciprocal Relationships, *Journal of the Acoustical Society of America*, Vol. 87, pp. 1144-1158.

Lee, J. S., Jiang, L. Z., 1996, Exact Electroelastic Analysis of Piezoelectric Laminae Via State Space Approach, *International Journal of Solids and Structures*, Vol. 33, pp. 977-990.

Lew, J. S., Juang, J.N., 2002, Structural Damage Detection Using Virtual Passive Controllers, *Journal of Guidance, Control, and Dynamics*, Vol. 25, No. 3, pp. 419-424.

Mitchell, J. A., Reddy, J. N., 1995, A Refined Hybrid Plate Theory for Composite Laminates With Piezoelectric Laminae, *International Journal of Solids and Structures*, Vol. 32, pp. 2345-2367.

Park, G., Cudney, H. H., Inman, D. J., 2000, An Integrated Health Monitoring Technique Using Structural Impedance Sensors, *Journal of Intelligent Material Systems and Structures*, Vol. 11, pp. 448-455.

Park, K. C., Reich, G. W., Alvin, K.F., 1998, Structural Damage Detection Using Localized Flexibilities, *Journal of Intelligent Material Systems and Structures*, Vol. 9, pp. 911-919.

Robbins, D. H., Reddy, J. N., 1991, Analysis of Piezoelectrically Actuated Beams Using a Layer-Wise Displacement Theory, *Computers and Structures*, Vol. 41, pp. 265-279.

Salawu, O. S., 1997, Detection of Structural Damage Through Changes in Frequency: A Review, *Engineering Structures*, Vol. 19, No. 9, pp. 718-723.

Schulz, M.J., Abdelnaser, A.S., Pai, P.F., Linville, M.S., Chung, J., 1997, Detecting Structural Damage Using Transmittance Functions, *International Modal Analysis Conference*, Orlando, Florida.

Schulz, M.J., Pai, P.F., Inman, D.J., 1999, Health Monitoring and Active Control of Composite Structures Using Piezoceramic Patches, *Composites: Part B*, Vol. 30, pp. 713-725.

Stroh., A. N., 1958, Dislocations and Cracks in Anisotropic Elasticity, *Philosophical Magazine*, Vol. 3, pp. 625-646.

Tiersten, H. F., 1969, *Linear piezoelectric plate vibrations*, Plenum Press, New York.

Ting, T. C. T., 1996, Anisotropic Elasticity, Theory and Applications, *Oxford Engineering Science Series*, No 45. Oxford University Press, New York.

Todd, M. D., Nichols, J. M., Pecora, L. M., Virgin, L. N., 2001, Vibration-Based Damage Assessment Utilizing State Space Geometry Changes: Local Attractor Variance Ratio, *Smart Materials and Structures*, Vol. 10, pp. 1000-1008.

Vel, S. S., Batra, R C., 2001, Exact Solution for Rectangular Sandwich Plates With Embedded Piezoelectric Shear Actuators, *AIAA Journal*, Vol. 39, pp. 1363-1373.

Vel, S. S., Batra, R. C, 2000, Cylindrical Bending of Laminated Plates with Distributed and Segmented Piezoelectric Actuators/Sensors, *AIAA Journal*, Vol. 38, pp. 857-867.

Vel, S. S., Batra, R. C., 2000, Three-Dimensional Analytical Solution for Hybrid Multilayered Piezoelectric Plates. *Journal of Applied Mechanics*, Vol. 67, pp. 558-567.

Vel, S. S., Batra, R. C., 2001, Exact Solution for the Cylindrical Bending of Laminated Plates With Embedded Shear Actuators, *Smart Materials and Structures*, Vol. 10, pp. 240-251.

Wang, B. T., Rogers, C. A., 1991, Laminate Plate Theory for Spatially Distributed Induced Strain Actuators, *Journal of Composite Materials*, Vol. 25, pp. 433-452.

Wang, D. H., Huang, S. L., 2000, Health Monitoring and Diagnosis for Flexible Structures with PVDF Piezoelectric Film Sensor Array, *Journal of Intelligent Material Systems and Structures*, Vol. 11, pp. 482-491.

Yan, Y. J., Yam, L. H., 2002, Online Detection of Crack Damage in Composite Plates Using Embedded Piezoelectric Actuators/Sensors and Wavelet Analysis, *Composite Structures*, Vol. 58, pp. 29-38.

Yang, J. S., Batra, R. C., Liang, X. Q., 1994, The Cylindrical Bending Vibrations of a Laminated Elastic Plate Due to Piezoelectric Actuators, *Smart Materials and Structures*, Vol. 3, pp. 485-493.

Zak, A., Krawczuk, M., Ostachowicz, W., 2000, Numerical and Experimental Investigation of Free Vibration of Multiplayer Delaminated Composite Beams and Plates, *Computational Mechanics*, Vol. 26, pp. 309-315.

Zhang, H., Schulz, M. J., Ferguson, F., 1999, Structural Health Monitoring Using Transmittance Functions, *Mechanical Systems and Signal Processing*, Vol. 13, No. 5, pp. 765-787.

Zou, Y., Tong, L., Steven, G. P., 2000, Vibration-Based Model-Dependent Damage (Delamination) Identification and Health Monitoring for Composite Structures—A Review, *Journal of Sound and Vibration*, Vol. 230, No. 2, pp. 357-378.

Zubaydi, A., Haddara, M.R., Swamidas, A.S.J., 2002, Damage Identification in a Ship's Structure Using Neural Networks, *Ocean Engineering*, Vol. 29, pp. 1187-1200.

APPENDIX A

Instrumented Bolt Information and Calibration

A.L. DESIGN, INC.

1411 Military Road, Buffalo, NY 14217, USA   (716) 875-6240

FAX (716) 875-2404

A FEW PRACTICAL SUGGESTIONS ON THE BEST WAY TO USE LOAD CELLS, LOAD WASHERS AND FORCE TRANSDUCERS

Load Cells are generally used to measure and detect forces or changes in the magnitude of forces.

The ideal way to set up load cells is to mount them on a rigid (very rigid) base. This base could be a thick flat steel plate which should be hardened to Rockwell 44C or higher and ground flat with a surface grinder. The top plate should be just as strong as the bottom one.

Don't use soft steel plates or copper, aluminum or plastic plates. The soft materials will cause large errors. (High hysteresis, nonlinearity and non-repeatability.)

Whenever possible use load buttons with spherical surfaces. These will concentrate the applied force on the center of the load cell. If there is no room for load buttons on top and bottom try to use at least one at the top. If there is no room for load buttons then it is important to make sure that the two surfaces which come in contact with the load cell are parallel. If they are not the load will be placed off center, resulting in less accurate results.

The practical usable range of a load cell is generally 10% to 100% capacity. If you exceed the capacity then obviously the unit is overloaded and permanent deformation may result (zero shift) or the unit could be crushed. Dropping calibrating weights on the cell even from a small height could crush the load cell. So be careful and slowly place the load on the load cell. Make sure the load cell is not slanted at an angle since it is important that it is positioned perfectly vertical or in line with the applied force (within +/- 0.5 degree or better). Make sure there are no side loads applied to the load cell unless it is specially designed to withstand side loading.

If the force or weight is below 10% of the load cell capacity then the errors will make the measurement less accurate, for example a 10,000 lb. capacity load cell with an accuracy of 0.2% FS (full scale) will give a 100 lb. weight +/- 20 lb. accuracy (The 0.2% of 10,000 is 20 lbs.) This is usually unacceptable. To get accurate results the force to be measured should be near the full capacity of the load cell. Of course other requirements may make this impractical.

When the load cell is hooked up to the readout/power supply the numbers may drift some due to the warmup requirement of the instrument and load cell. Even though the load cell is usually temperature compensated some zero drift is to be expected as the temperature changes. Readings and tests should be done after the whole unit is at uniform temperature and the zero balance adjusted. Creep in twenty minutes is to be expected in the range of 0.2 - 0.3% FS.

For accurate tests, calibration runs, etc., make several test runs. A minimum of three to five test runs would be adequate most of the time. A minimum of three calibration points should be selected (20%, 60%, 100% FS.). Of course the more points you have selected the more information you'll have about the performance of the unit. MAKE SURE THE LOAD IS NEVER LESS THAN 10% CAPACITY. (DON'T REDUCE THE LOAD TO ZERO DURING CALIBRATION RUNS.) You can get a zero reading after the tests are finished. Usually ten test runs are sufficient to get very reliable and accurate results.

Load washers are small load cells and it is important that load buttons are used on top and bottom for best performance. If no buttons are used the accuracy of the results will suffer.

If you use Load Washers to measure bolt tension make sure you use hardened washers between the underside of the bolt head and the Load Washer. These washers should be as thick as possible. These tests require quite elaborate set ups so consult us before making the tests.

When using the readout instruments/power supplies make sure that they are hooked up properly. The red and black wires should be connected to 10 or 5 Vdc power, the green and white wires to the signal indicator. After waiting for a few minutes (15 to 30) to allow the instrument and the transducer to warm up, the zero should be adjusted and the reading recorded. Now you can start the test runs and do your measurements. These recommendations are very general. If you have any specific questions call us and we will be glad to help you, (716-875-6240).

Sincerely,

Andrew Lenkei, P.E.

107

A.L.DESIGN,INC.
1411 MILITARY ROAD
BUFFALO, NEW YORK, 14217
U.S.A.

(716) 875-6240
FAX: (716)875-2404

THIS PROGRAM BY A.L.DESIGN, INC. CALCULATES THE
NON LINEARITY, HYSTERESIS, REPEATABILITY, AND
BEST FIT STRAIGHT LINE THROUGH THE ACTUAL
CALIBRATION POINTS OF THIS TRANSDUCER.

OUR CALIBRATION STANDARDS ARE TRACEABLE TO THE N.I.S.T., (NBS).

CUSTOMER: UNIVERSITY OF MAINE
             ORONO,   ME   04469

THIS CALIBRATION SHEET SHOWS THE CHARACTERISTICS OF THE TRANSDUCER

DATE   :   08-12-2002

MODEL   :   ALD-BOLT-1/2-2

SERIAL NO. :   220807

CAPACITY   = 9220 LBS

EXCITATION   = 10 VOLTS DC

RESISTANCE BETWEEN RED & BLACK WIRES =497 OHMS NOMINAL

RESISTANCE BETWEEN WHITE & GREEN WIRES= 350 OHMS NOMINAL

SAFE OVERLOAD   = 150% OF RATED CAPACITY

ULTIMATE OVERLOAD = 250% OF RATED CAPACITY

NOMINAL TEMPERATURE EFFECT ON RATED OUTPUT (15-115 deg.F) *
            = 0.08% / deg.F OF RATED OUTPUT

NOMINAL TEMPERATURE EFFECT ON ZERO BALANCE (15-115 deg.F) *
            = 0.08% / deg.F OF RATED OUTPUT
        * THIS DOES NOT APPLY TO GAGED BOLTS
        OR TRANSDUCERS MADE OF MATERIALS OTHER THAN
        17-4PH STAINLESS STEEL.

STRAIN GAGE TEMPERATURE LIMITS FOR HIGH/LOW TEMP. OPTION.
HIGH TEMP. = +450 degrees F.   LOW TEMP. = -452 degrees F.
THESE TEMPERATURE EFFECTS ARE FOR FOIL STRAIN GAGES ONLY.
SEMICONDUCTOR STRAIN GAGES HAVE HIGHER TEMPERATURE SENSITIVITY

NUMBER OF CALIBRATION POINTS IS : 10
AT NO LOAD, INDICATOR OUTPUT READS 0 mV

<table>
<tr><td colspan="3">RUN #1</td><td colspan="3">RUN #2</td></tr>
<tr><td>POINT</td><td>LOAD</td><td>TRANSDUCER OUTPUT</td><td>POINT</td><td>LOAD</td><td>TRANSDUCER OUTPUT</td></tr>
<tr><td>#1</td><td>1844 LBS</td><td>4.34 mV</td><td>#6</td><td>1844 LBS</td><td>4.32 mV</td></tr>
<tr><td>#2</td><td>5532 LBS</td><td>12.94 mV</td><td>#7</td><td>5532 LBS</td><td>12.89 mV</td></tr>
<tr><td>#3</td><td>9220 LBS</td><td>21.61 mV</td><td>#8</td><td>9220 LBS</td><td>21.6 mV</td></tr>
<tr><td>#4</td><td>5532 LBS</td><td>12.97 mV</td><td>#9</td><td>5532 LBS</td><td>12.95 mV</td></tr>
<tr><td>#5</td><td>1844 LBS</td><td>4.32 mV</td><td>#10</td><td>1844 LBS</td><td>4.31 mV</td></tr>
</table>

CHARACTERISTICS PARTICULAR
TO THIS TRANSDUCER ARE :

NON LINEARITY = +/- .2 % F.S.

HYSTERESIS   +/- .17 % F.S.

REPEATABILITY = +/- .14 % F.S.

RATED OUTPUT = 21.6 mV

SENSITIVITY   = 2.16 mV/V

LOADCELL'S UNADJUSTED ZERO OFFSET = .13 mV

ADJUSTED INDICATOR ZERO OFFSET = 0 mV

.
.

.

CALCULATED VALUES USING THE BEST FIT
STRAIGHT LINE THROUGH THE EXPERIMENTAL POINTS

<table>
<tr><td>POINT</td><td>LOAD</td><td>TRANSDUCER OUTPUT</td></tr>
<tr><td>#1</td><td>922 LBS</td><td>2.2 mV</td></tr>
<tr><td>#2</td><td>1844 LBS</td><td>4.3 mV</td></tr>
<tr><td>#3</td><td>2766 LBS</td><td>6.5 mV</td></tr>
<tr><td>#4</td><td>3688 LBS</td><td>8.6 mV</td></tr>
<tr><td>#5</td><td>4610 LBS</td><td>10.8 mV</td></tr>
<tr><td>#6</td><td>5532 LBS</td><td>13 mV</td></tr>
<tr><td>#7</td><td>6454 LBS</td><td>15.1 mV</td></tr>
<tr><td>#8</td><td>7376 LBS</td><td>17.3 mV</td></tr>
<tr><td>#9</td><td>8298 LBS</td><td>19.4 mV</td></tr>
<tr><td>#10</td><td>9220 LBS</td><td>21.6 mV</td></tr>
</table>

109

SHUNT CALIBRATION DATA

LOAD CELL SERIAL NO. = 220807

SHUNT RESISTOR VALUE = 200000 OHMS

EXCITATION = 10 Vdc

SHUNT OUTPUT = 3.08 mV

SHUNT CONNECTION = RED and WHITE

EXCITATION = (+)RED and (-)BLACK
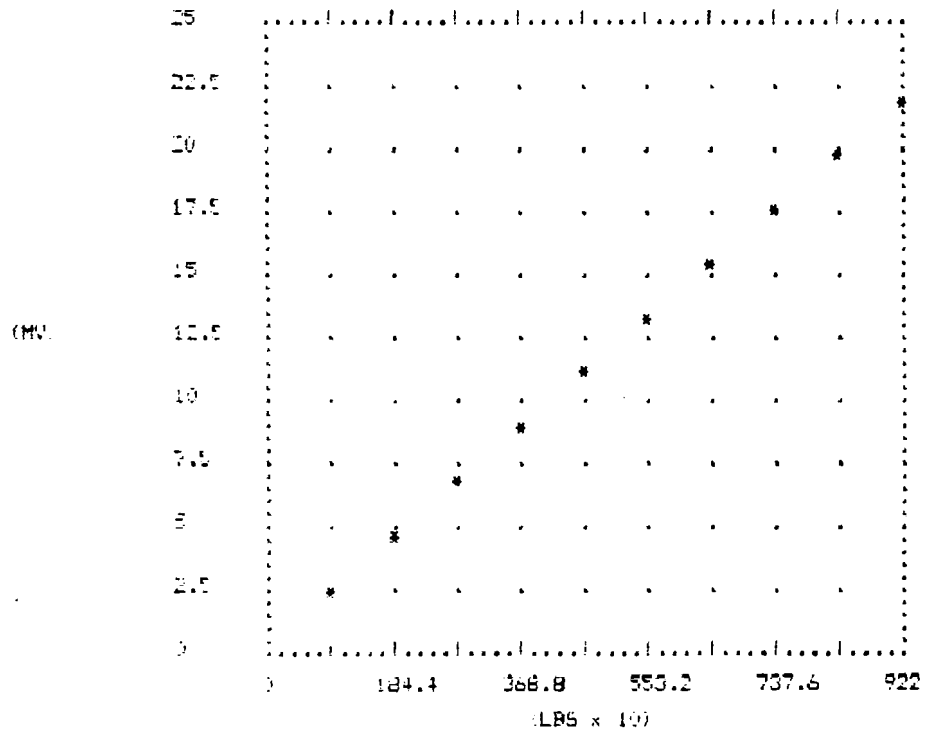
SIGNAL OUTPUT = (+)WHITE and (-)GREEN

WHEN USING AN ALD-MINI-UTC TENSION/COMPRESSION LOAD CELL THE SMOOTH FLAT SURFACE SHOULD
NOT TOUCH ANYTHING. THE OTHER SIDE WITH THE CIRCLE NEAR THE OUTER EDGE IS THE BASE. IT
IS OK TO MOUNT OTHER PARTS TO IT AND TO TOUCH THIS SURFACE ONLY.

WHEN CONNECTORS ARE SUPPLIED,
CONNECTOR PIN ASSIGNMENTS ARE:

A = BLACK (-) EXCITATION
B = WHITE (+) SIGNAL
C = RED   (+) EXCITATION
D = GREEN (-) SIGNAL

GREEN

350 OHM
BRG

SIGNAL

WHITE

RED   BLACK

EXCITATION

INTERNAL WHEATSTONE BRIDGE

110
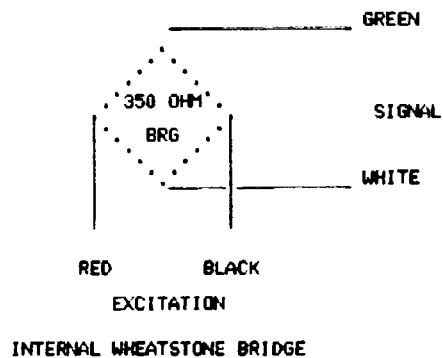
COMPUTED TRANSDUCER OUTPUT   VS.   LOAD

```
 25  :....!....!....!....!....!....!....!....!....!.....
     :
22.5 :    .    .    .    .    .    .    .    .    .   *
     :
 20  :    .    .    .    .    .    .    .    .    *
     :
17.5 :    .    .    .    .    .    .    .    *    .
     :
 15  :    .    .    .    .    .    .    *    .    .
     :
(MV) 12.5:   .    .    .    .    .    *    .    .    .
     :
 10  :    .    .    .    .    *    .    .    .    .
     :
 7.5 :    .    .    .    *    .    .    .    .    .
     :          .    *
     :
  5  :    .    *    .    .    .    .    .    .    .
     :
 2.5 :    *    .    .    .    .    .    .    .    .
     :
  0  :....!....!....!....!....!....!....!....!....!.....
     0        184.4      366.8      553.2      737.6      922
                         (LBS x 10)
```

APPENDIX B

Siglab Information

The SigLab acquisition and processing hardware was designed by a team of engineers with over 60 years of combined experience in the measurement art. The 20-42 and 50-21 systems are highly optimized for the task of making fast, accurate measurements of electrical, mechanical, or acoustical signals and systems. The SigLab systems are complex and powerful with capabilities that should not be confused with PC add-in boards or audio entertainment devices such as the "Sound Blaster". The goals of measurement quality, speed, size, durability and expandability are well met with the SigLab measurement hardware platform.

The differential inputs have ten full-scale ranges (20mV to 10V) allowing accurate measurement of signals from far less than a millivolt to 20 volts peak to peak. These inputs are protected up to 30 volts rms and the overload detectors guarantee that your measurements are valid by trapping overload conditions that may not be apparent due to subsequent filtering operations. You can specify ac/dc coupling as well as the dc offset. Optional integrated ICP power transducer bias sources provide a constant 4mA current with a 22 volt compliance to directly power accelerometers, microphones, and force transducers. Additionally, your own signal conditioning circuitry can be inserted in SigLab beneath the top cover access panel.

A fourth-order analog low-pass filter precedes the sigma-delta A/D converter providing complete alias protection with only 0.03 dB of ripple. The sigma-delta conversion technology provide ultra linear, and low noise performance. The SigLab 50-

112

21 boasts unmatched measurement quality with a guaranteed 95 dB spurious free dynamic range over its entire 50 kHz bandwidth.

A dedicated fixed point DSP filters and decimates the A/D data stream providing a selection of 13 alias-protected sampling rates down to 5 Hz. Either low-pass or band-pass filtering for narrow-band "zoom" analysis may be selected. Triggering circuitry provides slope control and 17 selectable threshold levels. The trigger source can be an input channel, an output channel, or a rear panel digital input.

The trigger may also select unfiltered data thereby providing a reliable trigger even with short duration "impulses" often encountered in modal impact testing.

The output subsystem looks much like the input subsystem in reverse. The TMS320C31 floating point DSP feeds previously acquired data or data generated mathematically (e.g. by using MATLAB) to the function generator FIFO buffer. The fixed point DSP then interpolates and optionally translates this data before sending it to the highly linear D/A converter. The output subsystem's signal quality is comparable to the input subsystem. The DSP is also used to generate predefined functions: sine, square, sawtooth, triangle, impulse, random, and chirp. Level control and DC offset can be applied to the analog signal before going to the output buffer amplifier. The buffer can source and sink at least 20 mA, has a 50 ohm output resistance, and is unconditionally stable.

The TMS320C31 floating-point DSP chip performs real-time processing tasks such as FFTs, auto and cross-spectral averaging, and computation of transfer and other functions. A real-time operating system kernel is also executing in the C31 to orchestrate the flow of data within SigLab and between SigLab and the host PC via the SCSI

113

interface. The system can be equipped with a generous amount of DRAM allowing gap free records of up to 15 million samples to be stored at the maximum sampling rate. Non-volatile memory (not shown) stores the input/output calibration factors. Except for a small boot program, all C31 code is downloaded from the host PC.

For expansion beyond four channels, SigLab's architecture allows interconnecting multiple units. The SigLab modules are linked by an external cable providing synchronous multi-channel capability. This Multi Unit Sync. subsystem manages the synchronization of all sampling clocks and trigger signals for the input and output channels. For normal operation SigLab is powered by a DC input between 12 and 15 volts. It can also run on its own internal NiCAD battery for a limited time.

This information was taken from http://www.dspt.com, for more information please refer to this website.

APPENDIX C

ACX Actuator

(ACX, Inc. actuators are now available through the Mide Technologies Corporation.)
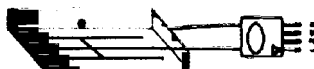
Model QP10W Specifications

Application type: strain actuator only
Device size (in): 2.00 x 1.50 x 0.015
Device weight (oz): 0.16
Active elements: 1 piezo wafer
Piezo wafer size (in): 1.81 x 1.31 x 0.010
Device capacitance: (µF): 0.10
Full scale voltage range (V): ±200
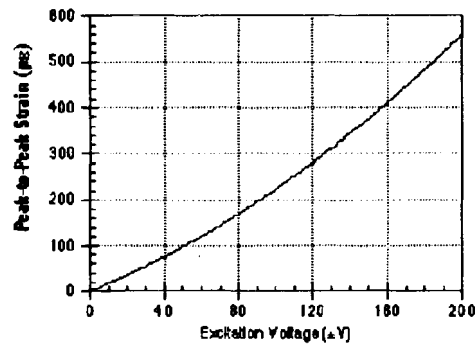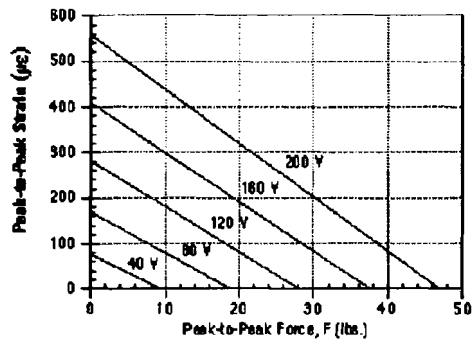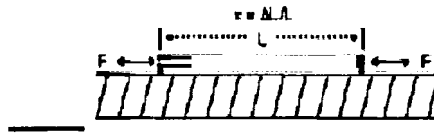
Functional Diagram

Device poled with positive voltage applied to pin 1.
Pins 2 and 3 not connected.

Bonded Configuration

Full scale strain, extension (µ ☒): ±278

Figure C-1 ACX Actuator Specifications

115

$r = \Delta L / L$

Price List

Figure C-2 ACX Actuator Strain to Voltage and Stain to Force Relationships

116

APPENDIX D

Dynamic Sensor Specifications

Ceramic Shear ICP Accelerometers

MINIATURE *(complete specifications are featured on pages 14 to 15)*

Miniature accelerometers are especially well suited for applications demanding high frequency range, small size, and light weight.

- NHV studies
- printed circuit boards
- card cages and chassis
- brackets
- thin panels
- shrouds
- conduits
- bearings

Available Sensor Options	
pfx	**For Complete Descriptions See Pages x to xii**
A	Adhesive Mount
HT	High Temperature
J	Ground Isolated
M	Metric Mounting
W	Attached Water Resistant Cable
●	Popular Product (see page i)

Designate option as prefix to model number, e.g., J352C66 specifies a unit with electrical ground isolated base.

Accessory key located on page 11

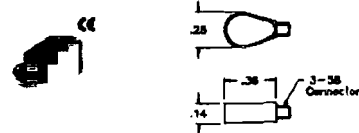● **Model 352A10** (accessory key: ●)
- 10 mV/g sensitivity
- 1 Hz to 20 kHz frequency range
- 0.7 gram in weight
- Integral cable
- Adhesive mount
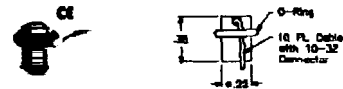
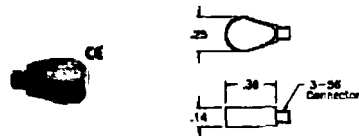Model 352A10

Model 352A21 (accessory key: ●②)
- 10 mV/g sensitivity
- 0.7 Hz to 13 kHz frequency range
- 0.6 gram in weight
- Adhesive mount
- Durable titanium housing
- Mating cable provided

Model 352A21

● **Model 352C22** (accessory key: ●②)
- 10 mV/g sensitivity
- 0.7 Hz to 13 kHz frequency range
- 0.5 gram in weight
- Adhesive mount
- Anodized aluminum housing
- Electrically ground isolated
- Mating cable provided

Models 352C22, 352A24

Model 352A24 (accessory key: ●②)
- 100 mV/g sensitivity
- 0.8 Hz to 10 kHz frequency range
- 0.8 gram in weight
- Anodized, ground isolated, aluminum housing
- Mating cable provided

PCB PIEZOTRONICS, INC. ☎ 716-684-0001

Figure D-1 Accelerometers Specifications'

Model 740B02 Dynamic ICP Piezoelectric Strain Sensor Specifications

| Dynamic Performance	
Sensitivity¹	50 mV/με
Amplitude Range¹	±100 με pk
Environmental	
Operating Temperature	-65 to +250 °F (-54 to +121 °C)
Electrical	
Low Frequency Response	0.5 Hz
Excitation Voltage	20 to 30 VDC
Constant Current Excitation	2 to 20 mA
Output Bias	9 to 13 VDC
Mechanical	
Weight	0.02 oz (0.5 gram)
Size (W x L x H)	0.2 x 0.6 x 0.07 in (5.1 x 15.2 x 1.8 mm)
Mounting	Adhesive
Cable	Integral/Coaxial 10 ft (3 m) Terminates in 10-32 threaded plug
Housing	Titanium
Sensing Element	Quartz

¹ Actual value depends upon thickness and stiffness of sensor structure interface.

This product is CE-marking compliant to European Union EMC Directive, based upon conformance testing to the following European norms:
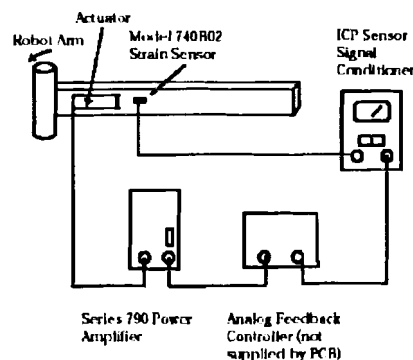- EN 50081-1: 1992 Emissions
- EN 50082-1: 1992 Immunity

SVS is the Shock and Vibration Sensors division of PCB Piezotronics, Inc., specializing in quartz, ceramic, charge, ICP³, and capacitive accelerometers. The divisional focus of SVS, combined with the strength and resources of PCB, offers customers exceptional customer service, 24-hour technical support, and an unconditional guarantee.

To obtain more information on this and other shock and vibration products, contact SVS at 1-888-684-0013. For information on other PCB products, call 1-716-684-0001, or visit our web site at: www.pcb.com.
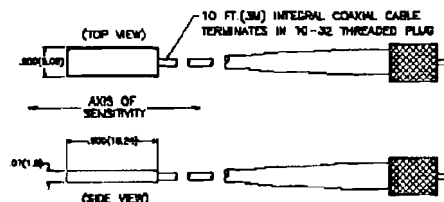
TYPICAL APPLICATION: An epoxy-bonded Model 740A02 Strain Sensor provides a control signal for an actively damped flexible robot manipulator, illustrated below. The electronic controller, with vibration feedback from the strain sensor, provides a signal to the amplifier, such that vibration amplitude is minimized. The active control system permits rapid settling time for a step rotation of the manipulator arm.

Figure D-2 Dynamic Strain Sensor Specification's

APPENDIX E

482A20 PCB ICP Sensor Signal Conditioner

Model Number 482A20	8 CHANNEL ICP® POWER SUPPLY	Revision. B ECN #: 10613

ELECTRICAL

Channels			8		
Transducer Excitation	volts		+24 ±1		
Excitation Current	mA		2-20 Adjustable		[1]
Voltage Gain (selectable)			x1, x10, x100		[3]
Gain Accuracy (all gains)	%		±1		
Frequency Response (-5%)	Hz		0.225 to 100 k		
Maximum Output Signal	volts		+10		
Output Impedance	ohms		<50		
Overload Detection	volts		±10		
Noise (spectral):	Typical	gain	x1	x10	x100
	1 Hz	μV√Hz	0.85	4.5	105
	10 Hz	μV√Hz	0.15	1.0	7.0
	100 Hz	μV√Hz	0.1	0.36	3.0
	1 kHz	μV√Hz	0.12	0.34	2.5
	10 kHz	μV√Hz	0.1	0.31	2.4
Broadband Noise:	1 Hz-10 kHz (maximum)	μV	9.1	50	480
Channel Isolation:	minimum	dB	72		
DC Offset (all gains)	mV		±50		
Power Required (50 to 400 Hz)	VAC/mA		90-130/500		
Alternate Power	VAC/mA		210-250/250		[2]

PHYSICAL

Connectors:	Input	type	BNC Jack
	Output	type	BNC Jack
Size (L x W x H):		in	9.7 x 4.0 x 6.3
		[cm]	[24,6 x 10,2 x 16,0]
Weight		lb [gm]	6.1 [2 767]

NOTES:
[1] Units supplied with current set at 4 mA ±0.6 mA.
[2] Unit is factory configured using internal jumpers when ordered with prefix "F". Example: F482A20.
[3] Units with serial number 139 or greater will power up to the same settings it had at power down.

SUPPLIED ACCESSORIES:
Model 017 AC Line Cord

In the interest of constant product improvement, we reserve the right to change specifications without notice.

ICP® is a registered trademark of PCB Piezotronics, Inc.

PCB PIEZOTRONICS

			Spec No.
Drawn			482-1200-80
Engineer			
Sales			
Approved			Sheet 1 of 1

Figure E-1 482A20 PCB ICP Sensor Signal Conditioner Specification's

APPENDIX F

Damping Program

```
function damping_driver

%   This function finds the damping coefficients for a series of text files
%   A plot is generated of the damping coefficients vs. applied torque
%   functions fileread is used to open the respect text files,
%   and function Find_Damping actually computes the damping coefficients

%   DD is a matrix of applied torques
%   DD(1,1) = 0 is the finger tight file

%   Functions Called:
%   -Find_Damping


DD(1,1) = [0]';
DD(2:20,1) = [50 60 70 80 90 100 120 130 140 150 160 170 200 230 300 360 480 600
720]';

%   loop to compute damping coefficients

for i = 1:max(size(DD))


str1 = 't_';
str2 = num2str(DD(i));
str3 = '_inst_narrow.txt';

fstring = strcat(str1,str2,str3);
damping(i) = Find_Damping(fstring);
torque(i) = DD(i);
end

%   Plot the results
plot(torque,damping)
axis([0 800 0 .014])
Title('Fundamental Mode Damping Sensitivity to Torque')
ylabel('Damping Coefficient')
xlabel('Bolt torque in (in-lbs)')
grid on;
```

```
axis([0 720 0 .014])

function damping = Find_Damping(filename)

%   Function to compute the damping coefficient for the input TRANSFER
%   FUNCION text file.  Utilizes the 3-dB down method to estimate the
%   damping coefficient.  This function works only for finding the damping
%   coefficient for the maximum peak.  The best results are obtained with
%   the transfer function bracketed around the peak response corresponding
%   to modal damping coefficient of interest.

%   m-files called:
%   -fileread


%   load the file
q = fileread(filename);
freq = q(:,1);
mag = q(:,2);

%   Find the maximum magnitude value, and it's location.
[max_mag,I] = max(mag);
omega_d = freq(I);

%   Calculate the 2 dB down points
dB3 = 20*log10(1/sqrt(2));
TwodBmag = max_mag+dB3;

%   Find omega_a
%   --------------------------------------------------------------
n = I-1;
mag(n);
while mag(n) > TwodBmag;
    n = n-1;
end

if mag(n) == TwodBmag
    omega_a = freq(n);
else
    magLOW = mag(n);
    omegaLOW = freq(n);

    magHIGH = mag(n+1);
    omegaHIGH = freq(n+1);
```

```
      omega_a = (omegaLOW - omegaHIGH)*((TwodBmag - magHIGH)/(magLOW -
magHIGH)) + omegaHIGH;
end
%   ---------------------------------------------------------------

%  Find omega_b
%  ***************************************************************
m = I+1;
mag(m);
while mag(m) > TwodBmag;
   m = m+1;
end

if mag(m) == TwodBmag
   omega_a = freq(m);
else
   magHIGH = mag(m);
   omegaHIGH = freq(m);

   magLOW = mag(m-1);
   omegaLOW = freq(m-1);

      omega_b = (omegaLOW - omegaHIGH)*((TwodBmag - magHIGH)/(magLOW -
magHIGH)) + omegaHIGH;
end
%  ***************************************************************

%  Compute the damping ratio
damping = (omega_b - omega_a)/(2*omega_d);


disp(TwodBmag)
disp(omega_a)
disp(omega_b)
disp(omega_d)
```

```
function res=fileread(filename)

%   This function is used to read the TRANSFER FUNCTION output generated by
%   Siglab.  The Siglab text file is opened, and the text preceding the
%   data is ignored.

format long g
[fid , message] = fopen(filename, 'rt');
dummy = fscanf(fid,'%c%[^\n]');
dummy = fscanf(fid,'%c%[^\n]');
dummy = fscanf(fid,'%s',[1,6]);
res=fscanf(fid,'%g');
res=transpose(reshape(res,3,[]));
status = fclose(fid);
```